ABSTRACT

Title of Document: NANOSTRUCTURED MATERIALS FOR SOLAR HYDROGEN GENERATION

Xiaofei Ma, Doctor of Philosophy, 2010

Directed By: Michael R. Zachariah, Professor
Chemical Physics Program
Department of Mechanical Engineering and Chemistry

Hydrogen can be considered a nonpolluting and inexhaustible energy carrier for the future. However, hydrogen is not readily available for use as a fuel. It exists in bound form with other elements (e.g. water, hydrocarbons) and as such energy is required to abstract molecular hydrogen from various feedstocks. Solar energy due to its abundance and low cost is being considered as the energy source for environmentally safe hydrogen generation.

This dissertation focuses on the development and characterization of nano-structured materials for solar thermochemical hydrogen generation, on the principle that concentrated solar radiation can be employed as the high-temperature energy source for driving an endothermic hydrogen generation process. The reaction mechanism and kinetics of different solar thermochemical processes using those nano-structured materials as reactants or catalysts were investigated. The experimental works in this dissertation can be divided into two main areas. The first

area is to study the properties and reactivity of in-situ generated Zn nanocrystals (NCs) for solar thermochemical Zn/ZnO water splitting cycle for hydrogen production. The particle size-resolved kinetics of Zn NCs oxidation, evaporation, and hydrolysis were studied using a tandem ion-mobility method in which the first mobility characterization size selects the NCs, whereas the second mobility characterization measures changes in mass resulting from a chemical reaction of the NCs. The second part of the dissertation is concentrated on the investigation of in-situ generated nano-sized metal particles as catalysts in liquid hydrocarbon decomposition process for hydrogen generation. Catalytic decomposition of liquid fuels (n-octane, iso-octane, 1-octene, toluene and methylcyclohexane) was achieved in a continuous tubular aerosol reactor as a model for the solar initiated production of hydrogen, and easily separable CO free carbonaceous aerosol product. The effects of fuel molecular structure and catalyst concentration on the overall hydrogen yield were studied. Using the similar aerosol catalysis idea, ignition of liquid fuels catalyzed by in-situ generated metal nanoparticles was investigated. The morphological change of catalyst particles during fuel ignition process and the catalytic ignition mechanism are discussed.

NANOSTRUCTURED MATERIALS FOR SOLAR HYDROGEN GENERATION

By

Xiaofei Ma

Dissertation submitted to the Faculty of the Graduate School of the
University of Maryland, College Park, in partial fulfillment
of the requirements for the degree of
Doctor of Philosophy
2010

Advisory Committee:
Professor Michael R. Zachariah, Chair
Professor Gregory Jackson
Professor George W. Mulholland
Professor Sheryl Ehrman
Professor Bryan Eichhorn

Dedication

To

My parents

Yucheng Ma and Xiaoling Liang,

And my wife

Yun Zhou.

Thank you for your unconditional love and support. Thank you for your unwavering faith and absolute belief in my abilities. You have sacrificed so much and waited so long for this moment to come true and I dedicate this dissertation to you.

Acknowledgements

I owe my gratitude to all the people who have made this dissertation possible. First and foremost, I thank my advisor, Professor Michael R. Zachariah, for his generous support and guiding me throughout the years of my graduate study. Without his invaluable ideas, experience and strategic insights this dissertation would not have been possible. I have been amazingly fortunate to have him as my advisor. His advice in my research, career and life has been one of my most valuable assets throughout my life.

I would like to thank Professor George W. Mulholland, Professor Gregory Jackson, Professor Sheryl Ehrman, and Professor Bryan Eichhorn for serving on my committee and taking time editing my dissertation, attending my defense and giving me valuable suggestions. I also offer my sincere gratitude to the director of Chemical Physics Program, Professor Michael Coplan, who has been always there to listen and give advice.

I would like to thank all my friends and colleagues in my group, with whom I have worked, and because of whom my graduate experience has been one that I will cherish forever. I would also like to give a special thanks to my friend and colleague Dr. Lei Zhou, who introduced me to the Chemical Physics Program and to this research group. I would like to thank Dr. Ashish Rai, who was a senior graduate student in our lab and mentoring me during my first year of graduate study and research. I would like to thank Dr. Anshuman A. Lall, Dr. Purnendu Chakraborty, Dr. Brian J. Henz, with whom I have had the great pleasure of collaborative work. I also thank Dr. Kyle Sullivan for helping me improving my Ph.D. presentation.

Most importantly, none of this would have been possible without the unconditional love, patience and support of my family. My family to whom this dissertation is dedicated to, has been a constant source of love and strength. I am indebted to my parents for raising me and providing me with extensive educational opportunities. I am grateful for my wife Yun Zhou for continuously encouraging me and being my lucky star. I would like to express my heart-felt gratitude to my family.

Table of Contents

List of Tables

List of Figures

Chapter 1: Introduction

1.1 Hydrogen Economy

"Yes, my friends, I believe that water will one day be employed as fuel, that hydrogen and oxygen which constitute it, used singly or together, will furnish an inexhaustible source of heat and light, of an intensity of which coal is not capable… I believe, then, that when the deposits of coal are exhausted we shall heat and warm ourselves with water. Water will be the coal of the future."

— Jules Verne's novel The Mysterious Island

1.1.1 The Idea of Hydrogen Economy

French novelist Jules Verne may be one of the earliest people with the thoughts of hydrogen economy. As early as 1874, he articulated in his novel "The mysterious Island" the idea of splitting water to generate hydrogen and oxygen and recognized that hydrogen is a valuable fuel which can be used to satisfy the energy needs of the society. As a visionary prophet, Verne wrote about air and underwater travels before the navigable aircraft and practical submarines were invented, and wrote about space travels even before any means of space travel had been devised.

Jules Verne would be pleased, though not surprised to see that more than a century and a quarter later, the idea of using hydrogen as the "coal of the future" is

beginning to move from the pages of scientific fiction into the experiments in laboratories and lexicon of political and business leaders.

The term *hydrogen economy* was coined by John Bockris during a talk he gave in 1970 at General Motors (GM) Technical Center [1]. Central to the hydrogen economy is that the energy is derived from reacting hydrogen with oxygen using the fuel cell technology to power automobiles, buildings and portable electronics. Figure 1.1 shows the elements of the hydrogen economy. A hydrogen economy could solve the two major problems currently facing the world: the energy crisis and the environmental deterioration [2].

Figure 1.1 Elements of the hydrogen economy (from US Department of energy website, http://www.hydrogen.energy.gov/systems_integration.html)

In the current hydrocarbon economy, oil, coal, and natural gas have powered cars, power plants and factories, causing the anthropogenic buildup of greenhouse gases in the atmosphere. Global warming as a result of the accumulation of CO_2 is not a new concept. Figure 1.2 presents the famous Keeling Curve [3, 4] which shows the variation in concentration of atmospheric carbon dioxide since 1958. Atmospheric CO_2 has increased from about 275 ppm to about 380ppm during the 50 years between 1960 and 2010.

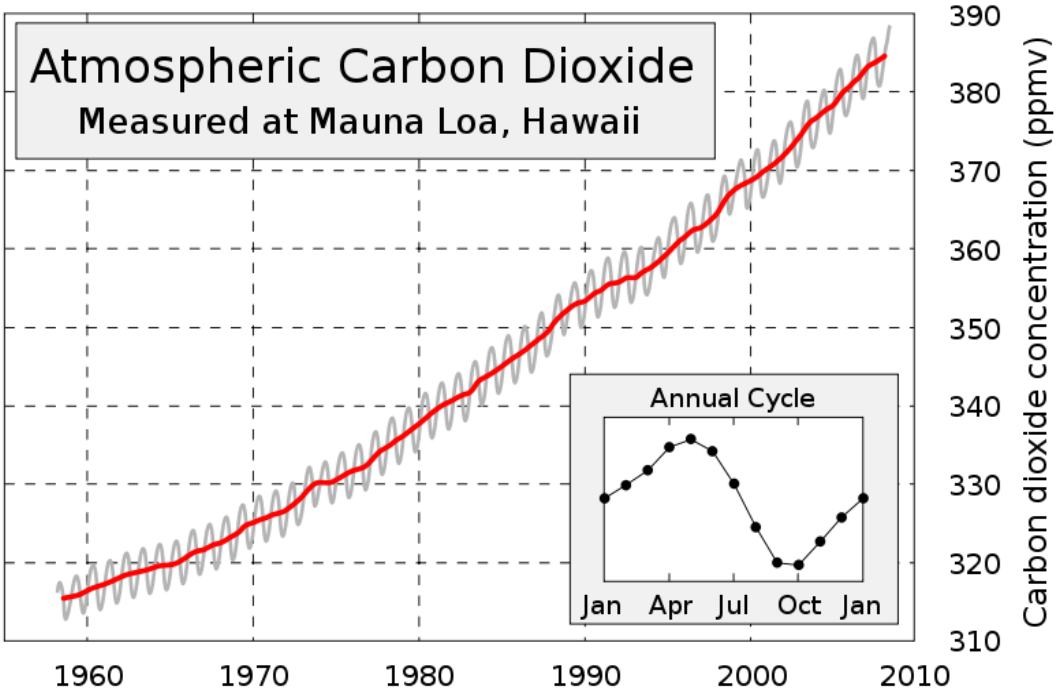

Figure 1.2 Keeling curve of atmospheric carbon dioxide concentration (from Wikipedia, http://en.wikipedia.org/wiki/Keeling_Curve)

Using hydrogen as a fuel offers many advantages. The first and the most important virtue of using hydrogen is its near pollution-free nature. When burned, the main reaction product is water vapor without emission of greenhouse gases. Secondly, since hydrogen fuel has the highest H to C ratio (∞), the use of hydrogen completes the decarbonization trend that has accompanied the evolution of energy sources for mankind over the centuries. In Figure 1.3, coronene, heptane, methane and hydrogen are major compounds for coal, petroleum, natural gas and hydrogen, respectively. The history of fuel usage in the past 2000 years has consistently moved in the direction of a cleaner fuel with H to C ratio increased from 0.5 in coronene to infinite in hydrogen fuel. Furthermore, the production and use of hydrogen can greatly reduce the dependence on oil and natural gas.

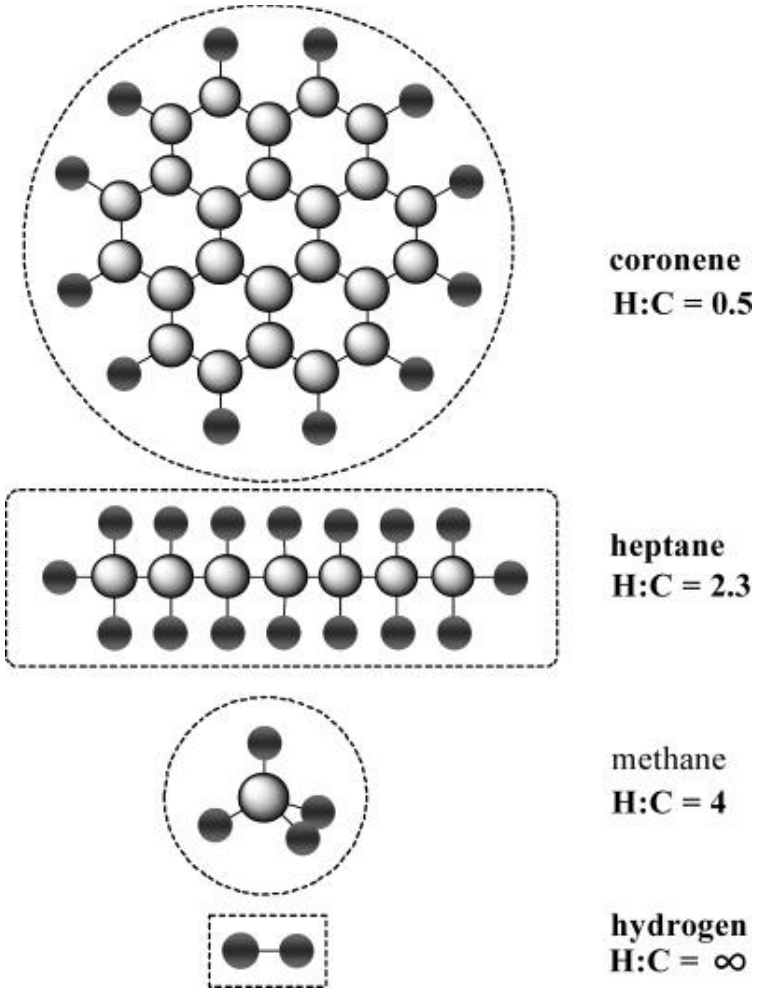

Figure 1.3 H/C atomic ratios in different hydrogen-containing molecules [5]

1.1.2 Hydrogen as a Clean Fuel of the Future: Physical and Chemical Properties of Hydrogen

Hydrogen is considered as a nonpolluting and inexhaustible energy carrier for the future due to its unique physical and chemical properties. In the context of hydrogen economy, hydrogen, the most abundant element in the universe, is an energy carrier, not an energy source.

Hydrogen atom is the lightest element in the universe. The molecular hydrogen is colorless, odorless, tasteless, and nontoxic. Hydrogen has a density of 0.09kg/m^3 which is about 14 times lighter than air [6]. Hydrogen has a low solubility in traditional solvents. However, its solubility is much larger in metals. Adsorption of hydrogen in steel can cause "hydrogen embattlement", which can result in the failure of chemical processing equipment. Compared with other fuels, hydrogen diffuses much rapidly in air with a diffusion coefficient in air of 6.1cm^2/s [7] at room temperature. The rapid dispersion rate is a great advantage of hydrogen as a fuel. Diffusion will cause the concentration decrease below the lower flammability level much faster.

Molecular hydrogen is comparatively non-reactive at ordinary conditions (room temperature, 1 atmosphere pressure). However it can be very reactive in contact with an oxidizer and selected surfaces. Hydrogen atom, is very reactive. Atomic hydrogen is a strong reducing agent. It can react with the oxides and chlorides of many metals such as silver, copper, lead to produce the free metals. When hydrogen reacts with oxygen in either combustion or a fuel cell, the reaction product is water vapor. However, the process can be much accelerated by an electric spark.

Hydrogen has the highest energy content on a mass basis, which makes it a good candidate for the rocket fuel. However, on a volume basis, hydrogen performs worse than gasoline. Therefore, a larger container is needed to power a hydrogen vehicle for an adequate driving range.

The combustibility properties of hydrogen are also different from the conventional fuels. Its properties include high flame speed (3.46m/s), high auto ignition temperature (585^{o}C), high stoichiometric air/fuel ratio for complete

combustion (34:1), low ignition energy (0.02mJ), small quenching distance (0.64mm), and very wide range of flammability (4-75% in ambient air) [6]. Those properties must be carefully considered when design a hydrogen combustion apparatus.

Similar to a gasoline engine, hydrogen can be used directly as a fuel in an internal combustion engine. Due to its unique fuel properties, hydrogen fueled spark-ignited (SI) engine can offer many advantages over a gasoline engine, such as less knocking tendency and lower NO_x emissions. However, many parts of a conventional internal combustion engine must be redesigned in order to prevent premature ignition and knock when using hydrogen as a fuel. For illustration, BMW has developed a bi-fueled internal combustion engine which is modified to allow for the combustion of hydrogen as well as gasoline (Figure 1.4).

Figure 1.4 The internal combustion engine for Hydrogen 7 vehicle by BMW (from www.hydrogencarsnow.com)

In the hydrogen economy scenario, the hydrogen fuel cell is the best candidate for hydrogen usage [6]. A hydrogen fuel cell converts the chemical energy stored in hydrogen directly into electrical and thermal energies. At the anode, the hydrogen fuel breaks down into electrons and ions with the help of anode catalysts. The electrons travel through a load, while the ions travel through the electrolyte to the cathode. At the cathode, the electrons are reunited with the ions and the two react with oxygen to produce water as the only product. The overall reaction is:

$$H_2 + \frac{1}{2}O_2 \rightarrow H_2O$$

Since the voltage of an individual fuel cell is low (The reversible thermodynamic limit is 1.23V.), fuel cells are usually combined into a fuel cell stack. There are many types of fuel cells. The most investigated types are proton exchange membrane fuel cell, solid oxide fuel cell, and molten carbonate fuel cell. Each fuel cell has its own optimum operation temperatures and applications. The proton exchange membrane fuel cell is considered the most suited for fuel cell vehicle applications due to its high power density, low operation temperature, and quick start-up. However, high cost and short durability prevent the current fuel cells from mass applications. Efforts are under way to improve the durability and reliability as well as to reduce the manufacture cost of fuel cells.

1.1.3 Current Hydrogen Economy and Future Challenges

Despite its attractive properties, hydrogen is not readily available for use as a fuel. It exists in bound form with other elements (e.g. water, hydrocarbons). In general, hydrogen can be prepared in different ways. The most mature, thermodynamically efficient processes today involve removal of hydrogen from hydrocarbons. Currently, industry generates about 50 million metric tons of hydrogen (If burned, will release about 6000 GJ of energy) globally each year and is expected to increase by about 10% per year. Hydrogen is primarily produced (96%) from fossil fuels with only 4% from water by electrolysis [5]. Currently, hydrogen is consumed primarily as an industrial feedstock. About 60% of the hydrogen is used to produce NH_3 by the Haber process [8], and about 40% is consumed in refinery, chemical and petrochemical industries. A small percentage of hydrogen is used by food producers [5].

Currently, industrial hydrogen is produced by steam reforming of natural gas, which consists of two reactions. The first reaction $CH_4 + H_2O \rightarrow CO + 3H_2 (\Delta H_{298} = 206 kJ/mol$, 0.24 mole of methane needs to be burned to provide the heat) operates at relatively high temperature (700–1100 ℃), requiring relatively large energy input. The second reaction involves the water gas shift reaction: $CO + H_2O \rightarrow CO_2 + H_2 (\Delta H_{298} = -41 kJ/mol)$, which occurs at lower temperatures. With this reaction additional hydrogen is recovered and CO removed from the steam reforming process. However, the water gas shift reaction is a major source of industrial CO_2, a major greenhouse gas species. If the CO_2 by-product cannot be fully used or sequestrated, the environmental gain from using hydrogen as an alternative fuel to hydrocarbons is largely reduced. Thus, in order to make sustainable use of hydrogen energy, the production of hydrogen should use renewable forms of energies and must be

environmental friendly.

1.2 Nanoparticles and Aerosols

1.2.1 Aerosols

Aerosols refer to an assembly of liquid or solid particles suspended in a gaseous medium long enough to be observed or measured [9]. Examples of aerosols include dust, smoke, fume, cloud, fog, mist and haze. Aerosols are at the core of environmental problems such as global warming, ozone depletion, acid rain, photochemical smog and air quality [10]. Natural and human-made aerosols found in ambient or in industrial process gas streams, come with a great diversity in size, mass, surface area, shape, density, and chemical compositions. Aerosols can be desirable such as the one used in catalysis or as the building blocks for new materials. Aerosols can also be undesirable. Undesirable aerosols are environmental pollution and contamination, and can threaten human health.

Size is probably the most fundamental parameter of an aerosol. For a spherical particle, the size can be simply characterized by a single parameter, particle diameter. Clearly, for more complex particles, more parameters are needed. Fractal dimension is often used to characterize fractal aerosols. The size range of aerosols covers entire five decade from 0.001 to 100 micrometers [11]. In particular, aerosols of diameter smaller than 100nm, which are usually referred as nanoparticles or ultrafine, have

received considerable interest due to their unique behaviors, properties and potential applications in catalysis and energy research. It is in this size range that aerosols science and technology meets with nano science and technology.

Aerosols are two phase systems: a gas or gas mixture, and the particles suspended in it. Thus, the behavior of the particles within the system largely depends on the interaction between the gas medium and the particles. Particles less than 0.1 micrometers in size are affected by the motion of individual gas molecules. Particles of larger size can be treated as surrounded by a continuous gaseous media. Many gas molecules collide near the particle surface. Intermediated-sized particles may slip by the obstacles. Equations govern the particle motion in the continuum regime need adjustment in order to describe the motion in the transition regime.

1.2.2 Nanoparticles

Nanoparticles refer to dispersive particles with size ranging from a few nanometers to 100 nanometers. Researches on nanoparticles are attracting a great deal of attention due to their potential applications in optoelectronics, catalysis, and magnetic data storage. Nanoparticles exhibit many size-dependent properties that differ significantly from their bulk counterparts. These unique properties are determined by their sizes, surface and electronic structures and inter-particle interactions.

Nanoparticles are the bridge that links single atoms or molecules to bulk structures. The finite size of the particle confines the spatial distribution of the

electrons, leading to the quantized energy levels, which results in the famous quantum confinement effect, which is the foundation of many quantum devices for nanoelectronics [12].

A key property of nanoparticles is their high surface-to-volume ratio. For example, a nanoparticle made of 1000 atoms will have about 25% of its atoms on the surface. The surface atoms have fewer nearest neighbors than the atoms in the body. These coordinatively undersaturated atoms greatly increase the surface energy, thus enhance the atomic diffusion. A high percentage of surface atoms introduce many size-dependent phenomena such as melting temperature depression [13-15], surface melting [16, 17], size dependent structural transformations [18], and size-dependent evaporation [19].

The most important application of nanoparticles is in catalysis [20]. From a practical point of view, catalysts are often expensive (e.g. gold, platinum). It is economical to prepare the catalysts as nanometer-sized particles. Thus, the total surface area exposed to the reactants is maximized; the cost is minimized. From a functional point of view, nanoparticles offer unique catalytic properties since the size of nanoparticle is between molecule and bulk materials. A widely studied topic is size dependent catalytic properties of nanoparticles [21, 22]. The smaller the particle size, the higher the specific surface area for a given amount of sample. Moreover, the high specific area offers better diffusion, which can significantly change the reactivity. El-Sayed et al. [21-23], recently reported synthesis of transition metal nanoparticles of different shape and pointed out the potential usage of different shaped particles in catalysis. Later, they showed that activities of platinum nanoparticles of different shapes are indeed different for the same electron-transfer reaction in colloidal solution. The discovery of

particle shape dependent catalytic properties of nanoparticles adds another degree of freedom for designing advanced catalysts.

1.2.3 Aerosol/Nanoparticle Measurement and Characterization

As nanotechnology progresses with new discoveries, the development of appropriate characterization methods and tools becomes critical. Current advanced nano characterization techniques allow characterization of nanoparticle catalysts on the molecular scale under vacuum and under reaction conditions [12]. A variety of techniques are available for obtaining useful information about aerosol/nanoparticle properties. They can be generally divided into two categories, in-situ techniques and ex-situ techniques.

In-situ characterization methods and tools include various ion-mobility methods, on-line mass spectrometry, and real-time optical detection techniques [9]. Ex-situ characterization methods and tools include X-ray diffraction, electron microscopy, Fourier transform infrared spectroscopy, and thermal optical analysis [12].

Ion-Mobility Methods

Ion-mobility methods are widely used as an in-situ method for aerosol characterization which takes advantage of the motion of charged particles in an electric field. By balancing the electrostatic force with another force on the aerosol particle, the particle size and mass can readily be determined in an ion mobility

instrument. Ion-mobility methods can be employed for particle mass measurement as well as high-resolution particle sizing.

When a charged particle is placed in an electric field, it will migrate with a velocity that depends on the charge on the particle, the particle size and structure. In the Stokes regime, the migration velocity is obtained by equating the electrostatic force to Stokes drag, and solving for the velocity.

$$neE = 3\pi\eta V_e d_p / C_c$$

$$V_e = \frac{neE\,C_c}{3\pi\eta d_p}$$

The electrical mobility Z is thus defined as the velocity of a particle with a charge ne in an electric field of unit strength. It is given by:

$$Z = \frac{V_e}{E} = \frac{ne\,C_c}{3\pi\eta\,d_p}$$

In order to use the ion mobility method, one must know the distribution of charges on particles. Aerosol particles can acquire charges by a number of mechanisms including static electrification, photoemission, thermionic emission, self-charging of radioactive aerosols, and charging by small gas ions [9]. However, not many charging mechanisms can be used directly for ion-mobility measurement because the initial charge state of the aerosol is rarely known. Most ion-mobility instruments employ a bipolar diffusion charging process for particle charging, in which electrically neutral cloud of positive and negative ions migrate to the particles by Brownian diffusion and undergo charge transfer reactions with aerosol particles. The charges used in these instruments are based on ion generation by radioactive decay. It is usually assumed that a Boltzmann equilibrium charge distribution will be

reached for aerosol particles after long exposure to bipolar ion mixtures. The distribution is given by:

$$f_n = \frac{\exp(-\frac{n^2}{2\sigma^2})}{\sum_{k=-\infty}^{\infty} \exp(-\frac{k^2}{2\sigma^2})}$$

where $\sigma^2 = \frac{d_p kT}{2e^2}$. However, the actual charge distribution slightly deviated from the Boltzmann distribution and is asymmetrical [9]. Ion-mobility instruments rely on the equilibrium charge distribution for particle size and mass measurement.

The Differential Mobility Analyzer (DMA)

The differential mobility analyzer is an important tool for on-line particle sizing and particle size distribution measurements. Knutson and Whitby [24] first introduced it as a monodisperse particle source. In a DMA, electrostatic force and drag force are simultaneously applied on aerosol particles. The balance of the two forces determines the size of the aerosol particle. A schematic diagram of a cylindrical DMA is presented in Figure 1.5. The details of the DMA design and operating principle can be found in Knutson and Whitby's paper. In brief, a DMA system is a cylindrical coaxial flow condenser. Aerosol particles enter the DMA through a narrow slot in the outer electrode. A particle-free sheath flow enters the DMA from the top and separates the aerosol from the high-voltage inner electrode. A monodisperse aerosol extraction port is located downstream in the inner electrode. Particles migrate across the gap between the inner and outer electrodes at the same time as they are carried by the sheath flow through the classifier. Particles with higher electrical mobility than the

selected mobility migrate across the annulus, depositing on the central electrode above the aerosol extraction port. Particles with lower mobility deposit further downstream below the aerosol extraction port. Only particles within a narrow mobility range can be selected. The characteristic mobility of the particles at given DMA flow rate and applied voltage Z^* is given by:

$$Z^* = \frac{(Q_{sh} + Q_e) ln \frac{R_2}{R_1}}{4\pi VL}$$

Where Q_{sh} is the clean sheath flow, Q_e is the excess flow. R_1 and R_2 are the radii of the inner and outer electrodes, respectively. V is the applied voltage, and L is the length of the classifier.

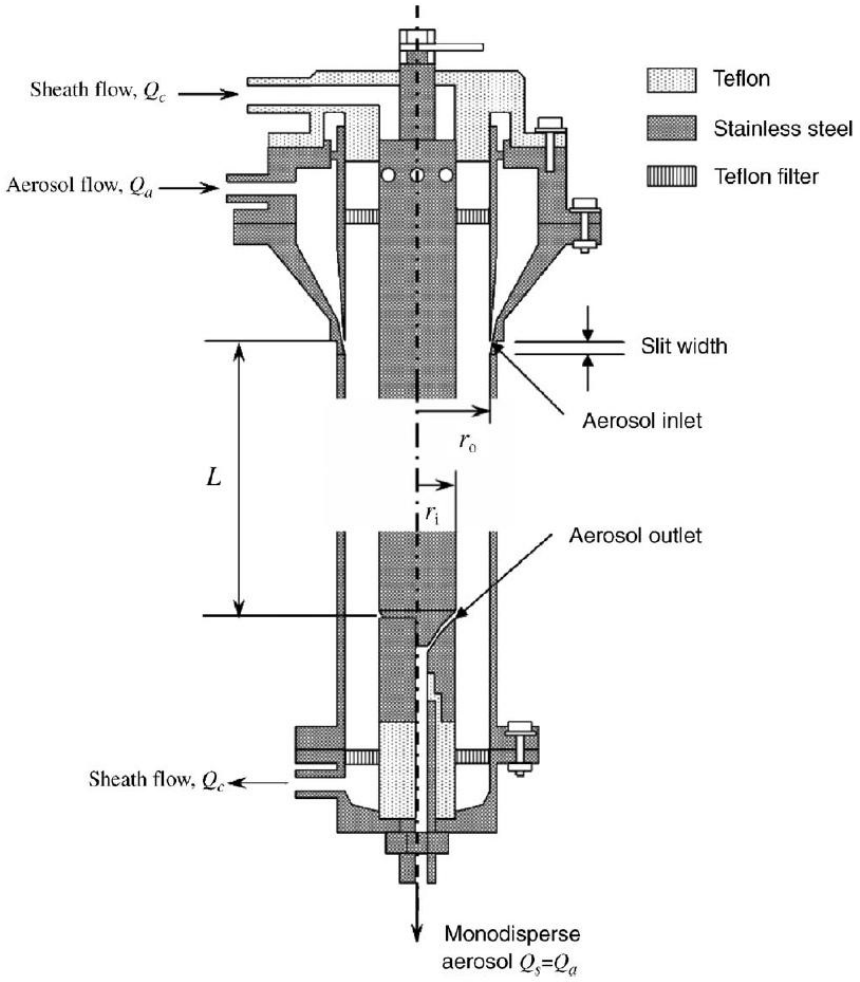

Figure 1.5 Schematic diagram of a cylindrical DMA [25]

The probability of particles with mobility Z that enter the DMA will be included in the classified aerosol flow is called the DMA transfer function. It is closely related with the resolution of a DMA which is defined as the ratio of Z* to the observed range of nobilities of the transmitted particles. If the particles are large enough, diffusion is unimportant. The DMA resolution is bounded by a value that is determined by the ratio of flow rates $\beta = \frac{Q_a + Q_c}{Q_{sh} + Q_e}$, where Q_a is the aerosol flow, Q_c is the classified monodisperse aerosol flow. The resolution is:

$$R_{non-diffusion} = \beta^{-1}$$

For sufficiently small particles, diffusion cannot be neglected. The resolution becomes:

$$R_{diffusion} = 2.66(\frac{fV}{G})^{\frac{1}{2}}$$

Where the factor f accounts for nonuniformities in the electric field along the migration path and G is a parameter that depends weakly on the geometry of the DMA and flow rate ratio β.

The Aerosol Particle Mass Analyzer (APM)

An aerosol particle mass analyzer classifies aerosol particles according to their mass to charge ratio. It works by balancing electrostatic and centrifugal forces applied on the particles. Though the resolution of the mass classification depends on the particle shape, orientation and properties of the surrounding gas, the center of mass selection band only depends on the intrinsic mass of the particles [26, 27].

Figure 1.6 presents a schematic of an APM instrument. The APM consists of two rotating coaxial cylindrical electrodes. The inner and outer electrodes rotate at the same angular velocity. When the aerosol is introduced into the narrow annular space between the electrodes, it rotates at the same angular velocity as the electrodes. Particles pass through the APM experience electrostatic and centrifugal forces acting in opposite directions. When the two forces balanced with each other, there is no net radial force on the particles, and the particles will pass the instrument through the aerosol exit. Particles of a particular mass-to-charge ratio will be selected through the

APM depending on the rotational speed and voltage difference between the electrodes. This method can be used on-line either to generate monodisperse particles, or to measure the mass-to charge distribution together with a CPC.

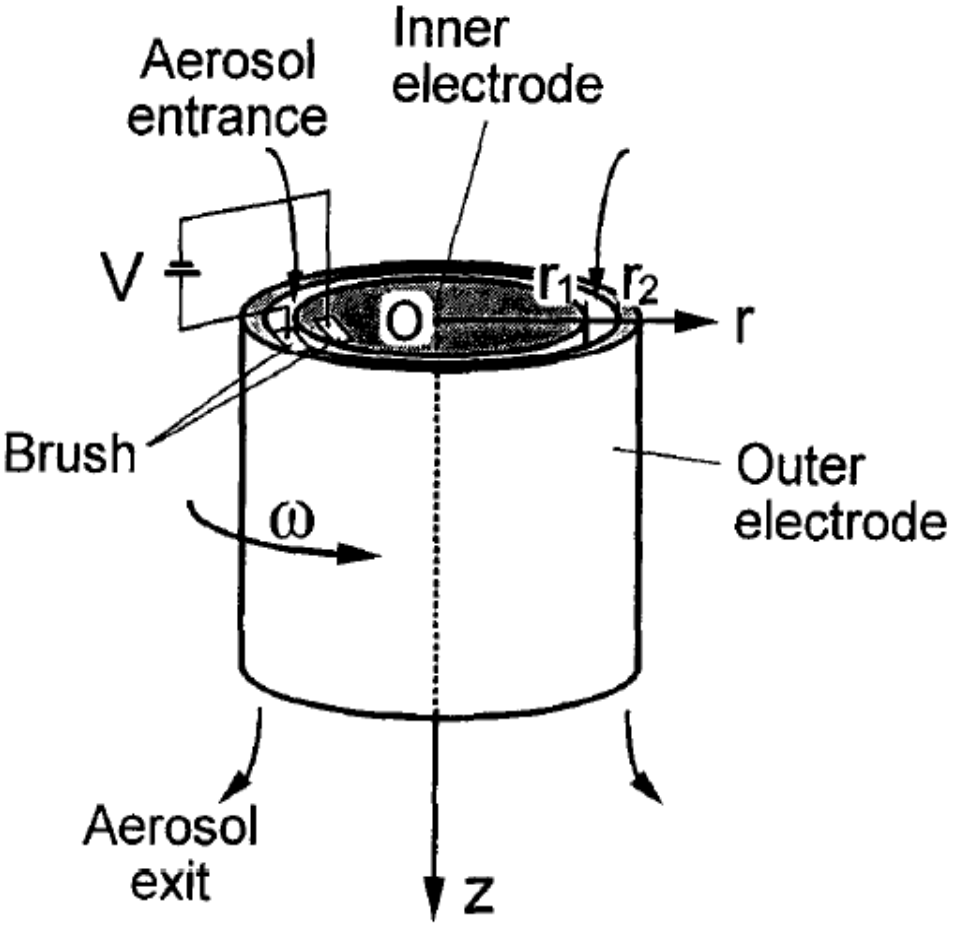

Figure 1.6 Schematic of an aerosol particle mass analyzer [26]

The equations of inside an APM neglecting Brownian diffusion are given by:

$$\frac{m}{\tau}\frac{dr}{dt} = m\omega^2 r - \frac{qV}{r ln(\frac{r_2}{r_1})}$$

Where m is particle mass, q is the charge on the particle, V is the APM applied voltage, ω is the rotational speed, and, τ is the particle relaxation time given as:

$$\tau = \frac{m}{f} = \frac{mC\left(d_p\right)}{3\pi\mu d_p}$$

Where f is the friction factor for a spherical particle with diameter d_p. Particles are classified in the APM according to their mass to charge ratio (specific mass), s_c:

$$s_c = \frac{V}{r_c^2\omega^2 \ln(\frac{r_2}{r_1})}$$

According to the above equation, particle morphology, size, and orientation play no role in particle classification. The APM transfer function is defined as the ratio of exit to inlet particle flux. The analytical solution for APM transfer function for uniform flow through the APM is given by Ehara et al. [26] (1996). The transfer function is a trapezoid such that the height of the transfer function trapezoid is given by:

$$t(s) = e^{-\lambda_c}$$

The base width relative to s_c, which is a measure of the resolution in the classification, is given by:

$$\frac{\Delta s}{s_c} = \frac{4\delta}{r_c}\coth(\frac{\lambda_c}{2})$$

$$\delta = \frac{r_1 - r_2}{2}$$

$$\lambda_c = 2\tau\omega^2 L/v_0$$

Where, λc is the classifier performance parameter, which may be interpreted as the ratio of axial (L/v_0) and radial traversal times ($1/2\tau\omega^2$), and L is the length of APM column.

The Condensation Particle Counter (CPC)

In order to perform the particle size distribution measurement using a DMA or particle mass distribution measurement using an APM, an ultrafine particle counter is required. Since ultrafine particles (smaller than 0.2 micrometer in diameter) could not be detected directly by optical techniques, a pre-growth of ultrafine particles is necessary in a particle counter.

A condensation particle counter is an instrument for detecting ultrafine particles. Three processes are involved in detecting [9], supersaturation of a working fluid, growth of particles by condensation of vapors, and detection of aerosol particles. Modern CPCs induce supersaturation conditions by conductive cooling technique [28-30]. A schematic of a continuous-flow CPC is presented in Figure 1.7. The aerosol passes through a working fluid reservoir kept at an elevated temperature and gets saturated with the working fluid vapor. Then the aerosol enters a lower temperature condenser tube, where gas cooling takes place by conduction and convection. Particles grow by condensation to a near uniform size between 5 and 15 micrometers. Downstream the aerosol flow, a photodetector is placed to measure the scattered light from the aerosol. The intensity of scattered light is used as an indication of the particle concentration.

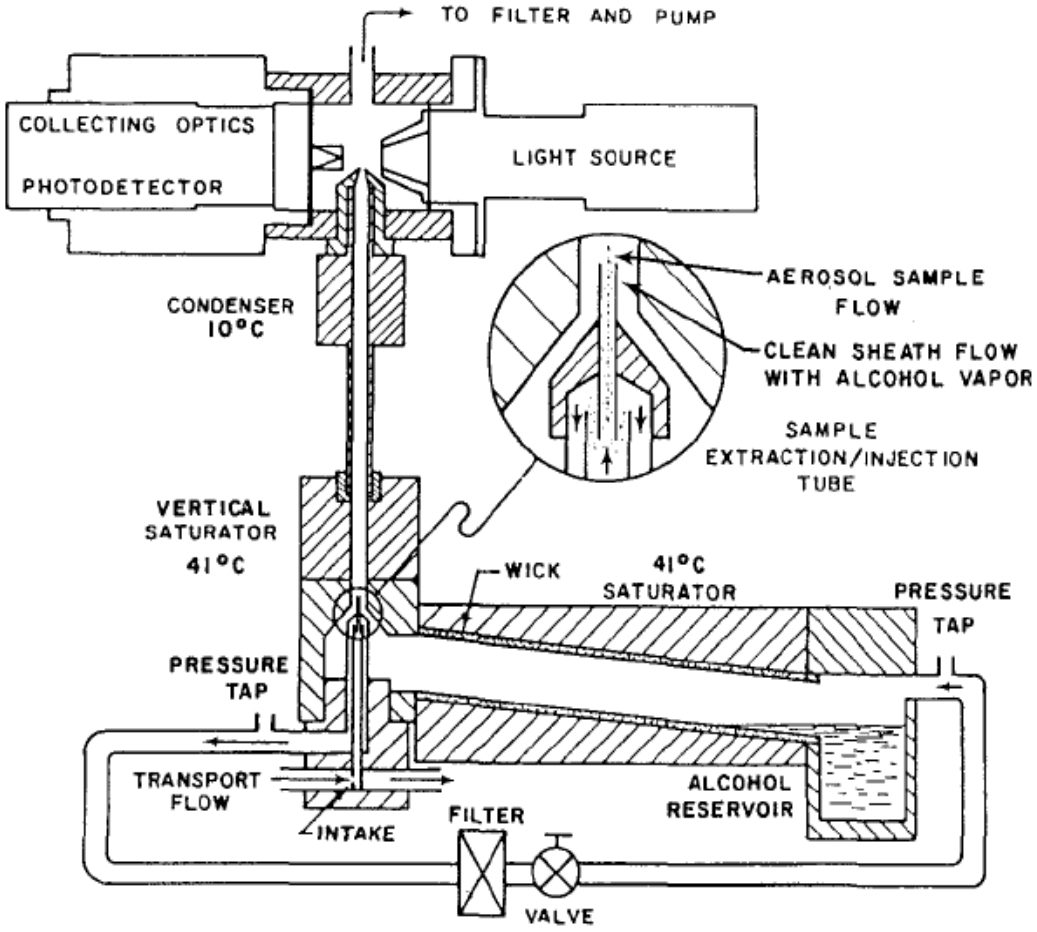

Figure 1.7 Schematic of a continuous-flow CPC [29]

1.3 Solar Thermal Chemical Cycles for Hydrogen Generation

1.3.1 Solar Energy

Hydrogen energy is environmental safe only if it is produced by renewable energies such as solar, nuclear, wind, tidal energies etc... However, each technology has its own drawbacks and limits. Nowotny [31] has summarized the advantages and

disadvantages of each energy source in Table I shown below. According to Nowotny, solar energy is the best candidate for future hydrogen production for the following reasons:

1. Abundance. Most continents have large areas with high levels of sunlight. The "sunbelt" regions of the world include the southwestern United States, southern Europe, all of Australia, and broad regions of the developing world.

2. Cost. Large scale solar-concentrating systems are available. The reflection and concentration of direct isolation can be achieved by using collectors/heliostats. The materials used in photo-chemistry are mostly low cost oxides rather than precious metals and expensive semiconductors.

3. Easy Adaptation. A large scale solar hydrogen generation system can be adapted relatively easily for individual household use. This will promote mass production

Table 1.1 Advantages and disadvantages of common renewable energy technologies (adapted from reference [31])

Technology	Advantages	Disadvantages
Solar-hydrogen energy	Sunlight is renewable Water is renewable Sunlight is abundant Materials are inexpensive Fuel is less expensive than oil (when the technology matures) Hydrogen is generated in one	Requires clear sky Requires increase of conversion efficiency Significant cost in terms of land utilization

	process (photo-electrochemical)	
Wind power	Wind is renewable Operates day and night	Capital cost is high Requires site exposed to high wind
Hydroelectric	Provides both water and power Operates day and night	Requires suitable site (river or lake) Negative environmental impact
Tidal power	Tidal flow is renewable Operates day and night	Limited to coastal areas exposed to high tide
Geothermal power	Operates day and night	Requires access to site of geothermal activity
Photovoltaic	Sunlight is renewable Sunlight is abundant Excess energy may be provided to larger electrical networks	Materials are expensive Processing technology is expensive Clear sky is required
Solar-thermal	Sunlight is renewable Sunlight is abundant Device is simple	Clear sky is required
Biomass	Operates day and night	Greenhouse gases are emitted

The sun is a yellow dwarf star of radius 6.95508×10^7 km which is about 109 times that of earth [7]. It generates energy by nuclear fusion of hydrogen nuclei into helium. The solar spectral ranges from X-ray and gamma ray spectral region to very

long radio wavelength region. The total radiation energy is about 2.845×10^{26} watts [32]. Due to the elliptical shape of the Earth's orbit, the distance between the Earth and the Sun varies during a year. These variations cause the solar radiation intensity at the top of the atmosphere changes from 1414 W/m^2 in December to 1321 W/m^2 in July.

To utilize solar energy for hydrogen generation, there are basically three ways. They are electrochemical, photochemical, and thermochemical [33]. The latter is based on the use of concentrated solar radiation as the high-temperature energy source for driving an endothermic chemical transformation. Five solar routes have been proposed for solar thermochemical hydrogen generation as shown in Figure 1.8.

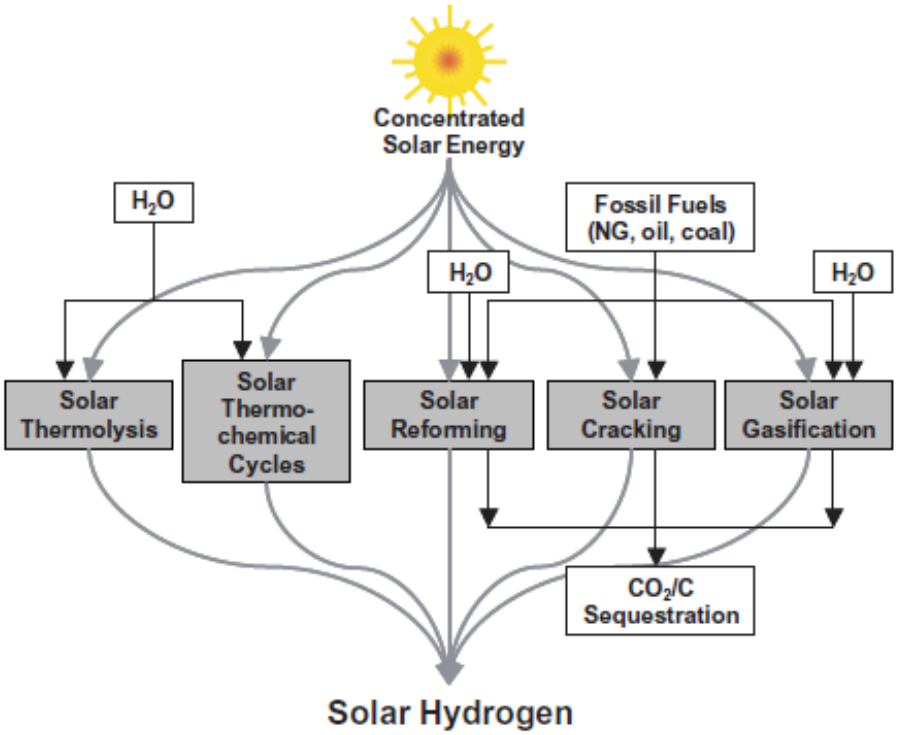

Figure 1.8 Five solar thermochemical routes for hydrogen production [33]

Collectors or heliostats are modern solar concentrating systems [34] which can reflect and concentrate direct solar radiation. Some advanced systems can achieve maximum concentrating factors in the 1500-5000 range, and can provide high temperature solar thermal heat exceeding 1500^{o}C. Such high temperature solar heat can be used to generate chemical fuels.

The efficiency of a solar receiver system for converting solar energy to the chemical free energy stored in the fuels can be calculated by considering the absorption efficiency of the solar receiver and the constraint of second law of thermodynamics. Thus, the system efficiency (theoretical limit) is a product of absorption efficiency and the Carnot efficiency [33].

$$\eta_{solar\_system} = \eta_{absorption}\left(\frac{T - T_L}{T}\right)$$

where T is the operating temperature of the receiver and T_L is the temperature of low temperature reservoir. The absorption efficiency is given by:

$$\eta_{absorption} = \frac{\alpha IC - \varepsilon\sigma T^4}{IC}$$

Where α and ε are the effective absorptance for solar radiation and the emittance of the receiver, I is the intensity of the solar radiation, C is the concentrating ratio of the solar concentrating system and the σ is the Stefan-Boltzmann constant.

Based on the analysis by Steinfeld [33], solar thermochemical production of hydrogen can be competitive with the solar electrolysis of water, and might become competitive with conventional fossil-fuel based processes under certain conditions.

1.3.2 Thermochemical Cycles for High Temperature Solar Hydrogen Production

However, even with these attractive advantages, efficient conversion of solar energy to hydrogen fuel is still a scientific and engineering challenge. The current state of solar technology cannot make the hydrogen price sufficiently low for daily transportation use.

Water is the most abundant hydrogen source on earth. The ideal scenario for hydrogen economy is to generate hydrogen from water. Hydrogen can be obtained from water by electrolysis. Fujishima and Honda [35] in 1972 demonstrated the first water electrolysis using only solar energy. Since then, there have been increased R&D activities on solar photo-electrochemical hydrogen generation. The major challenge of improving yield is to find novel photo-sensitive materials and develop advanced technology of photo-electrodes. Compared with electrochemical water splitting, direct water splitting (Solar energy is used directly to decompose water into hydrogen and oxygen) enjoys a higher efficiency theoretically, because there is no energy loss during the heat to electricity transformation [34]. However, even with the high temperature obtained using the current solar-concentrating system (about 1500 ℃), direct thermo water-splitting is extremely hard to achieve. The Gibbs free energy for the reaction $H_2O \rightarrow H_2 + 0.5O_2$ equals zero at a temperature of about 4300K. Given the current state of high temperature material technologies, it is too difficult even to build a reactor to sustain this reaction. Another big problem for the implementation of direct water splitting is the recombination of products and intermediates. High temperature gas separation is a big challenge. To overcome the

two shortcomings of direct water splitting, various kinds of multistep thermo-chemical water splitting cycles have been proposed and demonstrated. The concept of the whole process is shown in the following flow chart [34]: *solar radiation → collectors or heliostats → heat on receiver or in reactor → reactants (H_2O, metal oxide, etc.) → regeneration of the reactants, except for H_2O → product fuels extraction (H_2, O_2)*

Of all the multistep water splitting reactions, two-step cycles are the simplest. According to Nakamura [36], various two-step thermal-chemical cycles can be classified into three types:

Oxide type:

$$XO \rightarrow X + \tfrac{1}{2}O_2$$

$$X + H_2O \rightarrow XO + H_2$$

Hydride type:

$$XH_2 \rightarrow X + H_2$$

$$X + H_2O \rightarrow XH_2 + \tfrac{1}{2}O_2$$

Hydroxide type:

$$2XOH \rightarrow 2X + H_2O + \tfrac{1}{2}O_2$$

$$2X + 2H_2O \rightarrow 2XOH + H_2$$

Of the three two-step water splitting cycles, the metal oxide type cycles are the most investigated ones. It is also Nakamura who first proposed a two-step water-splitting cycle based on Fe_3O_4/FeO redox pair [36]. The two reactions of this cycle proceed as follows:

$$Fe_3O_4 \rightarrow 3FeO + \tfrac{1}{2}O_2$$

$$H_2O + 3FeO \rightarrow Fe_3O_4 + H_2$$

Basic thermodynamic properties have been estimated for this cycle including enthalpy of reaction and the change of Gibbs free energy with temperature. It is believed that the first reaction (thermal reduction of Fe_3O_4) proceeds at temperatures above 2500K while the second reaction (hydrolysis of FeO) occurs at temperatures below 1000K.

Similar thermodynamics analysis has been conducted for other redox pairs such as ZnO/Zn, SnO_2/Sn, Mn_3O_4/MnO, Co_3O_4/CoO, In_2O_3/In etc [37-41]. Compared with the iron cycle, Mn_3O and Co_3O_4 have lower reduction temperatures but the hydrogen yield from the MnO and CoO hydrolysis reactions is very low. For SnO_2/Sn and In_2O_3/In cycles, the reduction temperatures are much higher than Fe_3O_4, which creates a big engineering challenge.

1.3.3 Zn/ZnO Thermochemical Cycle

The ZnO/Zn redox pair has been proposed in addition to iron oxide cycles as a potential candidate for future solar chemical water splitting [33, 42]. The production of solar hydrogen via the Zn/ZnO water-splitting thermochemical cycle consists of solar endothermic dissociation of ZnO and non-solar exothermic hydrolysis of Zn.

The reactions are:

$$ZnO \rightarrow Zn(g) + 1/2O_2$$

$$Zn + H_2O \rightarrow ZnO + H_2$$

The advantages of Zn/ZnO solar thermochemical cycle are:

1. Low hydrolysis temperature. The thermodynamic analysis shows that hydrolysis by metallic zinc can proceeds at temperatures below 1400K under 1 bar [43]. The theoretical upper limit of solar energy to hydrogen energy conversion efficiency is 44% with complete heat recovery during quenching and hydrolysis, and 29% without any heat recovery.

2. Moderate ZnO reduction temperature. The reduction of ZnO to Zn occurs at a temperature less than the Fe_3O_4 reduction temperature and can be achieved by modern solar technology. Thermogravimetric (TGA) experiments have shown that the dissociation of ZnO occurs at about 1273K [44]. The production of Zn from ZnO reduction has been experimentally demonstrated using a solar chemical reactor [45, 46].

3. Logistical advantages. Zn can be transported easily to the reaction site. This eliminates complications associated with the transportation and storage of H_2

The interest in this dissertation focuses on the second step of the ZnO/Zn cycle, the Zn hydrolysis reaction. The Zn hydrolysis reaction has been studied in various forms over the years. However, a detailed, intrinsic reaction mechanism and kinetics for Zn nanoparticle hydrolysis reaction is still lacking.

1.4 Hydrogen Generation by Fuel Decomposition

Production of hydrogen from renewable energy-based water splitting processes (solar thermochemical, solar water splitting, photovoltaic water electrolysis) has the potential of providing us with environmental-friendly and cost-efficient energy solutions. However, it is generally understood that those processes are complex and

would be unlikely to reduce the hydrogen cost by a significant amount in the near future [5]. Currently, more than 96% of hydrogen generated globally is from fossil fuels, only 4% of hydrogen is produced from water electrolysis. It can be predicted that in the near- to medium-term future, hydrogen generation will continue to rely on fossil fuels. Various processes have been developed for hydrogen production from fossil fuels. Those processes can be divided into two major categories (oxidative processes versus nonoxidative processes) based on the role of oxidants [47-49].

1.4.1 Hydrogen Production from Fossil Fuels with CO_2 Generation

Oxidative processes convert fossil fuels into hydrogen in the presence of an oxidant which can be oxygen, steam, CO_2 or a combination thereof. Due to the oxidative nature of the processes, CO_2 or CO is co-produced. Most industrial hydrogen generation techniques such as steam reforming, partial oxidation and autothermal reforming belong to this category.

Steam reforming of methane is by far the most widely used and important process for industrial hydrogen production [6]. It accounts for about 40% of the total hydrogen production. The technology of steam methane reforming (SMR) is well developed. The details of this process are discussed in section 1.1.3. SMR is usually carried out in a catalytic environment. Ni and some noble metals are known to be catalytically active for this process. The reaction mechanisms on those catalysts have been studied and summarized by [50-52]. The catalytic activity of metals generally follows the trend [53].

Ru > Rh > Ir > Ni > Pt > Pd

The noble metals were first used in this process and are proved to be more active than Ni, but the cost makes their use prohibitive. Ni based catalysts are the most widely used because they are more prone to deactivation by coking and relatively low cost [54]. Solid carbon in the form of carbon fibers or filaments usually forms during the process from the surfaces of Ni particles. CO and methane decomposition are the major reactions for carbon formation. Solid carbon deposits can lead to the degradation of the catalysts. The catalytic activity of the catalytic systems depends not only on the surface concentration of the active sites but also on the support of catalyst which determines the resistance to sintering, coke deposition and dispersion of the catalytically active particles [55].

The steam reforming process has also been studied for liquid hydrocarbons as well as for methanol. Compared with methane steam reforming, the higher tendency for carbon formation from liquid hydrocarbon process creates significant problems. In order to solve the carbon deposition problem, catalytic pre-reforming process has been developed, in which higher hydrocarbons are converted into methane and carbon oxides.

Other than water vapor, carbon dioxide can be used for methane reforming [56]. The process is called "dry reforming". The major reaction is as follows:

$$CH_4 + CO_2 \rightarrow 2CO + 2H_2 \left(\Delta H_{298} = 247.4 kJ/mol\right)$$

The reaction is more endothermic than steam reforming and requires high operational temperature (800-1000^{o}C) and low pressure to achieve best conversion. In addition to Ni and noble metals [57], perovskite oxides and transition metal carbides [58-60] are

considered as catalysts for this process. Equilibrium calculation shows that at temperature below 800°C, solid carbon is the major product components. Thus, this process is prone to giving more carbon deposition. The dry-reforming process is getting more attention recently due to the idea that CO_2 can be converted. However, if the objective were to produce hydrogen, the process releases the same amount of CO_2 as steam reforming due to the water gas shift reaction. If the objective were to produce syngas, then CO_2 will be sequestered in the form of synthetic fuel for Fischer-Tropsch process.

Partial oxidation of hydrocarbons is an attractive alternative in industrial hydrogen production. It requires less energy input than steam reforming and can process heavy hydrocarbons or even residual oils with high content of sulfur and heavy metals [55]. Due to the addition of sufficient oxygen, the overall process is exothermic. Hydrogen produced from heavy residual oil using partial oxidation method has been practiced commercially by Shell and Texaco [61]. However, expensive oxygen plant is the obstacle that keeps this process from becoming the major hydrogen production process. The generic reaction equation can be written as:

$$C_m H_n S_p + \frac{m}{2} O_2 \rightarrow mCO + (\frac{n}{2} - p) H_2 + pH_2S$$

Besides the above equation, numerous other reactions can also occur in the process. These include feedstock decomposition (cracking) reaction, solid carbon (coke) partial combustion, coke water reforming reaction as well as water gas shift reaction, CO_2 reforming and methane reforming reactions. Due the complex nature of this process, no detailed mechanism of hydrogen production from hydrocarbons higher than methane has yet been established. A general trend in partial oxidation is that

aromatics are less reactive than n-alkanes and more prone to carbon deposition than paraffins and cycloparafins.

The catalysts used in the partial oxidation process are similar to those in the steam reforming process. They are supported Ni, Co and noble metal catalysts [57, 62, 63]. In addition, pyrochlore oxides and perovskite oxides [57] are also considered.

The last major process in oxidative fossil fuel conversion for hydrogen production is autothermal reforming [64]. In brief, the autothermal reforming process is a combination of steam reforming and partial oxidation, in which the heat produced by partial oxidation (internal combustion) is used to drive the steam reforming reaction in an adiabatic reactor. The reactor usually consists of a burner, a combustion zone and a catalytic zone. Therefore, the main advantages of this process are high energy efficiency, high temperature thus high fuel to hydrogen conversion. The main disadvantage of this process is the high cost of oxygen as in the partial oxidation process. Since the process is a combination of partial oxidation and steam reforming, the active catalysts are the same as those processes. However, due to the high operation temperature, both the catalysts and the support for ATR must have high thermal stability.

1.4.2 CO_2 Free Processes for Hydrogen Production from Hydrocarbons

Hydrocarbon decomposition is an attractive alternative for hydrogen production without greenhouse gas emissions. The concept of this process is simple. When sufficient energy is provided to heat hydrocarbons, they can thermally decompose

into their hydrogen and carbon constituents [65]. The general equation can be expressed as:

$$C_nH_m \rightarrow nC + \frac{m}{2}H_2$$

The most important advantage of thermal decomposition of hydrocarbon process is its carbon oxides free nature. Since no oxidative compound is added, the product is free of greenhouse gases. Without CO formation, there is no need for the energy intensive water gas shift reaction and CO_2 removal steps. Furthermore, because only solid carbon structures and hydrogen gas are produced during the process, separation of products is not a big issue.

In fact, thermal decomposition of hydrocarbon has been practiced since the 1950s [66]. This process which is also called thermal black process was employed by carbon black manufacturers for the production of carbon black with hydrogen as a byproduct and supplementary fuel.

Among all the hydrocarbons, methane decomposition has received most attention due to the availability of natural gas. The methane decomposition reaction can be expressed by the following equation:

$$CH_4 \rightarrow C + 2H_2 (\Delta H_{1073K} = +90.1 kJ/mol)$$

The sp^3 hybridization of the atomic orbitals makes the methane molecule very stable. The carbon-hydrogen bond energy in methane is $439 kJ/mol$, which is one of the highest among all the organic compounds. The lack of polarity and any functional group in its electronic structure also contributes to the high thermal decomposition temperature of methane.

For pure thermal decomposition of methane, the reaction mechanism has been

extensively studied [67]. Besides solid carbon and hydrogen gas, other compounds may also form during methane decomposition, depending on reaction kinetics and conditions. The overall mechanism can be summarized as a stepwise methane dehydrogenation process [68]:

$$2CH_4 \rightarrow C_2H_6 \rightarrow C_2H_4 \rightarrow C_2H_2 \rightarrow 2C$$

The initial homogeneous methane dissociation reaction induces the free radicals which lead to the formation of ethane. A sequence of dehydrogenation reactions transfers ethane into acetylene. Due to the high soot tendency of acetylene, a series of fast reactions lead to the production of higher unsaturated hydrocarbons and then aromatics and finally solid carbon.

A number of catalysts such as transition metals [65] (Ni, Co Fe), carbon-based catalysts [69] have been investigated for the catalytic methane decomposition process. Transition metals are known to be active for breaking C-H bonds in methane molecules in a wide range of temperatures. While carbon-based catalysts are efficient at a higher temperature range. Muradov [47, 65] used pulse and continuous flow reactors to study the activities of a number of supported transition metal including Pt, Mo, Fe, Ni and Co for catalytic methane decomposition. Fe and Ni based catalysts were found to be most active. Matsukata [70] conducted a series of experiments and found that among Cu, Fe, Ni and W metals, only Ni was active in methane decomposition at low temperatures. Au et al. [71] [72] have conducted a theoretical study to describe the methane decomposition processes on transition metal surfaces. Theoretical methane dissociation energies on a number of transition metals were calculated. They found that there is significant reduction in the dissociation energy on metal surfaces due to

the formation of strong M-CH_{x-1} and M-H bonds. The total dissociation energies of methane on metal surfaces follow the trend $Rh < Ru < Ir < Os \approx Pt < Pd$, thus Rh is the most favored catalyst thermodynamically. This trend is consistent with Koerts's work [73] in which he demonstrated that the activity order follows:

$$Co, Ru, Ni, Rh > Pt, \mathrm{Re}, Ir > Pd, Cu, W, Fe, Mo$$

All the metal catalysts have the deactivation problem due to the carbon deposit on the catalyst metal surfaces by forming soot, amorphous or encapsulated carbon. However, it is of practical importance if the carbon deposit can form nanometer-sized carbon structures such as filaments, tubes and whiskers due the high value of those products. Recent research interest is to develop the process for simultaneous production of hydrogen and filamentous carbon by catalytic decomposition of hydrocarbons. The detailed mechanism for carbon filaments, carbon nanotube formation can be found in many references [74, 75]. In brief, the dissolved carbon diffuses through metal particles, precipitates at the rear of metal crystallite and forms carbon filament structures. The filament growth stops when the metal particle is encapsulated in carbon layers.

The idea of using carbon-based catalytic materials was proposed by Muradov [48]. The use of carbon materials can overcome several challenges currently facing the metal catalysts such as the catalyst deactivation, sulfur poisoning and separation of carbon from metal particles. A variety of carbon materials including activated carbon, CNT, carbon blacks, graphite, diamond powder have been screened and tested. The catalytic activity follows the order activated carbon > nanostructured carbons (CNTs,

fullerenes) > ordered carbons (graphite, diamond powder). In general, high surface area carbons are preferred which shows the heterogeneous nature of the process.

Compared with gaseous hydrocarbons, liquid hydrocarbons have received less attention. However, decomposition of liquid hydrocarbons for hydrogen generation offers certain advantages over methane decomposition. From a thermodynamic point of view, the decomposition of liquid hydrocarbons is more favorable than the decomposition of CH_4, since less energy is required to produce a unit volume of hydrogen [76]. From a practical point of view, decomposition of liquid fuel is more suitable for onboard hydrogen generation, since the current transportation, storage and dispersal infrastructure for gasoline can be easily modified for other liquid fuels.

Many liquid hydrocarbons have been examined for thermal or catalytic decomposition process for hydrogen generation. Those liquid hydrocarbons include from cycloalkanes [77], commercial kerosene [78] to jet fuel mixture [79]. Fe, Ni and Pt based supported catalysts are among the most studied catalysts. Various binary metal catalysts on different support were also investigated. Depending on the operation temperatures and conditions, the activity order of various catalysts can change. For example, for catalytic kerosene decomposition [80], the H_2 yields at 600^{o}C were higher than at 500^{o}C, the catalysts activities are in the order of Ni/TiO_2 > $Pd–Ni/SiO_2$ > Fe/Al_2O_3 > $Ni–Cu/SiO_2$, whereas the order at 500^{o}C was Ni/TiO_2 > $Ni–Cu/SiO_2$ > $Ni–Pd/SiO_2$ > Ni/VGCF. A more detailed literature review on the current stage of catalytic decomposition of liquid hydrocarbons for hydrogen generation can be found in section 5.1.

1.4.3 Combining Fuel Decomposition Processes with Solar Thermal Energy: Solar Reactors

Using solar energy to drive the endothermic hydrocarbon decomposition reactions to produce hydrogen and carbon is a promising route for sustainable energy production. Performing fuel decomposition reaction in a solar reactor offers several advantages over conventional energy processes. First, since no pollution and potential hazards are produced (if 100% converted), this process is clean and environmental-friendly. Second, the solar-driven process upgrades the value of the fuel by adding solar energy in an amount equal to the enthalpy change of the reaction. Third, since no oxygen or combustion takes place, no carbon oxides will result from the complete process from solar energy to hydrogen.

Some new solar reactor designs have been proposed for this process and tests on these reactors have been performed on methane decomposition. Steinfeld et al., designed a solar chemical reactor features a vortex flow of CH_4 confined to a cavity-receiver and laden with carbon particles that serve simultaneously as radiant absorbers and nucleation sites for the heterogeneous decomposition reaction [81]. The reactor design is presented in Figure 1.9. The details of the rector design can be found in reference [81]. In brief, it consists of an insulated cylindrical cavity that contains a windowed opening, the aperture, to let in concentrated solar power into the reactor. Carbon particles, which serve simultaneously as radiant absorbers and nucleation sites, are injected into the reactor's cavity together with a flow of CH_4 via a tangential inlet port located at the front of the cavity. The chemical products continuously exit the cavity via a tangential outlet port located at the rear of the cavity. Tests with a 5

kW prototype demonstrated the feasibility of the reactor concept for continuous mode of operation.

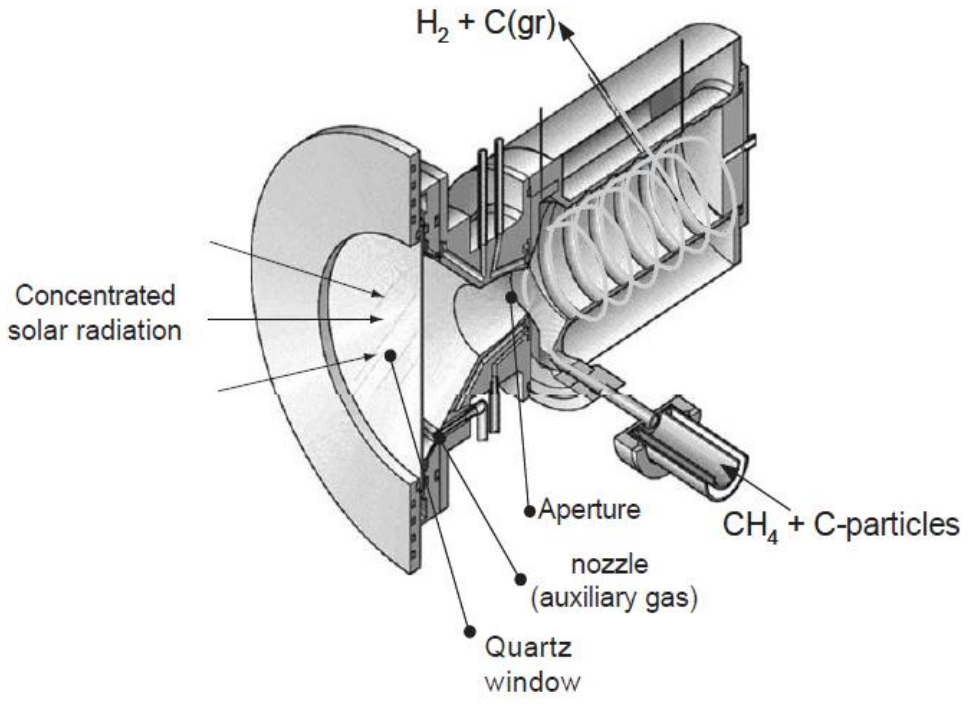

Figure 1.9 Schematic configuration of the solar chemical reactor for the thermal decomposition of CH_4

Bingham [82] reported a solar aerosol reactor design for solar thermal decomposition of methane. The reactor was heated to temperatures in excess of 2000 K using concentrated sunlight. At an average residence time of 0.01s, approximately 90% conversion of methane to hydrogen has been obtained at a reactor wall temperature of 2133 K. The carbon black co-product is ash free, amorphous, and has primary particle sizes of 20–40 nm. Barak et al. [83, 84], performed experimental and simulation work on both the unseeded reactor and seeded reactor for solar thermal

methane splitting. An extent of reaction of 28% was attained. Carbon deposit was a problem.

There is still a pressing need to develop new and improved solar reactor designs.

1.4.4 Catalysts Needs for Hydrogen Generation and Carbon Management

As discussed in previous sections, catalysts are of vital importance in every almost hydrogen generation process. In the solar thermal water-splitting cycles, metals act as both the fuel and the catalyst for the reactions. In the hydrocarbon to hydrogen conversion processes, numerous kinds of catalysts are used. The diagram in Figure 1.10 shows the reaction steps and their catalysts in a commercial natural gas processing unit. The catalytic synthesis of hydrogen from natural gas has been practiced in chemical industry for many years.

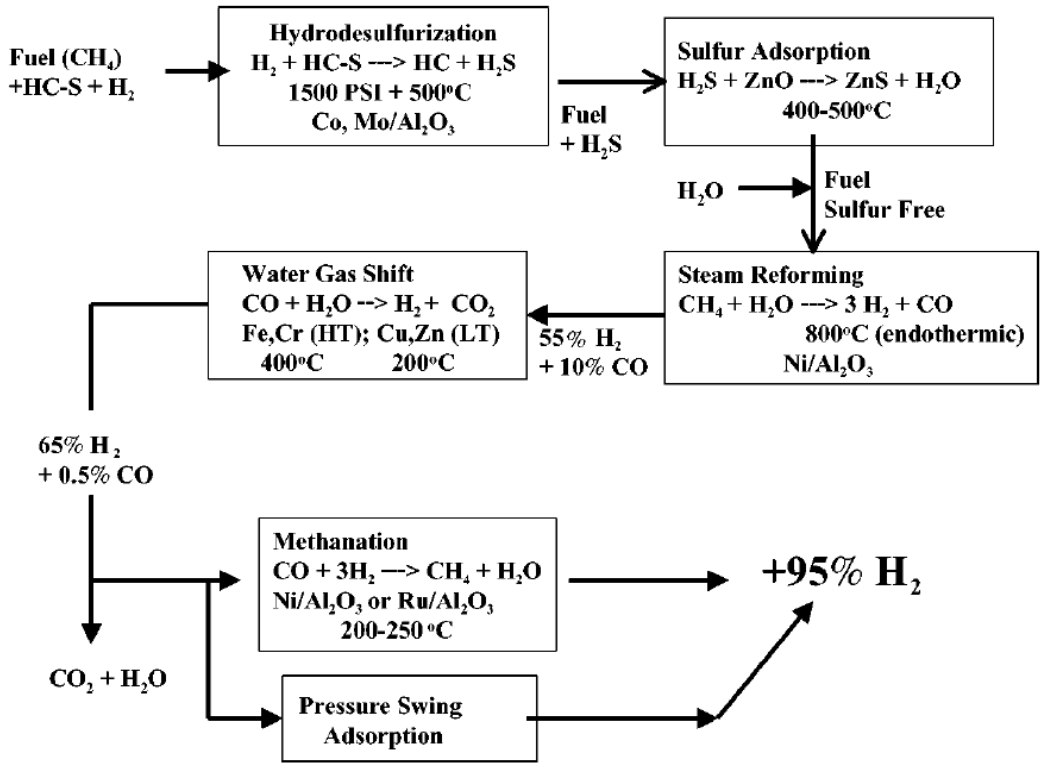

Figure 1.10 reactions and catalysts in a commercial natural gas processing unit (from new materials needs)

However, even for a mature technology such as steam methane reforming, there are many limitations on catalysts. Some of the limitations are: nickel catalysts are extremely sulfur sensitive; active nickel catalysts are also air sensitive, excessive heat will be generated if nickel catalysts exposed to air; coke formation during the process will deactivate the catalyst. Thus, finding more cost-effective active catalysts with diminished tendencies to form coke, a greater tolerance to sulfur, and safe handling properties is still a challenge. Better catalysts for other hydrocarbon to hydrogen processes are also badly needed. Novel process such as catalytic decomposition of

hydrocarbon can be commercialized only when cost-effective, high selectivity and efficient catalysts are developed.

A closely related topic to hydrogen production is carbon management. Hydrogen production is linked to CO_2 as a co-product when fossil fuels are reformed. Currently, steam reforming of hydrocarbons is the largest and the most economical way to produce hydrogen. This situation will not change in the near future as long as natural gas and petroleum based hydrocarbons remain relatively inexpensive. Thus, if the CO_2 byproduct cannot be sequestrated or converted, the environmental gain of using hydrogen as a clean fuel will be lost. To manage CO_2 emission and to convert CO_2 into useful fuels or feedstock, many processes have been proposed as shown in Figure 1.11. Great opportunities exist for advanced catalysts and improved catalytic processes.

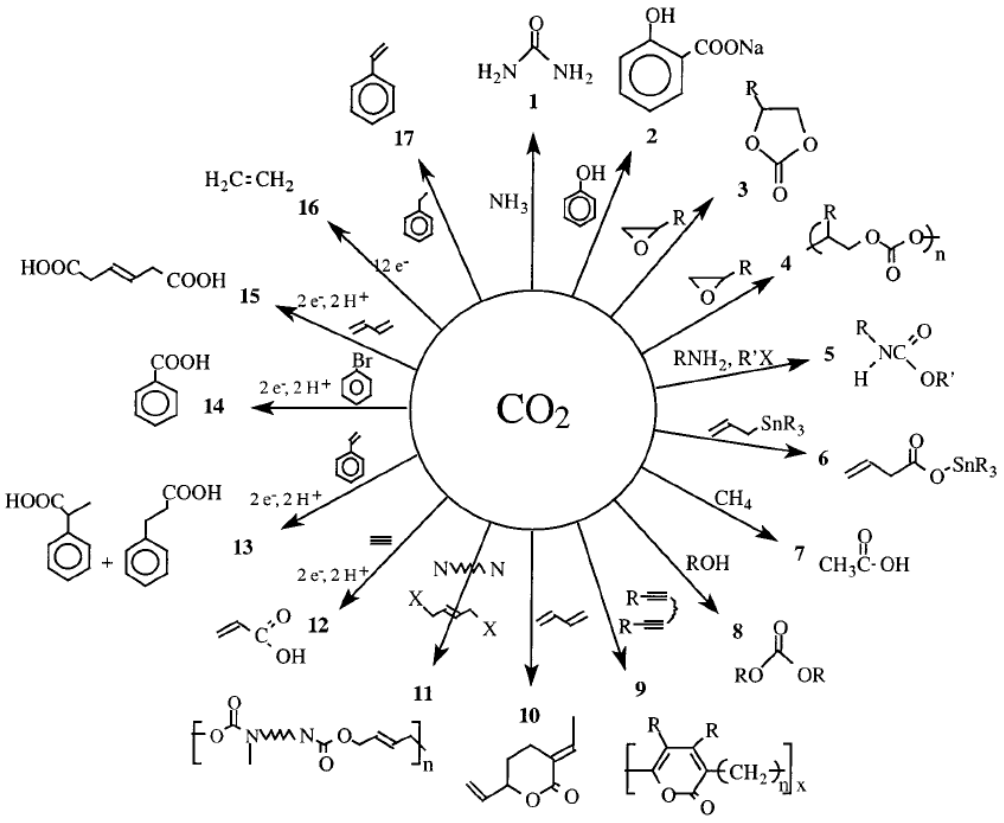

Figure 1.11 Chemical transformation of CO_2

1.5 Scope of the Dissertation

The dissertation focuses on developing and charactering nano-structured materials for solar energy generation and studying the reaction mechanism and kinetics of different solar hydrogen generation processes using nano-structured materials. The experimental work in this dissertation can be divided into two main areas. The first is to study the properties and reactivity of Zn nanocrystals for the solar thermochemical Zn/ZnO water splitting cycle for hydrogen production. The second is concentrated on

the investigation of nanosized metal particles as catalysts for applications in solar fuel decomposition for hydrogen generation and catalytic ignition of liquid fuels.

Chapter 2 describes the study of Zn nanocrystal oxidation and a new oxidation anisotropy effect. In this work, we combine two different ion-mobility schemes in series to study the size resolved oxidation kinetics of zinc nanocrystals (NCs). The first mobility characterization size selects the NCs, while the second mobility characterization measures changes in mass resulting from a controlled oxidation of the NCs. A shrinking core model is used to extract the size-dependent oxidation activation energies, which is observed to be dependent on NC size. We also observed a strong anisotropy effect in the oxidation as imaged by electron microscopy. An oxidation mechanism is proposed that qualitatively explains the oxidation anisotropy and its relationship to the surface energy of the Zn NCs.

Chapter 3 describes observations of evaporation anisotropy of substrate-free Zn NCs. In this work, we determine the onset temperature of evaporation as a function of NC size. The observed shape transformation of free NCs is different from that observed in a traditional hot-stage TEM heating experiments. The onset temperature of evaporation for different size NCs is measured using a tandem ion-mobility and an aerosol mass measurement method. It is found that the onset temperature decreases as the NC size decreases and is analogous to the Kelvin effect. The cohesive energy of bulk Zn is determined to be $1.8 \pm 0.1 ev$ from the size dependent evaporation data. A mechanism based on crystal face dependent surface melting is proposed to explain the evaporation anisotropy effect.

Chapter 4 describes the study of substrate-free hydrolysis of Zn nanocrystals as the second step in a ZnO/Zn solar water-splitting thermochemical cycle. In this work, we combined two different ion-mobility schemes in series to study the hydrolysis kinetics of size-selected zinc nanocrystals (NCs). The first mobility characterization size selects particles with a differential mobility analyzer (DMA). The second mobility characterization employs an aerosol particle mass analyzer (APM) and measures changes in mass resulting from a controlled hydrolysis of the Zn NCs. A low temperature reaction mechanism is proposed to explain the mass change behavior of Zn NCs hydrolysis at 100°C-250°C. An Arrhenius law was used to extract the reaction kinetic parameters. The hydrolysis activation energy and the order of the reaction with respect to water mole fraction were found to be $24 \pm 2 kJ/mol$ and 0.9 ± 0.1, respectively. Based on the proposed reaction mechanism, a complete conversion of 70nm Zn NCs was achieved at 175°C with a residence time of about 10 seconds and water vapor mole fraction of 19%.

Chapter 5 describes the study of catalytic decomposition of liquid fuels (n-octane, iso-octane, 1-octene, toluene and methylcyclohexane) for hydrogen production. The reaction was conducted in a continuous tubular aerosol reactor. The effects of fuel molecular structure and catalyst concentration on the overall hydrogen yield were studied. Iron aerosol particles used as the catalysts, were produced on-the-fly by thermal decomposition of iron pentacarbonyl. The addition of iron catalyst significantly decreases the onset temperature of hydrogen generation as well as improves the reaction kinetics by lowering the reaction activation energy. The activation energy without and with iron addition was 260 and 100 kJ/mol,

respectively representing a decrease of over 60%. We find that with the addition of iron, toluene exhibits the highest hydrogen yield enhancement at 900^{o}C, with a 6 times yield increase over thermal decomposition. The highest H_2 yield obtained was 81% of the theoretical possible, for n-octane at 1050^{o}C. The general trend in hydrogen yield enhancement is that the higher the non-catalytic thermal decomposition yield, the weaker the catalytic enhancement. The gaseous decomposition products were characterized using a mass spectrometer. A XRD analysis was conducted on the wall deposit to determine the product composition and samples for electron-microscopic analysis were collected exiting the furnace by electrostatically precipitating the aerosol onto a TEM grid.

Chapter 6 describes the work of catalytic ignition of liquid fuels (toluene, octane) over the surfaces of in situ generated free metal (Fe, Ni) nanoparticles in an aerosol reactor. The Fe nanoparticles were generated by decomposition of the fuel-soluble precursor iron pentacarbonyl ($Fe(CO)_5$). The Ni nanoparticles were prepared by using gas-phase thermal pyrolysis of nickel tetracarbonyl ($Ni(CO)_4$). The nanoparticles were suspended in Ar environment and injected into the aerosol reactor along with a fuel-oxygen mixture. Under the experimental conditions studied in this work, the catalytic effect is the most significant at high equivalence ratios. Compared with non-catalytic homogeneous ignition, the addition of Fe nanoparticles can lower the ignition temperature of toluene and octane by about 150^{o}C at equivalence ratio of 2.3. The size distributions of Fe nanoparticles was log-normal with a median diameter ranging from 120-170nm depending on the loading of the iron precursor. The size of Ni nanoparticles ranges from 60nm to 100nm. The morphology of catalyst particles

and the product particles were characterized by transmission electron microscopy. The effluent gas product and the fuel ignition temperature were determined by mass spectrometry.

Finally, chapter 7 summaries the work of studying the synthesis of hollow black carbon nanoparticles in gas phase by controlled oxidation method. The formation of the hollow black carbon nanostructure is determined by the elemental carbon to organic carbon (EC/OC) ratio in the original particles and the oxidation conditions that the particles underwent. The effect of the oxidation conditions on the black carbon nanostructure was examined using electron microscopy. A thermal-optical method was used for measuring the elemental carbon concentration in the particles. For the black carbon particles generated by toluene pyrolysis at 900^{o}C, the elemental carbon to the total carbon (EC/TC) ratio was determined to be 1.3%, hollow structures were consistently observed using various oxidizers (O_2, CO_2, acetone and water) under mild oxidation conditions. For the black carbon particles generated by toluene pyrolysis at 1050^{o}C, the elemental carbon to the total carbon (EC/TC) ratio is about 21.3%, hollow structure was not observed.

Chapter 2: Oxidation Anisotropy and Size Dependent Reaction Kinetics of Zn Nanocrystals

2.1 Introduction

Zn is an attractive fuel and has been employed in powder form as a rocket propellant when mixed with sulfur [85]. Zinc is also used as the anode or fuel in the zinc-air fuel cell which forms the basis of the theorized zinc economy [86]. More recently Zn/ZnO redox reactions has been considered for thermo-chemical two-step water-splitting cycles for hydrogen generation [33, 42, 87]. The cycle involves a Zn hydrolysis reaction to produce hydrogen, followed by the solar reduction of zinc oxide. In a recent study [88], Zn nanoparticles have been employed so as to take advantage of their high surface to volume ratio and the ability to operate a continuous flow process.

As a wide-band-gap semiconductor, bulk ZnO has band gap energy of 3.37 eV at room temperature, and also exhibits piezoelectric properties. ZnO nanostructures such as nanowires/belts have attracted considerable attention due to their novel application in optical and electrical devices, sensors and medical devices [89-91]. While there exist many different techniques to prepare ZnO, the thermal-oxidation from Zn is the most basic and is widely employed to create a variety of ZnO nanostructures [92-96]. Despite

the widening application of Zn based nanostructures, very little attention has been paid to the quantitative kinetics of Zn nanocrystal (NC) oxidation.

The general theory of metal oxidation and related transport phenomena in oxide films have been developed and studied for several decades. The theory proposed by Wagner is restricted to thick films [97]. His theory is based on two assumptions: electrical neutrality within the film, and diffusion across the oxide film as the rate-liming step in the overall reaction. The theory leads to the parabolic growth law. However, the characteristic length (Debye-Huckel screening length) is on the order of several hundred nanometers to 1 μm [98-100]. So, given the size of our Zn NCs (less than 100nm) Wagner's theory does not apply. When the film thickness is less than 1μm, the assumption of electrical neutrality is invalid, and when the film thickness is less than 20nm, even the Nernst-Planck relationship is unreliable [98]. Compared with a thick film, the mechanism of thin film growth is not as well understood. There are a number of power laws that have been employed to describe the kinetics for the growth of thin films. The theory of Cabrera and Mott is useful when considering the growth mechanism of thin films [101]. In their theory, the thickening of the film is caused by the ionic transport across the film and the driving force is the electric field generated by electron transfer. However, the Cabrera and Mott theory contains parameters that can not be measured independently, which makes it particularly difficult to apply in any quantitative analysis. It is believed that metal oxidation is a diffusion-controlled process. In this paper, the classic diffusion controlled shrinking core model is applied in our study as a relatively straightforward way to extract reaction kinetics data of Zn NC oxidation.

An interesting phenomenon in solid crystal oxidation processes is that the oxidation rate is dependent on the crystal orientation. Some experiments have been conducted to investigate the crystal face dependence of the oxidation rate. For example Liu studied mm size single-crystal Ni surfaces using Auger electron spectroscopy (AES) and found the rate of oxygen uptake depended on crystal orientation $\{111\} > \{110\} > \{100\}$ [102]. They proposed that packing of the absorbed oxygen on $\{111\}$ surfaces is more compact and enhances the nucleation of bulk oxide. Munoz-Marquez [103] used medium energy ion scattering (MEIS) to study the oxidation on Ni(100) and Ni(111) surfaces and found that oxide film growth proceeds significantly faster on Ni(111) than on Ni(100). However, no comparable studies have been conducted on free (unsupported) nanometer single crystals.

In this paper we use electrical mobility classification and characterization to explore the size resolved reactivity of Zn NCs in free-flight, and determine quantitative Arrhenius reaction parameters. We will also observe that oxidation is anisotropic as imaged from electron-microscopic analysis. What distinguishes this study from previous studies, are first, free NCs are suspended in an inert gas environment, which means free of any potential substrate effects, and thus all crystal planes are co-existent and exposed to the same experiment conditions simultaneously. Secondly, NCs are nanometer in size, which means there are a larger portion of atoms on the edges. Those edges are sharp interfaces between the crystal planes. Thus, edge effect may play an important role in the NC oxidation process.

2.2 Experimental Approach

The basic strategy for studying the reactivity of Zn NC, is to size select NC's and then quantify their size resolved reactivity. The experiment system consists of three components. Preparation of monodisperse Zn NCs, exposure of size selected Zn NCs into a controlled temperature region, and finally, measurement of the mass change resulting from oxidation. A complete schematic of the experimental system with temperature and flow rate control is shown in Figure 2.1. Our experiment consists of two different ion-mobility schemes in series [104]. The first mobility characterization is to size select NCs with a differential mobility analyzer (DMA, home-made) [105-107]. The second mobility characterization employs an aerosol particle mass analyzer (APM, Model APM-3600, Kanomax Japan Inc.) [26] and measures changes in mass resulting from a controlled oxidation of the Zn NCs.

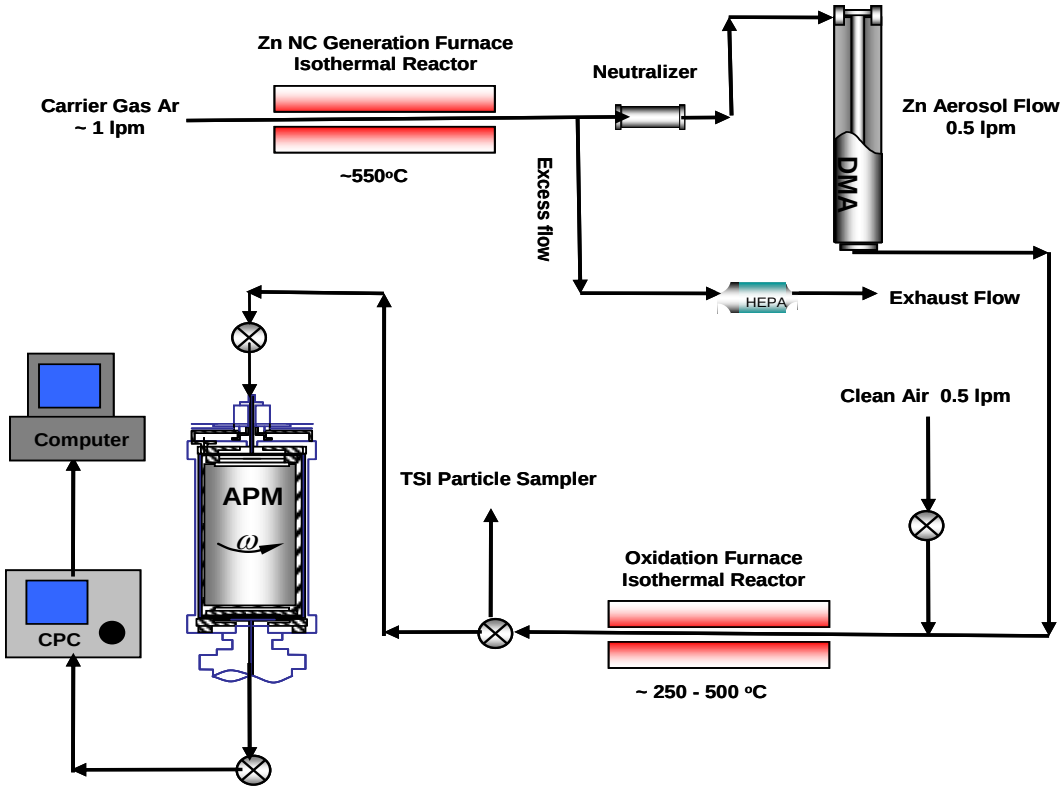

Figure 2.1 Experimental system for Zn, generation, size selection by DMA, oxidation and subsequent mass analysis with the APM

Since we are employing ion-mobility methods, particles are first charged to a Boltzmann charge distribution by exposing the nanoparticle aerosol to a Po-210 source, before the DMA. The average charge state of sample particles under Boltzmann distribution is quasi-neutral, with most of particles uncharged and equal amount of particles carry +/- 1 charge and +/-2 charges, etc. For example, in case of 50 nm particles, 60.2% particles will be neutral, 19.3% carry +/-1 charge, 0.6% carry +/- 2 charges, and higher charge state would be even less. Considering the small percentage in the multiple charged states, we ignore multiple charged particles. Both

the DMA and APM are configured to classify positively charge particles for these experiments.

2.2.1 In-situ Generation of Monodisperse Zn NCs

The Zn NCs are generated using an evaporation/condensation method in argon. Granular Zn (purity, ≥99.99% from Sigma-Aldrich) contained in a small ceramic boat was placed in a tube furnace at 550^{o}C to generate a flow of Zn vapor. The Zn vapor condenses as it exits the tube furnace, and by empirical adjustment of the tube furnace temperature, and the argon carrier gas flow rate we were able to form unagglomerated Zn NCs. Since our objective is to study size resolved reactivity we use a DMA as a band pass filter to generate monodisperse NCs. The DMA selects particles based on their electric mobility, which is related to the drag force and charge on a particle. For particles of the size being considered here the particles are being selected based on their projected surface area [105, 108, 109].

2.2.2 DMA-APM System

The DMA, used in this experiment for generating monodisperse NCs, consists of an annular region between two concentric cylinders, with the center cylinder held at high voltage and the outer one at ground. Charged particles of the right polarity feel an attractive force toward the center electrode, and move radically inward at a

constant electrophoretic velocity, determined by the particle charge, and drag force (which is a function of particle size). When charged particles flow between the cylinders the electric force on the particle is balanced by the drag force, and at a fixed voltage all particle exiting the instrument have (to the resolution of the instrument) equivalent mobility sizes. In the size range of consideration here, the DMA functions as a source of mono-area NCs.

The APM can determine the particle mass distribution based on particle mass to charge ratio, and is used in our experiment to monitor changes to the particle mass resulting from oxidation. The APM consists of two concentric cylindrical electrodes that rotate together at a controlled speed. An electric field is created by applying high voltage on the inner electrode, while the outer one is held at ground. Charged particles flowing within the concentric cylinders experience opposing centrifugal and electrostatic forces, and as a result, particles exiting the instrument (for fixed voltage and rotation speed) all have the same nominal mass. By scanning either the voltage or the rotation speed, the particle mass distribution (independent of particle shape) can be determined. APM mass measurements are independent of particle morphology because the centrifugal force is directly proportional to the mass. Our previous experiments have used the DMA-APM technique to measure the inherent density of nanoparticles, as well as to study the mechanism of aluminum and nickel oxidation [104, 110].

Based on operating conditions for the DMA and APM, we estimate uncertainties as follows. For the DMA the uncertainty is based on the theoretical transfer function which will give an uncertainly in the peak particle size of +/- 4 %. We then use a

Gaussian fit to determine the peak size which would have a precision uncertainty of no more than 1%. A similar result can be obtained for the APM however the uncertainties are not due to the transfer function but uncertainties in the step voltage which has a resolution of only +/-0.5V, which gives an uncertainty in mass of ~4%. Using the root-sum-square (RSS) method, we can estimate the uncertainty in density to be ~5%. This is consistent with our prior work using combined DMA/APM on reference aerosols (NaCl and DOP) which gave an experimentally determined uncertainly in density of 4%. Furthermore, our DMA/APM mass measurements of NIST SRM 60 and 100nm PSL spheres were within about 1.4% and 5.6%, respectively[111].

2.2.3 Zinc NC Characterization, Sampling, and Oxidation

In our experiment, Zn NCs of initial ion-mobility sizes of 50nm, 70nm and 100nm were selected in sequential experiments to study the size-dependent oxidation. After size classification, the Zn aerosol flow is mixed with air at the ratio of 1:1, and then passes through a second tubular reactor. This flow tube reactor enables the controlled oxidation of the Zn NCs for residence times of 2-4 sec's. The total flow rate of the aerosol flow is 1 LPM at standard condition. To monitor the small mass change of the NCs due to oxidation, an aerosol particle mass analyzer (APM) is placed downstream. Particles exiting the APM will be selected on the basis of mass, and are counted using standard particle counting methods using a condensation particle counter (CPC).

In the experiment, the temperature in the oxidation furnace was set between 250-500^{o}C in increments of 25^{o}C. The particle mass distribution was then measured for each reactor temperature after the system reached steady state. The room temperature particle mass distribution was also taken, and set as the base of the mass measurement. Samples for electron-microscopic analysis were collected exiting the evaporation furnace by electrostatically precipitating the aerosol onto a TEM grid.

2.3 Results and Discussion

2.3.1 Zn NC Morphology

Figure 2.2 shows the SEM image of two single Zn NCs that were deposited from the gas phase by electrostatic precipitation to a TEM grid. The NCs so obtained show a perfect hexagonal prism. Energy dispersive X-ray (EDS) spectra obtained from the NCs in SEM confirmed that the composition to be Zn. The crystal structure of zinc is hexagonal close-packed which belongs to the space group P63/mmc. Selected area electron diffraction analysis indicates that the Zn NCs have top surfaces of $\{0001\}$ crystal planes, and have side surfaces of $\{1\bar{1}00\}$ planes.

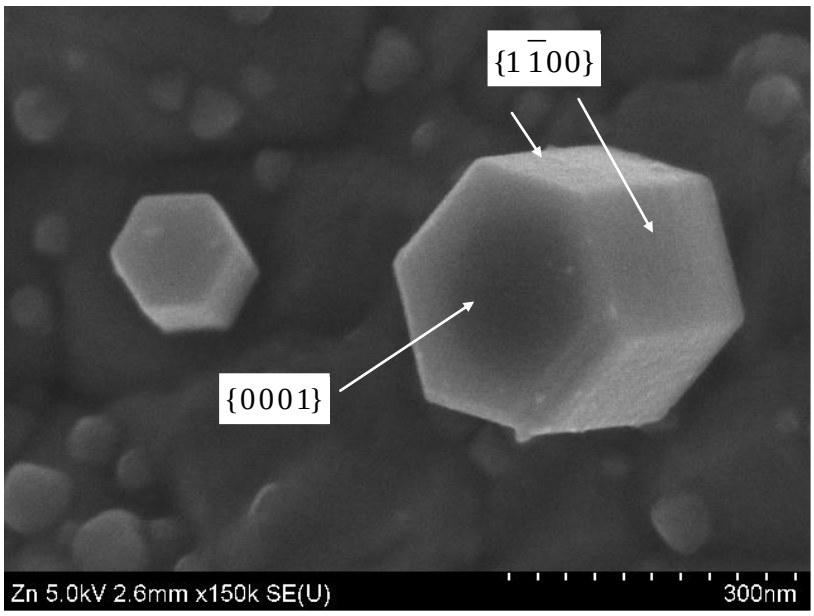

Figure 2.2 SEM image of the hexagonal-prism-shaped Zn NCs (before size selection)

2.3.2 Size-Dependent Reaction Rate

Figure 2.3 shows the normalized particle mass distributions for different initial sizes of Zn NCs oxidized in air at different temperatures, obtained from APM-CPC measurements. The particle number concentration is obtained as a 1 min time average of the CPC counts at each APM voltage. The peak mass of Zn NCs at each oxidation temperature is obtained by fitting the experimental data using a Gaussian distribution. The results in the figure show that the peak mass for each mobility size remains unchanged at low temperatures, and then increases in mass at elevated temperatures reflecting the increase rate of oxidation. Figure 2.4 shows the percentage conversion from Zn to ZnO as a function of reaction temperature for different sizes of NCs. As example, for 50nm Zn NCs, the oxidation starts at about 250^{o}C, and based on the

mass changes we find that the NC has fully oxidized by ~425^{o}C. Similar trends are observed for the other sizes of Zn NCs.

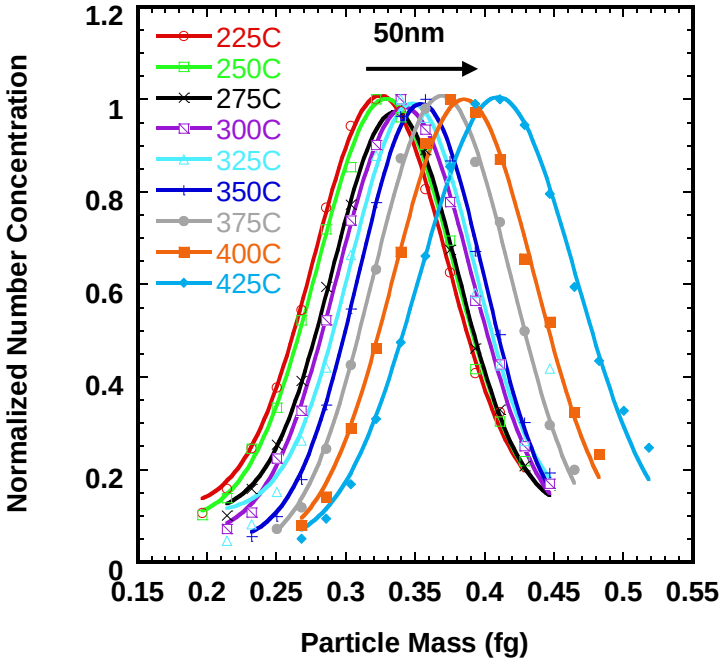

(a)

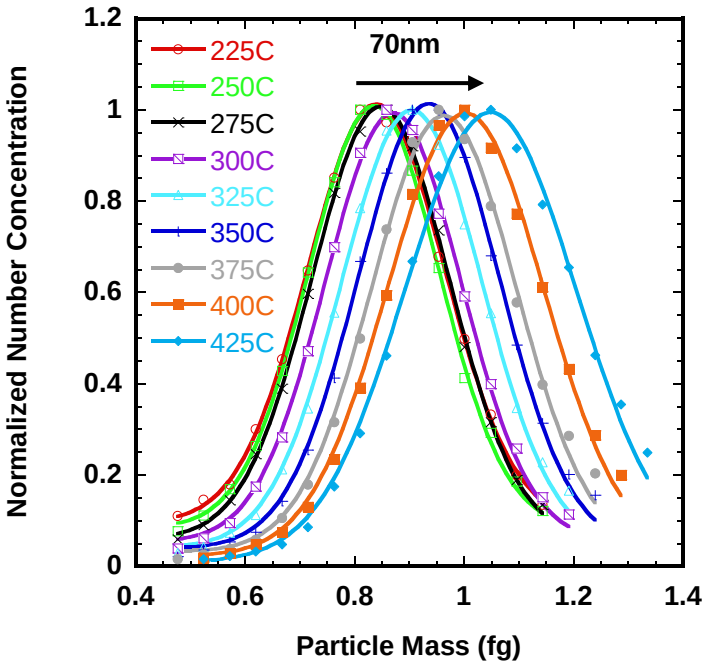

(b)

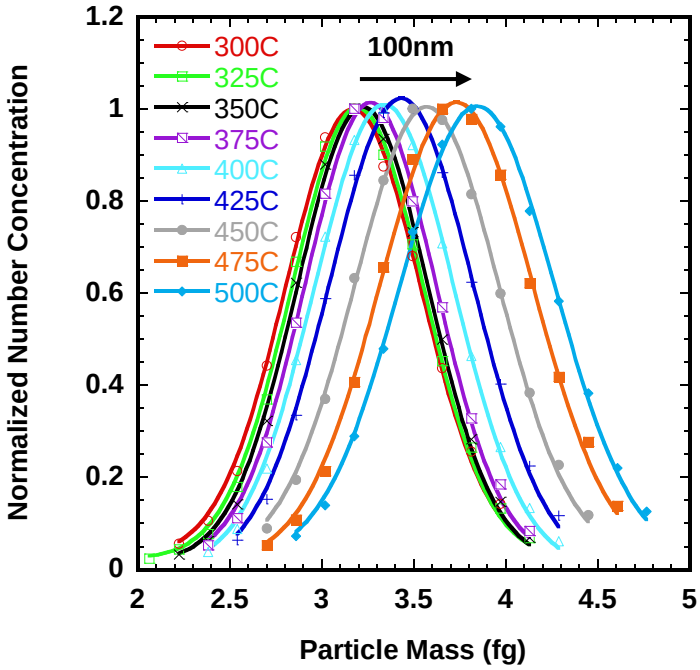

(c)

Figure 2.3 Normalized particle mass distributions for different mobility sizes of Zn NC at different oxidation temperatures (a) 50nm (b) 70nm (c) 100nm.

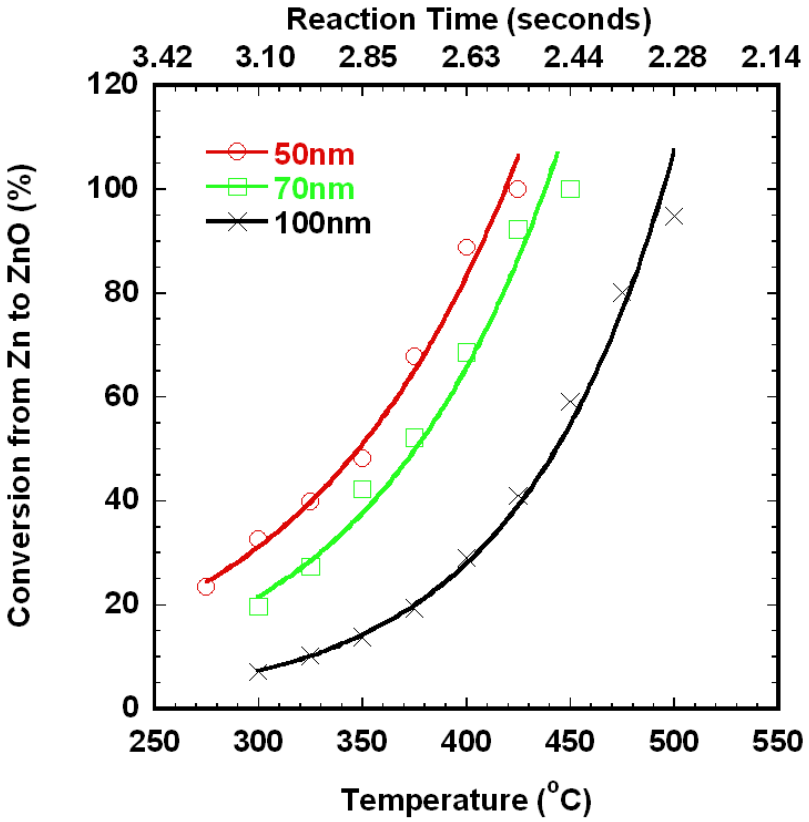

Figure 2.4 Percentage of conversion from Zn to ZnO for different sizes of Zn NCs

It is believed that metal oxidation is a diffusion controlled process. This suggests that the classic diffusion controlled shrinking core model could be applied in our study as a relatively straightforward way to extract reaction kinetics data [112]. The shrinking core model is typically described in three steps. 1: diffusion of gaseous reactant (oxygen) to the particle surface. 2: dissolution and diffusion of gaseous reactant (oxygen) through the oxide shell to the surface of unreacted core. 3: chemical reaction of the dissolved oxidizer with material (Zn) at the surface of the unreacted core. For spherical nanoparticles, Carter [113] applied the assumptions as in Wagner's theory to the shrinking core model, and derived an oxidation rate law for metal

particle oxidation. Following Carter's steady state analysis, the diffusion flux through the oxide shell can be related to the reaction rate as:

$$\frac{dN_{O_2}}{dt} = -4\pi D_e C_{O_2} \frac{r_c r_p}{r_p - r_c} \tag{1}$$

Where N_{O_2} is the mole of oxygen in the oxide layer, C_{O_2} is the oxygen molar concentration in the gas phase. r_c and r_p are the radius of the zinc core and the reacted particle radius, respectively. D_e, the diffusion coefficient for ion diffusion in the oxide layer is given by:

$$D_e = A \exp(-\frac{E_a}{RT}) \tag{2}$$

Where A is a size-dependent pre-exponential factor, E_a is the activation energy of the reaction, and R is the gas constant. Since the mass change of the reacted particle is due to the addition of gaseous reactant (oxygen) to the particle, if we multiply both sides of equation (1) by the relative molecular mass of oxygen, the mass change rate of the reacted particle can be immediately obtained by substituting D_e in equation (1) using equation (2):

$$\frac{dm}{dt} = 4\pi M_{O_2} C_{O_2} D_e \frac{r_c r_p}{r_p - r_c} \tag{3}$$

Where m is the absolute mass of the reacted particle and M_{O_2} is the molecular weight of oxygen. Knowing the furnace temperature, the particle mass change Δm can be obtained by integrating equation (3) as the particles pass through the furnace. Considering the exponential temperature dependence of the rate constant and the fact that r_c and r_p are more temperature dependent, we can approximate the instantaneous

mass changing rate by the average mass changing rate $\frac{\Delta m}{\tau}$, where τ is the reaction time in the furnace. Thus we can use the following equation to process our kinetic data:

$$\ln(\frac{\Delta m}{\tau}) = -E_a / RT + \ln(4\pi M_{O_2} C_{O_2} A \frac{r_c r_p}{r_p - r_c}) \quad (4)$$

The reaction time at different furnace temperatures can be calculated using the following equation:

$$\tau = \int_0^L \frac{1}{u(x)} dx \quad (5)$$

Where L is the length of the tube and $u(x)$ is the flow velocity, which can be calculated below as:

$$u(x) = \tfrac{4}{3} u_m \frac{T(x)}{T_0} \quad (6)$$

Where $4/3\ u_m$ is the peak flow velocity of carrier gas calculated from volume flow rate and the cross sectional area of the flow tube under the assumption of laminar flow at temperature T_0. $T(x)$ is temperature distribution within the tube at each furnace set point. Based on equation (4), the size-resolved activation energy can be obtained from an Arrhenius plot as shown in Figure 2.5. Two different regimes of oxidation are represented by the two linear fits, represent a slower reaction region at lower temperatures followed by a faster oxidation regime occurring at higher temperatures. The intersection of the two straight lines represents the transition temperatures between the two regimes. For the case of the slower reaction, the activation energy decreases from $46.1 kJ/mol$ for 100nm size NCs, to $34.0 kJ/mol$ for 50nm NCs. While for the faster reaction, the activation energy decreases from $63.1 kJ/mol$ for

100nm NCs to $49.3 kJ/mol$ for 50nm NCs. In general, the smaller particles have lower activation energy. We also conducted TGA experiments on a sample of commercial Zn nanoparticles. The sample with a mean particle diameter ~ 100nm showed and activation energy is $128.7 kJ/mol$, which is considerably higher than our experimental measurement and not unexpected. This difference between conventional methods and our approach has been consistently observed in previous works [114, 115]. It is well known that bulk methods suffer from heat and mass transfer effects, were milligrams of an aggregated sample are needed, while the sample mass of our aerosol based techniques is ~ 1 fg and is being performed on an isolated NC. Furthermore, for highly exothermic reactions, the reaction heat released will tend to exacerbate heat transfer problems, while the DMA-APM techniques employed here allows for a direct measure of mass change of individual particles and thus enables us to explore the intrinsic reactivity of NCs while minimizing the sampling error introduced by mass and heat transfer. Because of the complexity of the rate expression it is not easy to define a pre-exponential (A-Factor) in a simple Arrhenius form. Rather we can say that the effective oxygen sticking coefficient based on the oxygen flux and the mass change of the NC at different temperatures, ranges from 1.0E-7 to 1.0E-6.

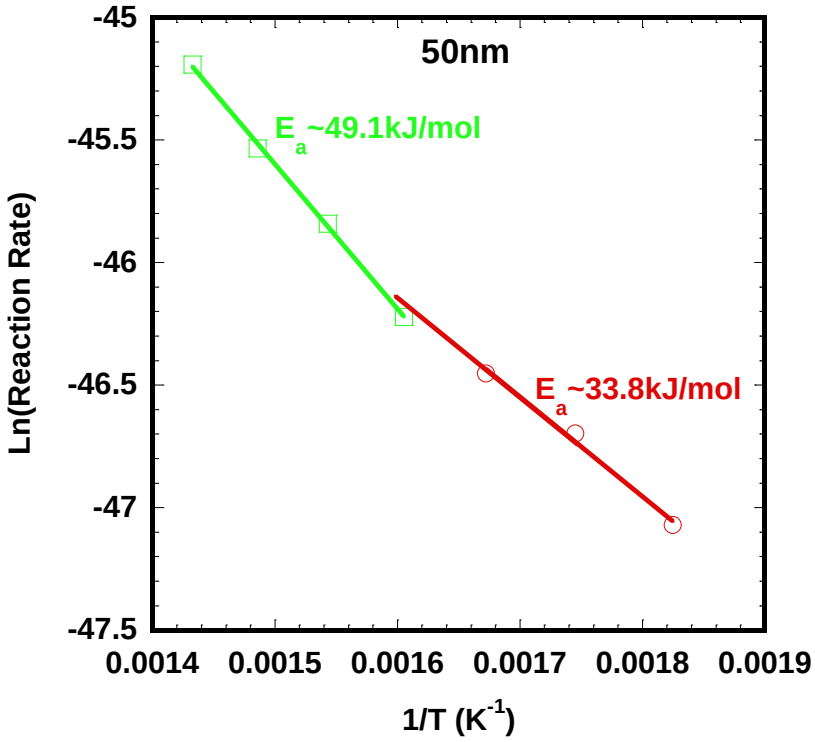
50nm
E a ~49.1kJ/mol
E a ~33.8kJ/mol
Ln(Reaction Rate)
1/T (K-1)
-45
-45.5
-46
-46.5
-47
-47.5
0.0014
0.0015
0.0016
0.0017
0.0018
0.0019

(a)

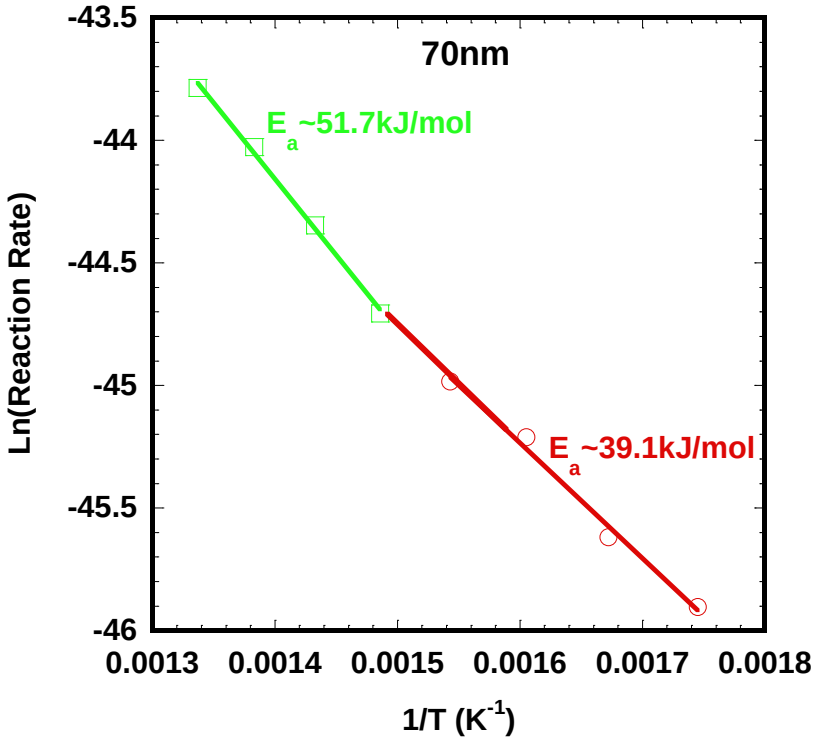
70nm
E a ~51.7kJ/mol
E a ~39.1kJ/mol
Ln(Reaction Rate)
1/T (K-1)
-43.5
-44
-44.5
-45
-45.5
-46
0.0013
0.0014
0.0015
0.0016
0.0017
0.0018

(b)

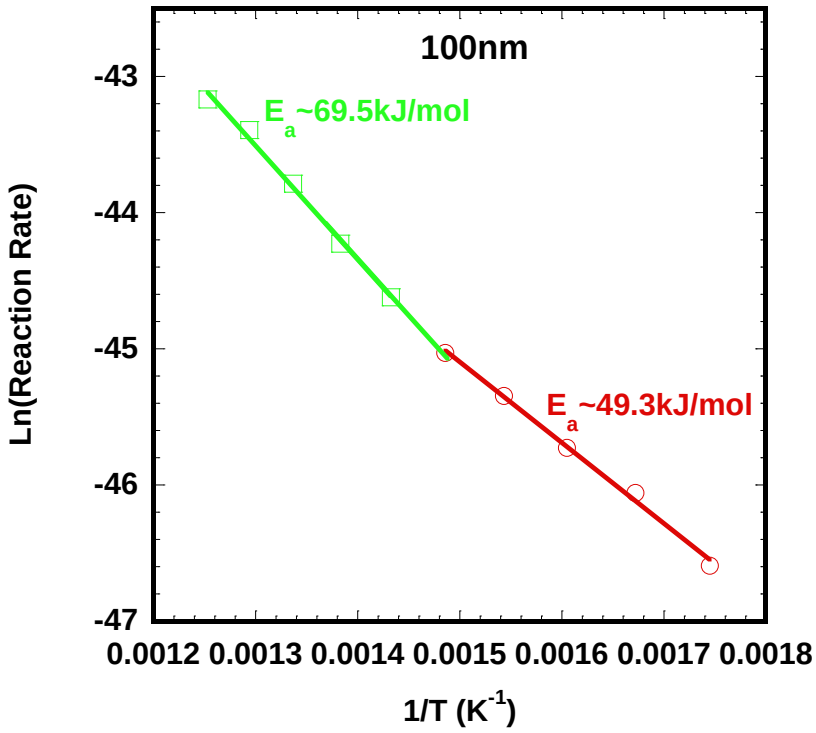

(c)

Figure 2.5 Arrhenius plot of reaction rate for different sizes of NCs (a) 50nm (b) 70nm (c) 100nm

Particle burn times for different sizes of NCs at different oxidation temperatures were also calculated based on the experimental reaction rate, and the NC mass measured by the APM. Figure 2.6 plots the particle burn time as a function of particle size for various temperatures. In this case the measurements are restricted to below the melting point. The particle burn time shows a size dependence close to $\sim D_p^2$, which is consistent with the oxide shell diffusion-controlled shrinking core model. However, the power of size dependence decreases slightly from 2.2 at 300°C to 1.6 at 400°C. This deviation may be partially explained by the slow and fast reactions for different sizes of NCs. For example, at temperature of 350°C, the oxidation of 50nm

NC is in the fast reaction regime while the 70nm and 100nm NCs are still in the slow reaction regime. Furthermore, this weaker size dependence (less than power two) has also been observed for Ni and Al oxidation [104, 110]. Based on molecular dynamics simulation [116] on oxide–coated nanoparticles the metal core is expected to have high internal pressures. A phenomenological model [110] developed for aluminum oxidation has shown that this higher internal pressure is at least partially responsible for a lower power dependence on particle size.

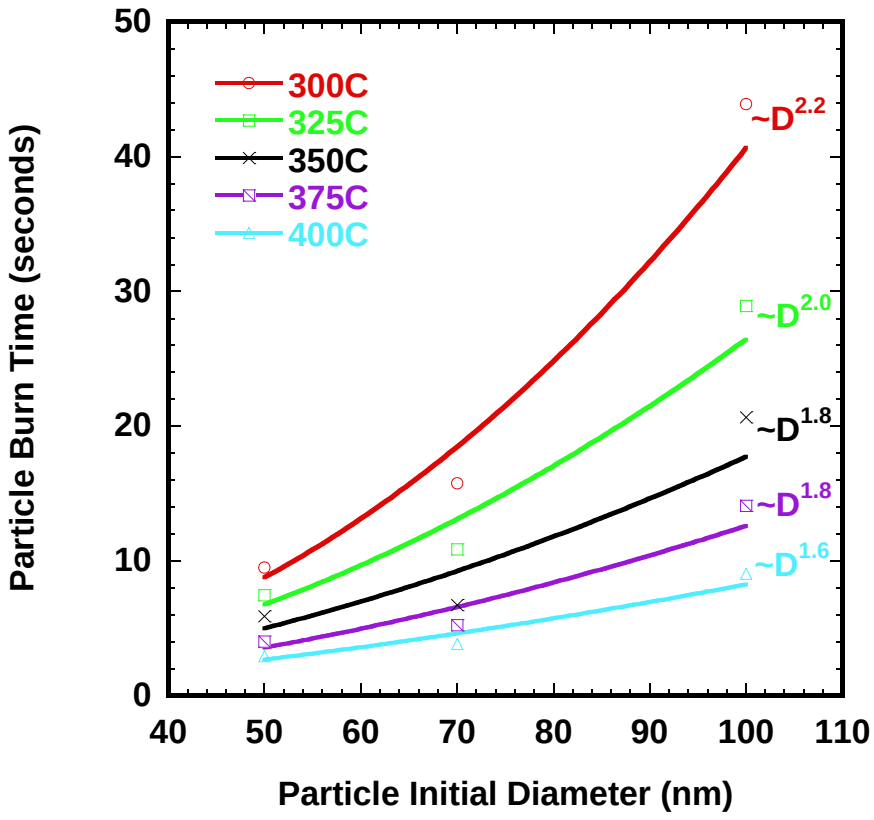

Figure 2.6 Particle burn time for different sizes of NC at different reaction temperatures

2.3.3 Zn NC Oxidation Anisotropy

To further explore the nature of the two oxidation regimes observed in the Arrhenius plots, samples of 100nm Zn NCs were collected for electron microscopic analysis after oxidation at 350°C, 400°C and 450°C, which are below, close to and above the transition temperature, respectively. The high resolution SEM images are shown in Figure 2.7.

As we can see from the figure, there is a preferable surface of oxidation during the initial stages. From the images collected at 350°C (2.7(a) and 2.7(b)), we see that there are band-shaped oxide layers formed around the six side surfaces of the NCs, while the top and bottom surfaces of NC are flat and remain unchanged. The Zn NCs show a strong oxidation anisotropy with the rate of oxidation on Zn $\{1\bar{1}00\}$ planes much faster than on the $\{0001\}$ planes. As the oxidation temperature increases to 400°C, the Zn NC undergoes restructuring with the edges between the top surfaces and side surfaces becoming blurred. The NC deforms and the original hexagonal-prism shape can not be distinguished. As oxidation temperatures well above the transition temperature (as shown in Arrhenius plots), the NC exhibits a flower-shaped morphology. Given the observed oxidation anisotropy we propose the following reaction mechanism: at the lower oxidation temperatures, only the side surfaces of the NCs are activated and oxide layer are formed first around those surfaces, while at higher oxidation temperatures, both the side and top surfaces are activated, which enhances the oxidation kinetics but requires a higher activation energy. This at least is consistent with the observed kinetic regimes.

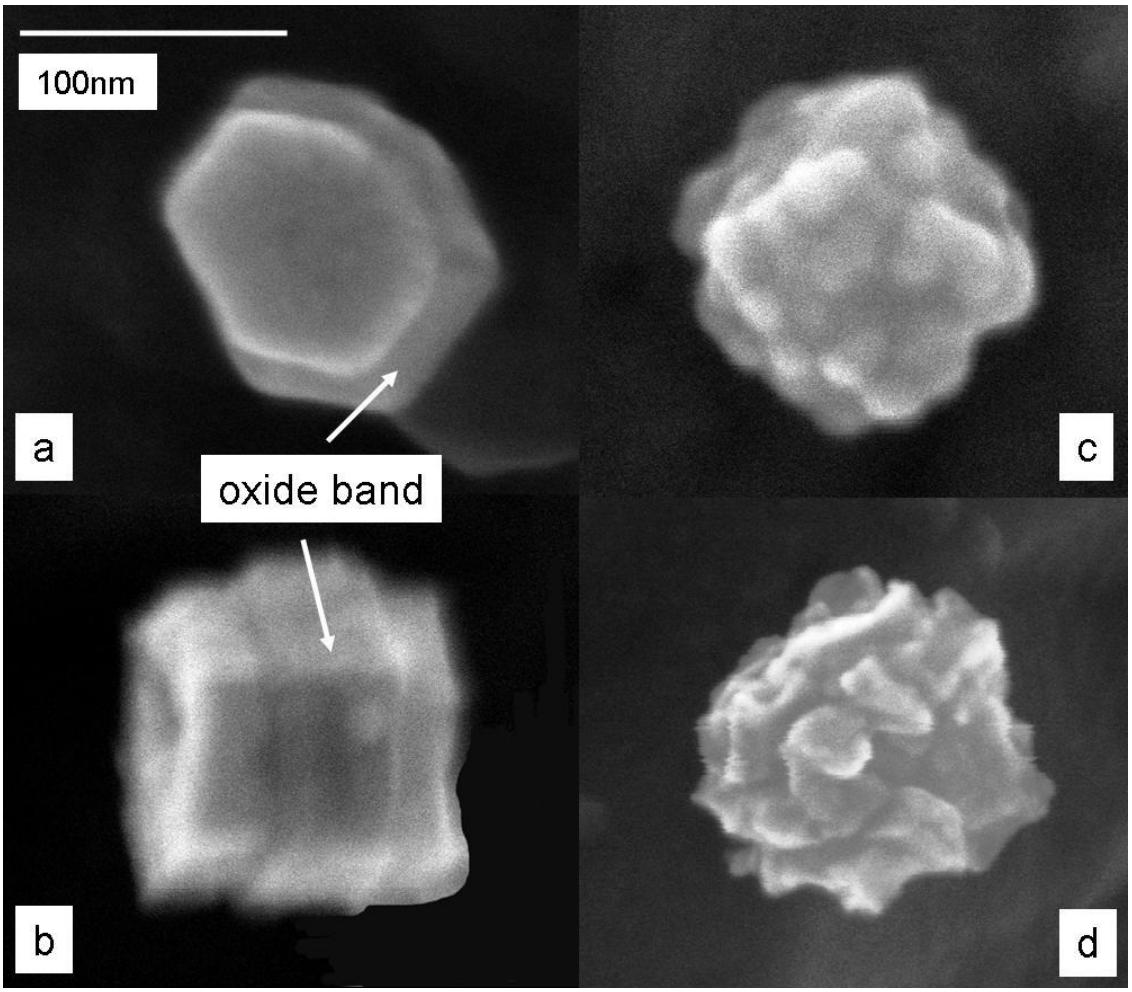

Figure 2.7 HR-SEM pictures of partially oxidized Zn NCs at different oxidation temperature (a) top view of the NC at 350^{o}C (b) side view of the NC at 350^{o}C (c) 400^{o}C (d) 450^{o}C

As discussed in the introduction, our NCs are free of any potential substrate effects, and there are a larger portion of atoms on the edges of our NCs. Those edges are sharp interfaces between the crystal planes. As such evaporation and oxidation are taking place simultaneously from all faces, and thus at the interface of these planes either a morphology change with time, or alternatively a change in reaction rate must

occur. No doubt these edge atoms are at a higher potential energy, due to their lower coordination number and high stain, thus potentially more reactive. This perhaps, is a more important distinction between millimeter size crystals and NCs. We have observed an analogous anisotropy effect during the evaporation of Zn NCs in an inert atmosphere, which is the subject of another study. Briefly however, what we observed can be summarized in Figure 2.8 which shows a SEM picture of a partially evaporated 100nm Zn NC. Most of the hexagonal-shaped top surfaces (Zn $\{0001\}$ planes) of the Zn NCs during evaporation are well-preserved relative to the side surfaces (Zn $\{1\bar{1}00\}$ planes). Material from the side surfaces are preferentially etched away, which leaves the side surfaces with a depression while the top surfaces remain perfectly planar. Note that in both evaporation and oxidation it is the $\{1\bar{1}00\}$ that reacts preferentially. Furthermore the reactivity is not homogeneous across the face, but is most active away from the interface with the {0001} surface. The behavior is consistent with the interface of the {0001} surface acting as a pinning site. The evolving morphology is then a competition between the thermodynamic stability between the two planes and the reaction process.

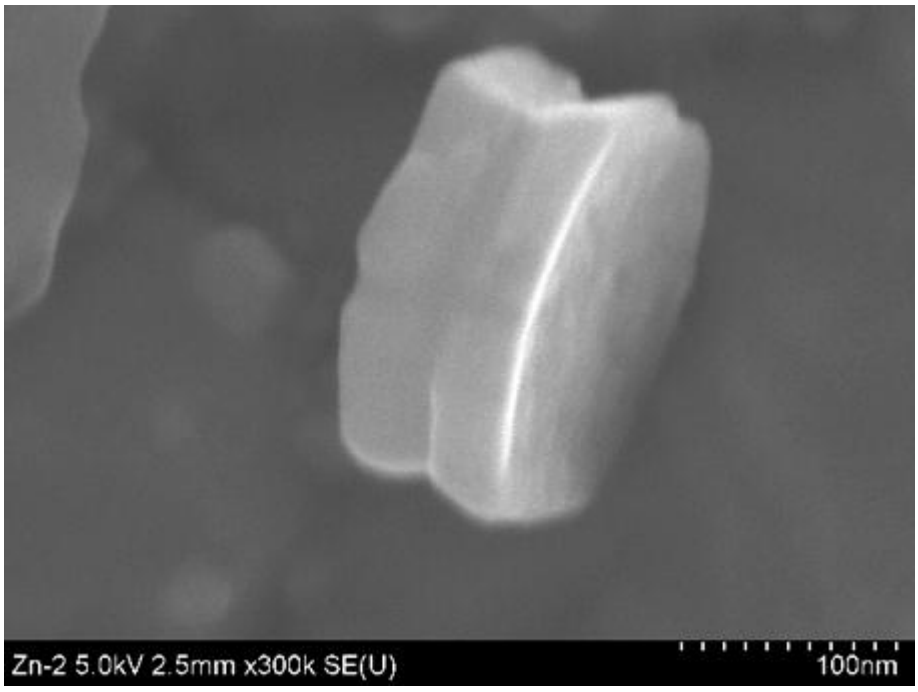

Figure 2.8 SEM image of a partially evaporated 100nm Zn NC

Law [117] highlights this edge-enhanced oxidation effect in his ZnO nanowire growth mechanism. Furthermore, the side surfaces are Zn $\{1\bar{1}00\}$ planes which have higher surface energy than the top surfaces (Zn $\{0001\}$ planes). It is known that high energy surfaces tend to have an enhanced oxidation rate than low energy surfaces which are more stable [118].

This oxidation anisotropy of NCs could in principle be applied to increase the reactivity of nano energetic materials or materials for solar thermal hydrogen generation for example by elongation of the c-axis of NC, to maximize the high energy surface area.

2.4 Conclusions

Size-classified substrate-free Zn NCs are explored for their oxidation kinetics using an in-flight tandem ion-mobility DMA-APM method. This method allows for a direct measure of mass change of individual particles and thus enables us to explore the intrinsic reactivity of NCs while minimizing the sampling error introduced by mass and heat transfer occurring in traditional methods. Two reaction regimes were observed for Zn NC oxidation, a slower reaction regime at lower temperatures followed by a faster oxidation regime occurring at higher temperatures. A shrinking core model is used to extract the size-dependent oxidation activation energies. Using electron microscopic analysis, we observed a strong effect of oxidation anisotropy. An oxidation mechanism based on surface energy anisotropy and edge-enhanced oxidation effects was proposed to explain the observed oxidation behavior of Zn NCs.

Chapter 3: Evaporation Anisotropy of Free Zn Nanocrystals

3.1 Introduction

Phase transitions of nanocrystal/nanoparticles are of great interest because of their size dependent properties. Examples include melting point depression [13-15] (one of the oldest areas of small particle research) and size-dependent evaporation [19, 119]. Furthermore morphology changes are often accompanied with phase transitions [16, 18, 120].

The prospect of exploiting these properties to create new functional materials and advanced devices has become the primary motivation for this multidisciplinary research area. For example, in the area of catalysis, accurate measurement of the transition temperature as a function of particle size helps determine the thermal stability regime of different sizes of catalytic particles, whereas the ability to control the shape of NCs can change their catalytic ability [23, 121].

As the crystal becomes smaller, there is a higher proportion of atoms on the surface with fewer nearest neighbors, and are thus more weakly bound and less constrained in their thermal motion than the bulk. Furthermore, atoms on different types of crystal faces have different bonding, surface atom densities and electronic structure and thus their properties are expected to be different. Previous experiments have shown that the physical processes, such as surface melting is crystal face dependent[17] and that chemical reaction rates are anisotropic [102, 103, 122].

In this study, we use an on-line tandem gas-phase ion-mobility NC characterization method, together with off-line electron microscopy to study the evaporation from Zn NCs. The size dependent evaporation temperature is determined by ion-mobility measurements, whereas the NC shape transformation is observed by electron microscopic analysis.

3.2 Experiment

The details of the experiment system have been described in Chapter 2 and in reference 14. In brief, the experiment system consists of four parts: (a) Generation of Zn NCs, by evaporation-condensation (b) Size selection to generate monodisperse Zn NC in the aerosol phase using a differential mobility analyzer (DMA) [105-107]. (c) Heating of Zn NCs in a temperature-controlled tube furnace, and (d), measurement of the mass change resulting from evaporation using an aerosol particle mass analyzer (APM) [26]. Previous studies [19, 119] have investigated evaporation from aerosols used a tandem DMA technique to monitor the size change of spherical particles. However, the interpretation of ion-mobility data is based on assuming the particles are spherical and can lead to considerable errors particularly for the case investigated in this study. In this study we combine the DMA with an APM which gives a direct measure of particle mass regardless of shape. Our DMA-APM mass measurements of NIST SRM® 60 and 100 PSL spheres were within about 1.4% and 5.6%, respectively [123]. We have employed the DMA-APM technique previously to study the oxidation kinetics of nickel nanoparticles[104] and Zn NCs [122].

Zn NCs are generated by evaporating granular Zn (purity, ≥99.99%, Sigma-Aldrich) at 550^0C with a tube furnace, in a carrier gas of argon at 1 LPM (liter per minute). Unagglomerated single crystal Zn NCs are formed at the exit of the flow tube by empirical adjustment of the furnace temperature, and the argon carrier gas flow rate. In our experiment, Zn NCs of ion-mobility sizes of 50nm, 70nm, 100nm and 150nm were selected using the DMA as a band-pass filter in sequential experiments to study the size-dependent evaporation. After size classification, the aerosol is passed through a second tube furnace which allows controlled evaporation of the size selected NCs. The residence time of the aerosol in this furnace is about 5 seconds at an argon flow of 0.5 LPM. The changes in NC masses are monitored by the APM downstream. The temperature in the evaporation furnace was set between 250 - $400^\circ C$ in increments of $25^\circ C$. The particle mass distribution was then measured for each furnace temperature after the system reached steady state. The room temperature particle mass distribution was also taken, and set as the base of the mass measurements. Samples for electron microscopy analysis were collected downstream of the evaporation furnace by electrostatically precipitating the aerosol onto a TEM grid.

3.3 Results and Discussion

3.3.1 Evaporation Anisotropy of Zn NCs

Figure 3.1(a) shows SEM images of two single Zn NCs which exhibit a perfect hexagonal prism. EDS (energy dispersive X-ray spectroscopy) spectra obtained from the NCs in the SEM confirmed the composition as Zn. Selected area electron diffraction analysis indicated that the Zn NCs have top surfaces of $\{0001\}$ and side surfaces of $\{1\bar{1}00\}$ crystal planes.

Figure 3.1(b) and 3.1(c) show SEM and TEM images of a partially evaporated 100nm mobility size Zn NC collected after controlled evaporation at 375^{o}C for ~5 seconds. As we can see from the images, most of the hexagonal-shaped top surfaces (Zn $\{0001\}$ planes) of the Zn NCs are well-preserved relative to the side surfaces (Zn $\{1\bar{1}00\}$ planes) during evaporation. Material from the side surfaces and edges are preferentially etched away, which leaves the side surfaces with a depression while the top surfaces remain perfectly planar. Measurement shows the width of the side surfaces do not change. The reader is reminded that the evaporation takes place in the gas phase prior to deposition of the NC on the TEM grid.

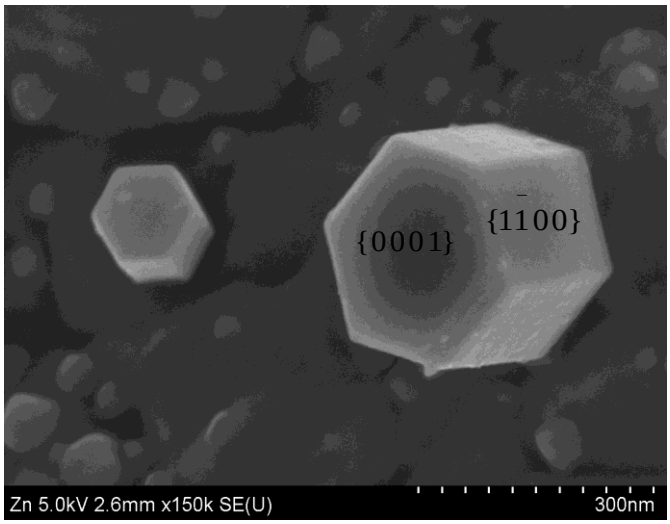

(a)

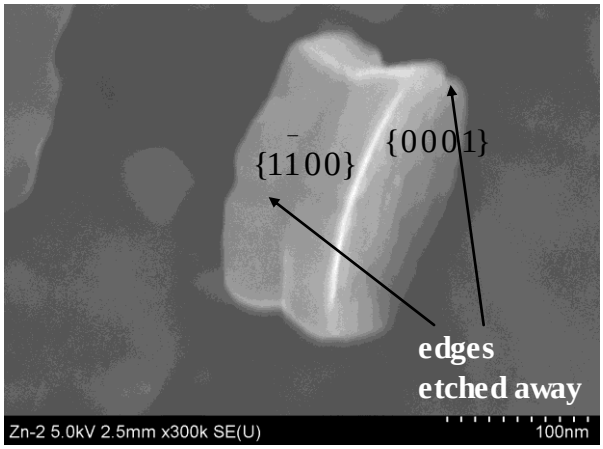

(b)

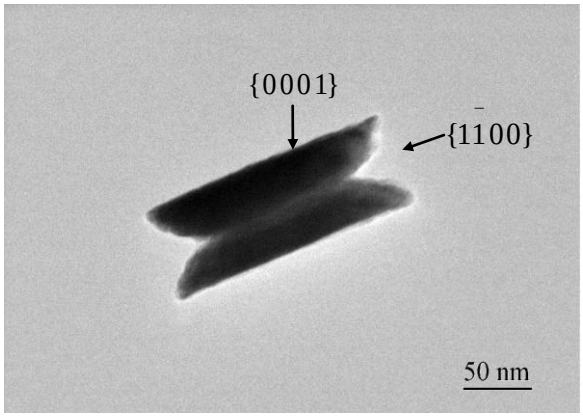

(c)

Figure 3.1 Images of aerosol grown hexagonal-prism-shaped Zn NCs (a) SEM image of Zn NCs before size selection (b) SEM image partially evaporated Zn NC (c) TEM image of partially evaporated Zn NC (The crystal planes marked in the image may change during the evaporation, especially, the original $\{1\bar{1}00\}$ *planes may no longer exist.)*

To explain the observed evaporation anisotropy, we propose an evaporation mechanism based on the theory of surface melting. As Zn NCs enter the furnace

region, the NCs are heated to the furnace temperature which leads to premelting [1] of some of the NC surfaces and edges. A thin layer of Zn quasi-liquid [2] forms preferentially on the side surfaces ($\{0001\}$ planes) of Zn NCs and on edges rather than on the top surfaces ($\{1\bar{1}00\}$ planes) due to the crystal-face dependent surface melting [17]. At 375°C, the energetic criterion of surface melting is met for Zn $\{1\bar{1}00\}$ planes but not for Zn $\{0001\}$ planes. The quasi-liquid layer over the side surfaces greatly enhances the evaporation rate so that a depression is formed. We have observed an analogous anisotropy effect during the oxidation of free Zn NCs [122]. In both evaporation and oxidation it is the $\{1\bar{1}00\}$ plane that reacts preferentially. Furthermore the reactivity and the evaporation rate are not homogeneous across the face, but are most active away from the interface with the {0001} surface. The behavior is consistent with the interface of the {0001} surface acting as a pinning site.

To compare the effect of different time-temperature heating history on the morphology of NCs, an in-situ TEM heating experiment was also conducted on Zn NCs. The experiment was carried out in a JEOL JEM 2100 LaB_6 TEM. The sample was heated from room temperature up to 325°C. Figure 3.2 shows the TEM images of a side surface deposited Zn NC before and after heating treatment. As we can see from the images, after heating in the TEM at 325°C for about 6 minutes, the side surface of NC transforms from rectangular shape to a spherical shape. The similar shape transformation has also been observed by Wang for platinum NCs where he

[1] Premelting describes the fact that, even below its melting point, quasi-liquid films can be observed on crystalline surfaces124. Dash, J. G.; Rempel, A. W.; Wettlaufer, J. S., The physics of premelted ice and its geophysical consequences. *Reviews of Modern Physics* **2006,** 78, (3), 695-741..

[2] The quasi-liquid has properties intermediate between those of the solid and the bulk liquid125. J.F.van der Veen, B. P., A.W.Denier van der Gon, Surface Melting. In *Chemistry and Physics of Solid Surfaces*, R.Vanselow, R. H., Ed. Springer: 1988; Vol. VII, pp 455-490.

attributes the NC shape transformation to the surface premelting. To protect the TEM vacuum column, we were unable to go to higher temperatures for these Zn studies, however, homogenous evaporation from the surfaces of the spherical NC is expected if we further increase the temperature beyond 325^{o}C.

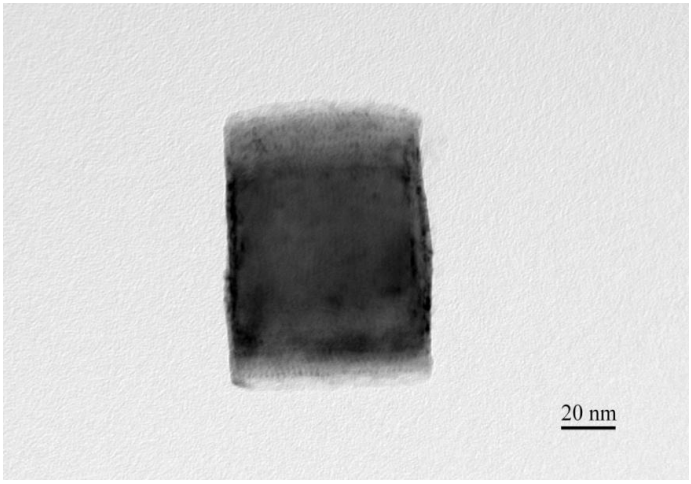

(a)

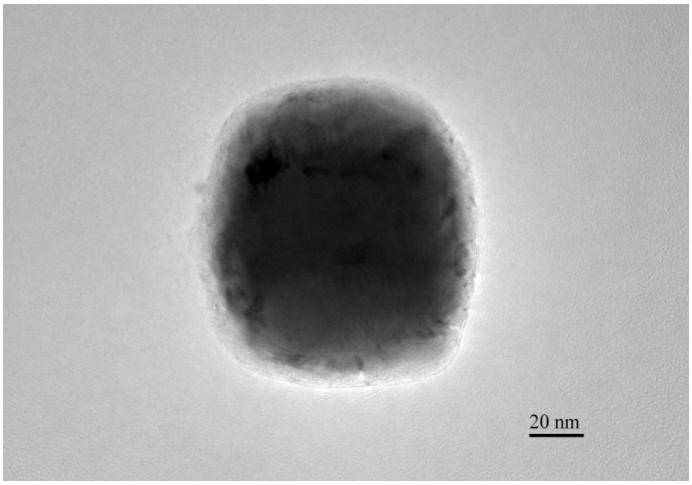

(b)

Figure 3.2 (a) Image of a side surface deposited NC before heating in a hot-stage TEM (b) after heating in the TEM at 325^{o}C for 6 minutes, the NC transforms into a spherical shape

Two different shape changes are observed for NCs heating in a tube furnace and in a hot-stage TEM. What distinguishes the two approaches is that free NCs are suspended in an inert gas environment, which means free of any potential substrate effects, and thus, all crystal planes are coexistent and exposed to the same experimental conditions simultaneously. Second, free NCs were heated to the furnace temperature in about 1s, and then evaporated in the tube furnace for only seconds, whereas in the hot-stage TEM, NCs were heated to a lower temperature and remained at that temperature for several minutes. At high temperature, the evaporation rate is so large that materials evaporate as soon as they melt. At lower temperatures, molten Zn diffuses over the whole NC surface leading to the more energy favorable spherical shape. This surface diffusion induced morphology evolution takes place over several minutes.

The evolution of the morphology observed in Figure 1 and 2 suggest that fast evaporation could be a feasible technique to produce particles with unique shapes by trapping them in meta-stable configurations which could potentially be of benefit in for example catalysis.

3.3.2 Size-Dependent Evaporation Temperature of Zn NCs

To study the size dependent evaporation behavior of Zn NCs, the mass changes of size selected NCs are monitored at different temperatures. A typical plot of normalized mass distributions of Zn NCs at different evaporation temperature is

shown in the Figure 3.3(a). As we can see from the plot, at low temperatures the particle mass distributions overlap with each other, i.e. evaporation is not occurring. As we further increase the furnace temperature, the Zn NC mass distribution decreases (to the uncertainty of the instrument) from the room temperature mass distribution, which indicates evaporation of Zn NCs. For each temperature, the peak mass of the NC mass distribution is calculated by fitting the experiment data using a Gaussian distribution and serves as the representing mass of the monodispersed Zn NC population. Figure 3.3(b) shows the plot of NC mass vs. temperature. The plot can be categorized as falling into two regions, which can be represented by the best linear fits to the data. The near horizontal line represents the un-evaporated case, in which the mass of the NCs doesn't change, while the steeply sloped straight line represents an evaporation case. The onset temperature for evaporation for each mobility size is determined by finding the intersection of the two straight lines. From the experiment, even for the largest size of NCs $(150nm)$, the onset temperature of evaporation is lower than the bulk melting temperature of Zn $(692K)$ and the bulk boiling temperature $(1180K)$. This result is consistent with the experimental observation of PbS and Ag nanoparticles [19, 119].

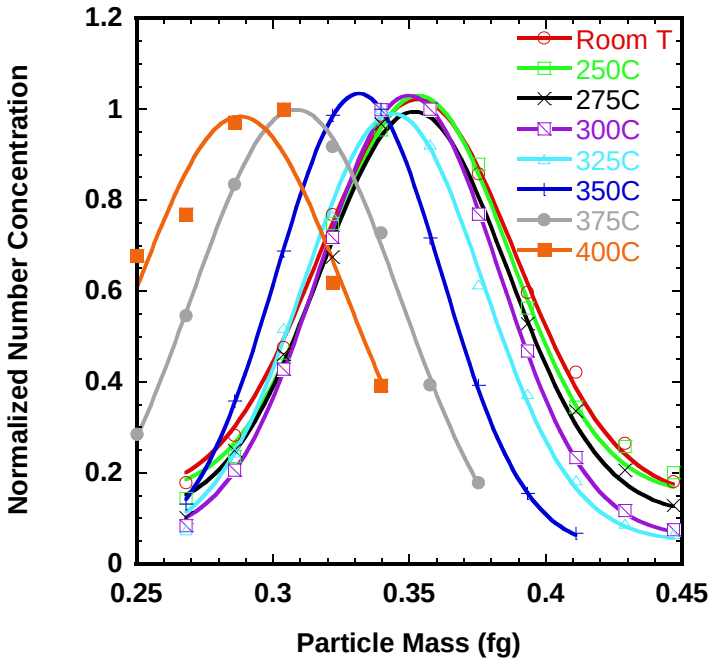

(a)

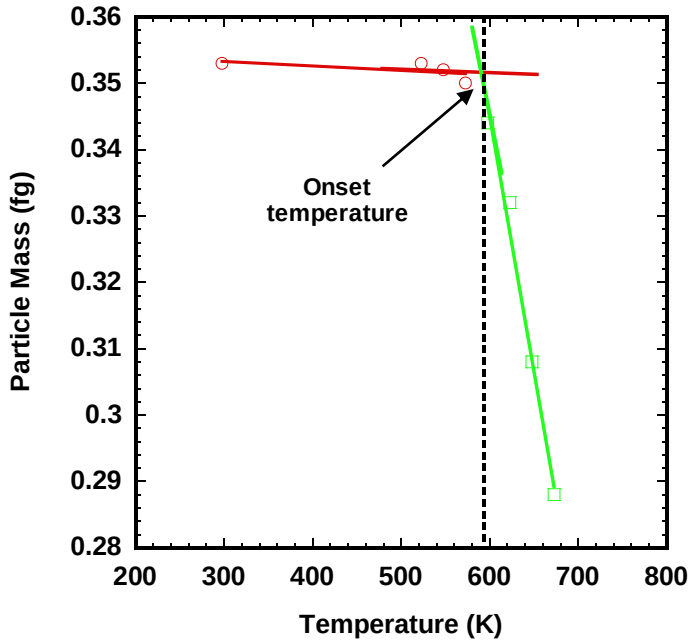

(b)

Figure 3.3 (a) Normalized particle mass distributions for initial mobility NC size of 50nm at different evaporation temperatures. (b) Particle mass vs. temperature for

initial NC size of 50nm. The intersection of two straight lines is the onset temperature of evaporation.

Since material evaporates only from the side surfaces of the NCs and the fact that NCs are hexagonal prism in shape, we choose the length r measured from the center of the NC normal to the side surfaces to be the characteristic radius of the Zn NCs. Based on the room temperature mass measurement and the geometry of the synthesized NC, we obtain the characteristic diameter of our Zn NCs to be 39.6, 55.4, 80.0 and 113.6 nm corresponding to NCs of initial mobility diameters 50, 70, 100 and 150 nm, respectively. The onset temperature of evaporation is plotted against the inverse of the characteristic diameter of the NC as shown in Figure 3.4. A linear relationship is obtained by fitting the experimental data. From the plot, we can see that the onset temperature of evaporation indeed decreases with the NC size. The best fit line yields a slope of $-2000 \pm 80 nm \cdot K$ and an intercept of $654 \pm 3K$, the latter represents the temperature at which very large particles start to evaporate.

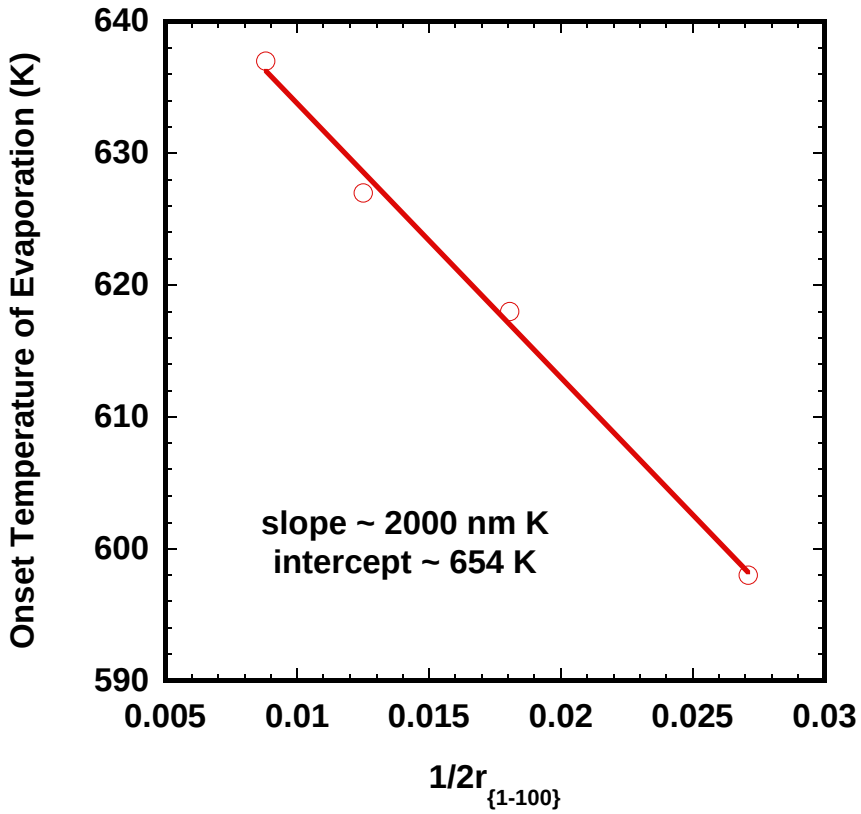

Figure 3.4 Onset temperature of evaporation vs. $1/2r_{\{1\bar{1}00\}}$

The cohesive energy of a solid (E_B) is an important physical quantity to account for the binding strength of the crystal and is equal to the energy dividing the crystal into the individually isolated atoms by breaking all the bonds of the solid [126]. The cohesive energy is considered as one of the most fundamental thermal properties that describes the inner structural energy of nanoparticles and shows how strongly atoms hold together. It is regarded as being directly related to the nature of the thermal stability of the nanoparticle. Based on the studies by Nanda [127] and Wang [128], the evaporation temperature can be scaled with the size-dependent atomic cohesive energy as follows:

$$\frac{T_{ev}(D)}{T_{ev}(\infty)} = \frac{E_B(D)}{E_B(\infty)} \tag{4}$$

Where $T_{ev}(D)$ is the evaporation temperature for particles of size D while $T_{ev}(\infty)$ represents the bulk evaporation temperature. Wang [128] simplified the functional form of $\frac{E_B(D)}{E_B(\infty)}$ and obtained a size-dependence evaporation temperature relation similar to that of the size-dependence of melting temperature:

$$T_{ev}(D) = T_{ev}(\infty) - \frac{hE_B(\infty)}{3RD} \tag{5}$$

where *h* is the atomic diameter and *R* is the gas constant. Substitution of the slope of $-2000nm \cdot K$ from the experiment and $h = 0.29nm$ [129] for Zn yields the bulk cohesive energy $E_B(\infty)$ to be $1.8 \pm 0.1ev$. The experiment value for Zn cohesive energy is *1.35ev* [129]. Various theoretical methods [130-133] have been employed to calculate the cohesive energy of bulk Zn. However, there is relative wide range of calculated values from 0.97ev up to 1.91ev due to complexity in electronic correlation. Compared with the available Zn cohesive energy data, our experimental value is higher than the reported experiment value but is in reasonable agreement with the theoretical predictions.

3.4 Conclusion

In summary, we have successfully generated size-classified Zn NCs and have demonstrated that the size-dependent evaporation of free Zn NCs can be studied by an in-flight tandem DMA-APM method. The variation of the onset temperature of

evaporation with the size of NCs is found to be similar to the melting temperature depression of small nanoparticles. It is found that the onset temperature decreases as the NC size decreases and is analogous to the Kelvin effect. The cohesive energy of bulk Zn is determined to be $1.8 \pm 0.1 ev$ from the size dependent evaporation data. We also observed the evaporation anisotropy effect in the evaporation process of NCs using electron microscopy. A mechanism based on crystal face dependent surface melting is proposed to explain the evaporation anisotropy effect.

Chapter 4: Size-Resolved Kinetics of Zn Nanocrystal Hydrolysis Reaction for Hydrogen Production

4.1 Introduction

Water-splitting thermochemical cycles have been demonstrated to bypass the H_2/O_2 separation problem which impedes single-step thermal dissociation of water, and further allows operation at relatively moderate upper temperatures [33]. Abraham [134] investigated the potential for water-splitting cycles based on general thermodynamic principles and concluded that the minimum number of reaction steps operating between 1000K and 298K is three. Previous studies were mostly focused on multistep thermochemical cycles using nuclear heat and were forced to operate under the temperature limit of about 1200K due to the maximum temperature of the heat source [34]. However, these multiple steps (more than two) suffer from inherent inefficiencies associated with heat transfer and product separation at each step [33]. Two-step water-splitting cycles based on metal oxide redox pairs are thermodynamically more efficient and can been achieved using concentrated solar energy. These type of cycles were first proposed by Nakamura [36] based on Fe_3O_4/FeO redox pair. In the first step of the cycle, solar energy is used to dissociate the metal oxide to metal or lower valence metal oxide. In the second step, metal is oxidized by water at moderate temperatures to form hydrogen and the corresponding metal oxide.

Among the feasible two-step water-splitting thermochemical cycles, the ZnO/Zn redox pair has attracted particular interest for its potential of achieving high energy conversion efficiency [42]. The theoretical upper limit is 44% with complete heat recovery. Several studies have been conducted on different aspects of the thermal dissociation of ZnO, and experimental solar furnace/reactors have been built for exploratory tests [44-46, 135-139]. Our special interest in this paper focuses on the 2nd step of the ZnO/Zn cycle, the Zn hydrolysis reaction. The reaction is thermodynamically favorable below about 1400K but with kinetic constraints [43]. The Zn hydrolysis reaction has been studied on various forms of Zn material such as Zn discs [140], liquid zinc [135, 141], Zn vapor [87, 142], Zn powder/nanoparticles [43, 88, 143, 144] and on solar zinc [145, 146]. Various analytic tools have been employed to probe the reaction kinetics and characterize the reaction products. For example, GC/MS has been used for hydrogen measurement, thermogravimetric analysis for monitoring reactant weight and X-ray, TEM and DMA for Zn/ZnO particle characterization. The reaction rate has been studied on Zn discs by Bazan et. al. [140] at 21 to 50 ℃, on liquid Zn by Bermann and Epstein [141] in the temperature range of 450-500 ℃ and on zinc powder by Funke et.al [147]. Clarke and Fray investigated the Zn hydrolysis reaction by analyzing the wall deposit in an aerosol reactor at a temperature up to 900 ℃. The detailed experimental conditions and results from previous studies are summarized in table 4.1.

Table 4.1 Summary of recent studies on Zn hydrolysis reaction

Zn Material	Temperature	Experimental Tools	Reaction Kinetics	Hydrogen Conversion
Author				
solar Zn	748-803K	catharometric analyzer	activation energy	maximum H_2 yield

Chambon nanoparticle (2009) with void fraction of 91 ± 1%		environmental SEM	of 87 ± 7kJ/mol, and reaction order of 3.5 ± 0.5	~ 55%
submicron Zn particles, (2009) d_{BET} =164 ± 10 nm	330–360°C	thermogravimetric balance, TEM, XRD, GC	an initially linear conversion profile followed by a parabolic conversion profile independent of water mole fraction	maximum ZnO content ~ 95%, at 350°C with reaction time ~ 180min and water mole fraction of 0.4
Zn particles Funke (average size (2008) 158nm)	653-813K	thermogravimetric analysis, TEM,SEM, EDS, combustion oxygen Analyzer	activation energy of 132 ± 27kJ/mol	maximum 24% at 813K with residence time of 0.6s
in-situ formation Hamed and hydrolysis (2008) of Zn aerosol	1023K and 1073K	GC, X-ray, TEM, DMA	Zn vapor deposition followed by hetero-geneous reaction on the wall	87%-96% at residence time 1.71 and 2.12min

solar Zn Vishnevetsky (2007)	458-833K	hydrogen analyzer, X-ray, TEM	two stages observed, reactivity is higher for solar Zn powder than for commercial Zn	24%-81% for temperature range 458-833K
in-situ formation Ernst and hydrolysis (2006) of Zn aerosol	573-1273K	thermogravimetic analysis, GC, TEM	H_2 formation is favored by heterogeneous reaction, higher reaction temperature.	up to 90% H_2 conversion at $T_R > 900K$
in-situ formation Weiss and hydrolysis (2005) of Zn aerosol	923, 1023 and 1073K	GC, X-ray, TEM	conversion reaches optimum at 1023K, ZnO passivating layer on larger particles is the reaction barrier	37% to 72% at 923 and 1023K and decrease to 37% at 1073K
in-situ formation Wegner and hydrolysis of (2005) Zn nanoparticles	1023K and 1073K	GC, X-ray	two reaction mechanisms, (1) reaction of Zn(g) and stream at reactor wall (2) reaction between Zn(l) or Zn(s) and stream at particle Surface	average of 60% and 45% at 1023K and 1073K
liquid Zn Berman (2000)	723-773K	GC	Diffusion through ZnO is the rate determining	

			step. The order of reaction is $0<n<1$. Kinetic expression is $W_{sp} = kP_{H_2O}/(1 + bP_{H_2O})$	
commercial Zn Weidenkaff (mean size of (2000) 10μm) and solar Zn (mean size of 9μm)	623-773K	thermogravimetric analysis	reaction proceeds faster for molten Zn and Zn containing impurities	Zn content > 50% for commercial. Zn content < 10% for solar Zn

More recently, researchers at ETH proposed using Zn nanoparticles for the hydrolysis reaction. Due to large surface to volume ratio of nanoparticles, the application of those materials should promote the reaction kinetics, heat and mass transfer, and thus favor complete or nearly complete reaction. Ernst [88] et al. at ETH using thermogravimetric analysis measured the reaction rate of Zn particles at the temperature region just below the Zn melting point. A core-shell model was used to quantify the hydrolysis rate. However, conventional systems such as TGA are known to be corrupted by heat and mass transfer effects which greatly influences the accuracy of kinetics obtained by these methods [148, 149]. Furthermore, for the experiments using nanoparticles as the reactant, the particles they used may have a fairly wide size distribution. Since the reactivity could be different for different sizes of particles, the conversion rate they measured is a size-averaged value which may change as the particle size distribution changes. Thus, new tools and experiments are needed to probe the size-resolved intrinsic reaction kinetics of nanoparticles/nanocrystals. In our approach, we employ an on-line tandem ion-

mobility method which allows us to determine the intrinsic hydrolysis kinetics of in-situ generated unsupported Zn NCs by measuring the mass change of a single particle.

In this study, we focused on the reaction kinetics of Zn NCs hydrolysis at relatively low temperatures (100^{o}C-250^{o}C). From a practical point of view a lower reaction temperature is desirable from efficiency and materials engineering standpoint. Furthermore, low temperatures enable one to bypass the material loss problem due to Zn evaporation**.** Our preliminary experiments of Zn hydrolysis in the temperature range of 100^{o}C-250^{o}C have shown significant mass changes of Zn NCs. Some previous studies also show that hydrogen can be harvested by Zn hydrolysis at temperatures below 100^{o}C. For example, the theoretical and experimental work of Alimenti [150] and Bazan's [140] experiment on Zn disk prove that even the hydrolysis reaction of bulk Zn can proceed in the temperature range 21^{o}C-50^{o}C with the evolution of molecular hydrogen. Furthermore, studies of Zn corrosion in the outdoor atmosphere [151] primarily by moisture have indicated a measurable reaction rate of hydrolysis. According to Mattsson's experiment [152], the Zn corrosion rate under atmospheric exposure can be as high as 16 $\mu m / year$, which is about 2nm/hour and the reaction rates do not decrease with time [151]**.**

4.2 Experiment Setup

The experiment system is very much like the one for Zn NC oxidation study, which consists of three components. Preparation of monodisperse Zn NCs, exposure of size selected Zn NCs into a controlled temperature region, and finally,

measurement of the mass change resulting from hydrolysis. A complete schematic of the experimental system with temperature and flow rate control is shown in Figure 4.1. Our experiment consists of two different ion-mobility schemes in series. The first mobility characterization is to size select NCs with a differential mobility analyzer (DMA) [104]. The second mobility characterization employs an aerosol particle mass analyzer (APM) and measures changes in mass resulting from a controlled hydrolysis of the Zn NCs.

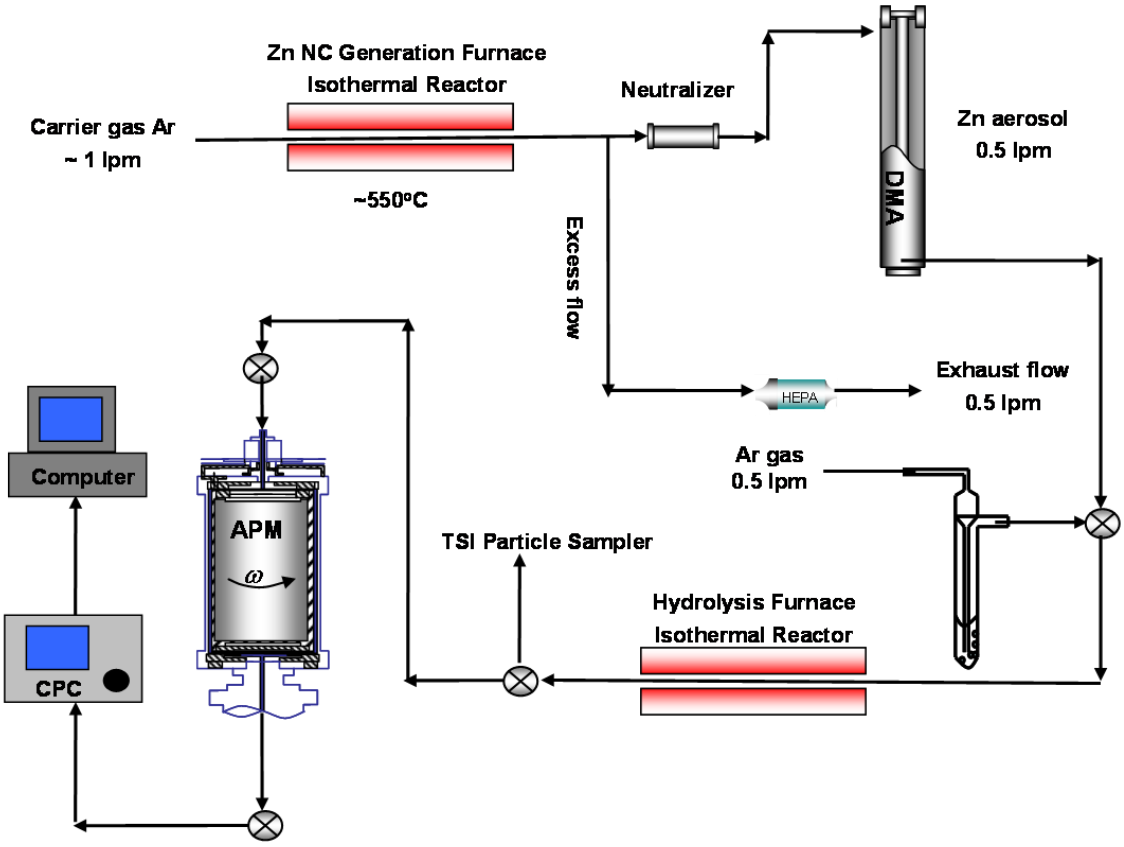

Figure 4.1 Experimental system for Zn, generation, size selection by DMA, hydrolysis and subsequent mass analysis with the APM.

Water vapor is generated by bubbling Ar gas at a flow rate of 0.5 LPM (liter per minute) through heated distilled water. In order to prevent any condensation of water vapor in the gas lines, the whole water injection system is wrapped with heating tapes and heated to ~70^{o}C. Two diffusion dryers are placed between the hydrolysis furnace and the APM sampling port to prevent water condensation in the instruments.

Since we are employing ion-mobility methods, particles are first charged to a Boltzmann charge distribution by exposing the nanoparticle aerosol to a Po-210 source, before the DMA. The average charge state of sample particles under Boltzmann distribution is quasi-neutral, with most of particles uncharged and equal amount of particles carry +/- 1 charge and +/-2 charges, etc. For example, in case of 50 nm particles, 60.2% particles will be neutral, 19.3% carry +/-1 charge, 0.6% carry +/- 2 charges, and higher charge state would be even less. Considering the small percentage in the multiple charged states, we ignore multiple charged particles. Both the DMA and APM are configured to classify positively charge particles for these experiments.

4.2.1 In-situ Generation of Monodisperse Zn NCs

The Zn NCs generation method is the same as oxidation and evaporation studies. An evaporation/condensation method is used. Argon is the carrier gas. Granular Zn (purity, ≥99.99% from Sigma-Aldrich) contained in a small ceramic boat was placed in a tube furnace at 550^{o}C to generate a flow of Zn vapor. The Zn vapor condenses as it exits the tube furnace and by empirical adjustment of the tube furnace temperature,

and the argon carrier gas flow rate we were able to form unagglomerated Zn NCs. Since our objective is to study size resolved reactivity we use a DMA as a band pass filter to generate monodisperse NCs. The DMA selects size based on the electric mobility which is related to the drag force and charge on a particle.

4.2.2 The DMA-APM System

The same DMA-APM system used for Zn NC oxidation and evaporation studies was used in this study. The DMA was used in this experiment for generating monodisperse NCs. The APM measured the mass change of individual particles due to hydrolysis.

4.2.3 Zn Nanocrystals Characterization, Sampling and Hydrolysis

In our experiment, Zn NCs of initial ion-mobility size of 70nm were selected to study the hydrolysis reaction. After size classification, the Zn aerosol flow is mixed with Ar gas (carrying water vapor) at the ratio of 1:1 and then passes through a second tube furnace. This furnace enables the controlled hydrolysis of the Zn NCs. The total flow rate of the aerosol flow is 1 LPM at standard condition. The Zn particle concentration after the DMA size-selection is about 3000 per cm^3 and the Zn mass concentration in the hydrolysis furnace is about 4E-12 g/cc, assuming the particles are 70nm spherical particles and the density of Zn is 7.14g/cc.To monitor the small mass change of the NCs due to hydrolysis, an aerosol particle mass analyzer (APM) is

placed downstream. Particles exiting the APM will be selected on the basis of mass and are counted using a standard particle counting method, condensation particle counter (CPC).

In the experiment, the temperature in the hydrolysis furnace was set between 100-250^{o}C in increments of 25^{o}C. The particle mass distribution was then measured for each furnace temperature after the system reached steady state. The room temperature particle mass distribution was also taken, and set as the base of the mass measurement. Samples for electron-microscopic analysis were collected exiting the evaporation furnace by electrostatically precipitating the aerosol onto a TEM grid.

4.3 Results and Discussion

4.3.1 Zn Nanocrystal Morphology

Figure 4.2 shows the SEM image of two single Zn NCs that were deposited from the gas phase by electrostatic precipitation onto a TEM grid before size-selection. The NCs show the shape of near perfect hexagonal prisms. Energy dispersive X-ray (EDS) spectra obtained from the NCs in SEM confirmed that the composition is Zn. Selected Area Electron Diffraction analysis indicated that the Zn NCs have top surfaces of $\{0001\}$ crystal planes and have side surfaces of $\{1\bar{1}00\}$ planes.

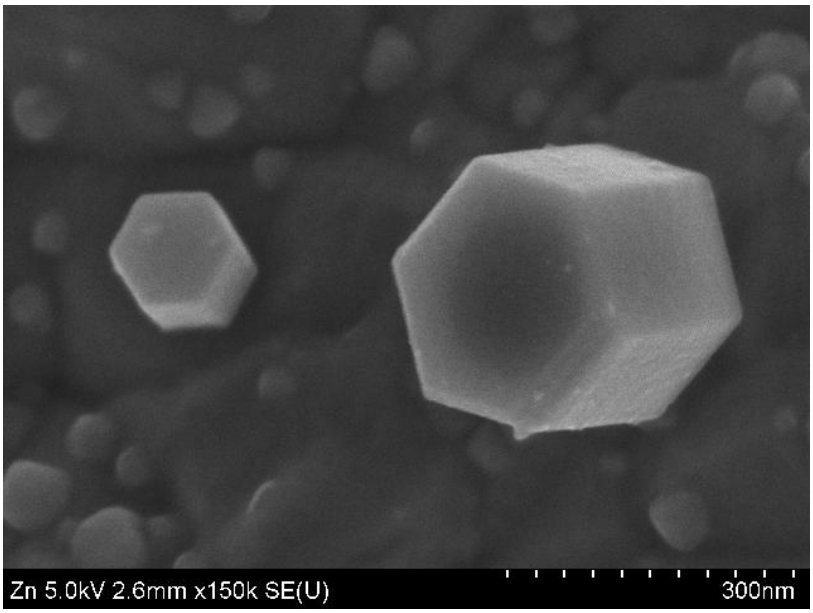

Figure 4.2: SEM image of the hexagonal-prism-shaped Zn NCs (before size-selection).

4.3.2 Zn Nanocrystal Mass Measurement

Figure 4.3 shows the normalized particle mass distributions for 70nm mobility size Zn NCs reacting with water vapor at different temperatures. Figure 4.3(a) and 4.3(b) are corresponding to a water vapor fraction of 3% while figure 4.3(c) and 4.3(d) are for the water vapor fraction of 15%. In each plot, the particle number concentration is plotted against the particle mass. These distributions are obtained from APM-CPC measurements. The particle number concentration is obtained with a condensation particle counter (CPC) while changing the APM voltage. Each data point in Figure 4.3 is a time average of ~1min of CPC counts in order to minimize the effect of system instability. The peak mass of Zn NCs at each hydrolysis temperature

is obtained by fitting the experimental data using a Gaussian distribution. From Figure 4.3(a) and 4.3(c), we can see that as we increase the hydrolysis temperature, the particle mass distributions shift to the larger mass side, which indicates that Zn NCs gain weight by reacting with water. However, upon further increase in the reaction temperature, the particle masses decrease as can be seen from Figure 4.3(b) and 4.3(d). Similar trends of mass change has also been observed for 100nm Zn NCs. Figure 4.4 displays the plots of Zn NC mass as a function of reaction temperature for 70nm Zn NCs based on the results of particle mass measurement. Also shown in these plots is the residence time corresponding to each hydrolysis temperature. The residence time is determined using the following equation:

$$\tau = \int_0^L \frac{1}{u(x)} dx \tag{1}$$

where L is the length of the tube and $u(x)$ is the flow velocity, which can be calculated below as:

$$u(x) = \tfrac{4}{3} u_{\mathrm{m}} \frac{T(x)}{T_0} \tag{2}$$

where 4/3 u_m is the peak flow velocity of carrier gas calculated from volume flow rate and the cross sectional area of the flow tube under the assumption of laminar flow. $T(x)$ is temperature distribution within the tube at each furnace set point.

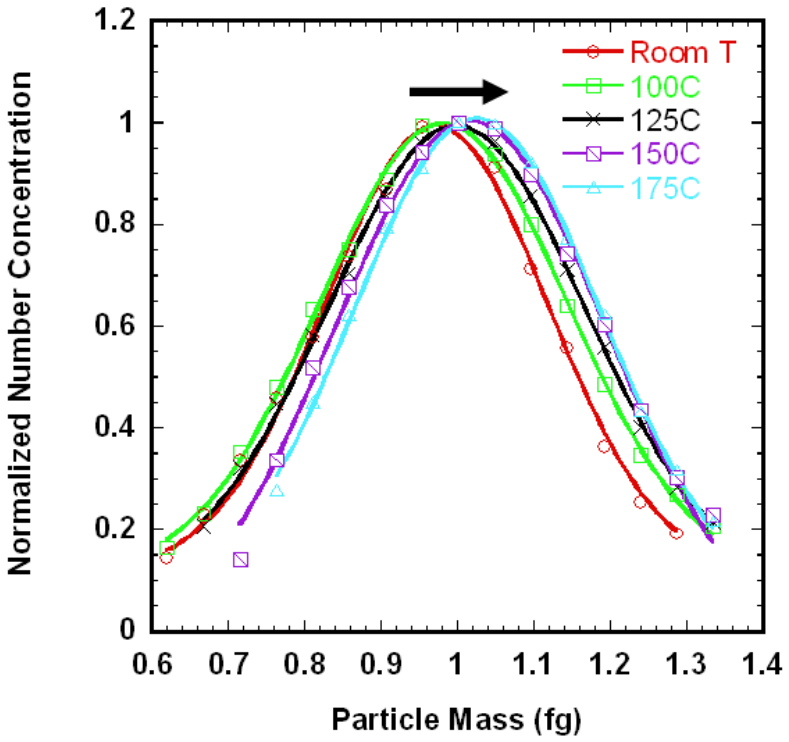
Normalized Number Concentration
Particle Mass (fg)
Room T
100C
125C
150C
175C
1.2
1
0.8
0.6
0.4
0.2
0
0.6
0.7
0.8
0.9
1
1.1
1.2
1.3
1.4

(a)

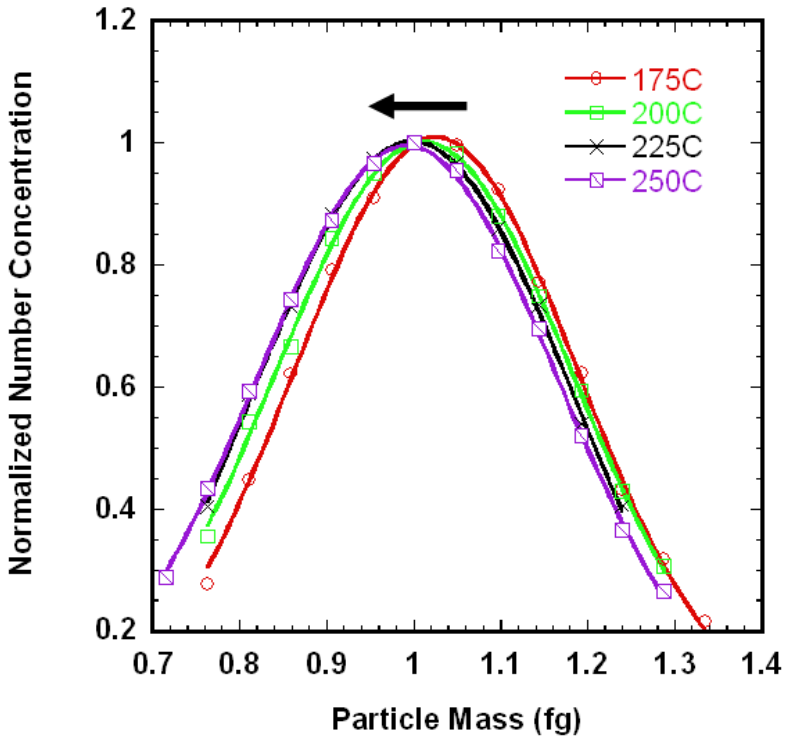
Normalized Number Concentration
Particle Mass (fg)
175C
200C
225C
250C
1.2
1
0.8
0.6
0.4
0.2
0.7
0.8
0.9
1
1.1
1.2
1.3
1.4

(b)

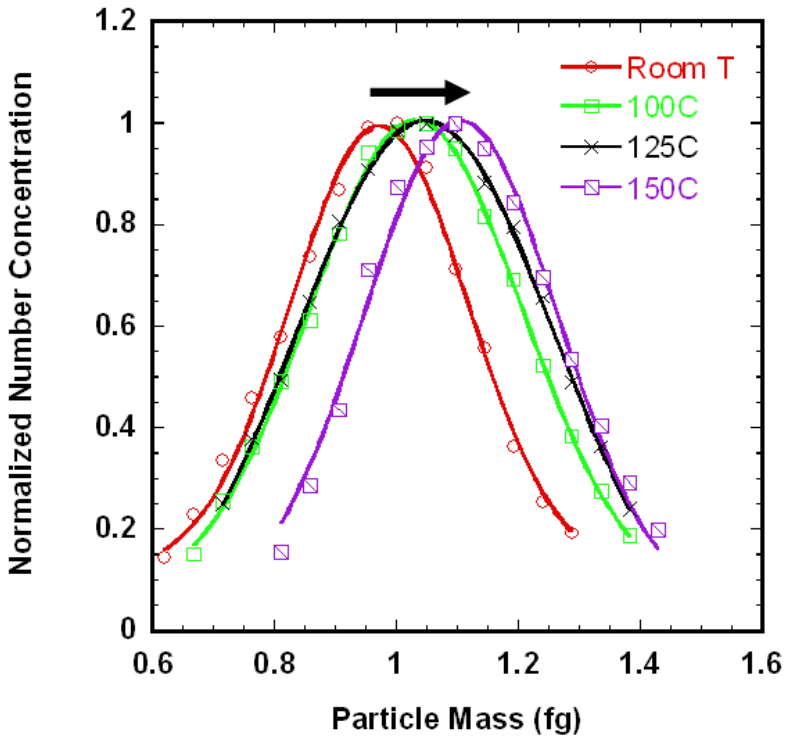
Normalized Number Concentration
Particle Mass (fg)
Room T
100C
125C
150C
0
0.2
0.4
0.6
0.8
1
1.2
0.6
0.8
1
1.2
1.4
1.6

(c)

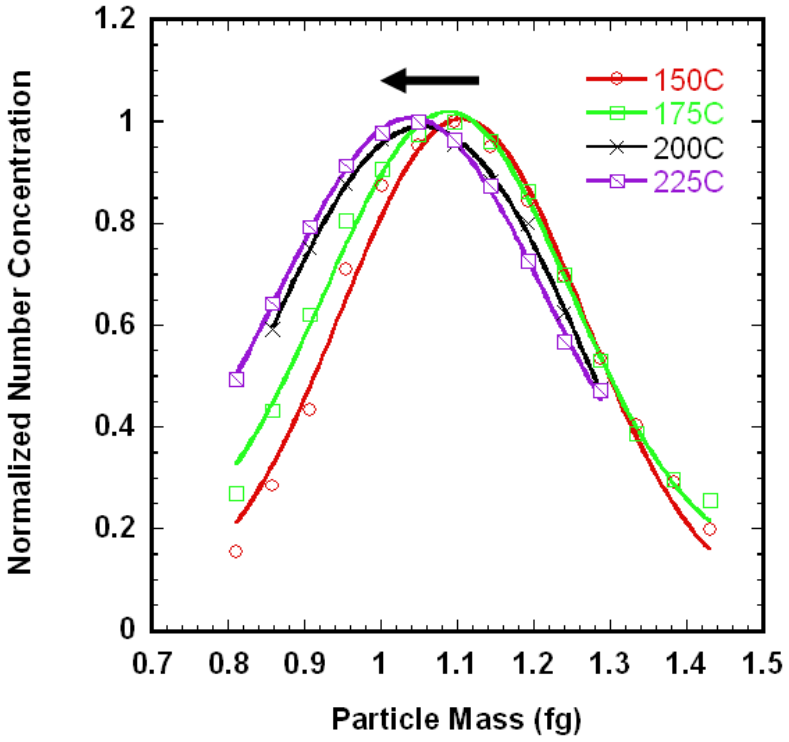
Normalized Number Concentration
Particle Mass (fg)
150C
175C
200C
225C
0
0.2
0.4
0.6
0.8
1
1.2
0.7
0.8
0.9
1
1.1
1.2
1.3
1.4
1.5

(d)

Figure 4.3: Normalized particle mass distributions for 70nm mobility size Zn NC at different hydrolysis temperatures. Plots (a) and (b) are for the water vapor fraction of 3%. Plots (c) and (d) are for the water vapor fraction of 15%.

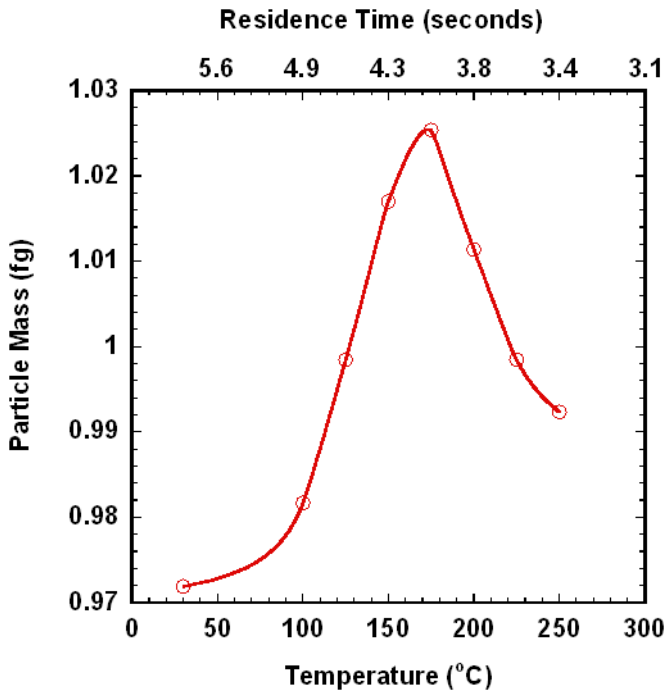

(a)

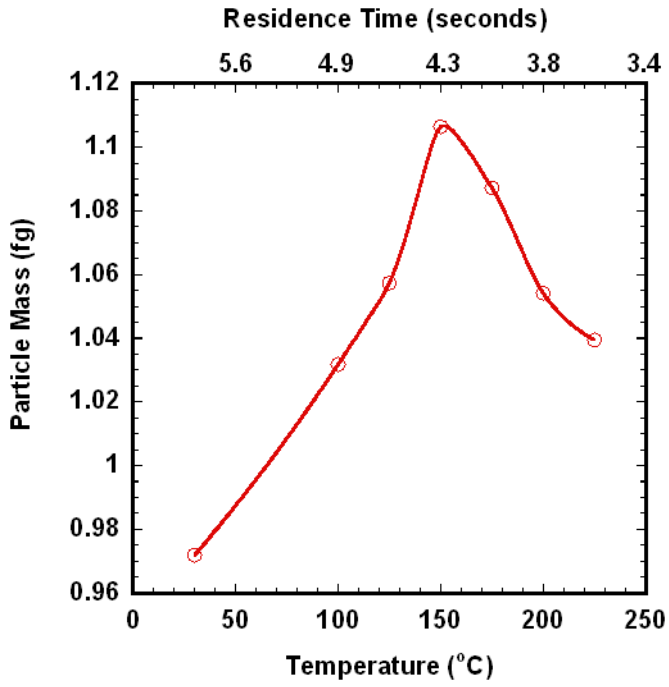

(b)

Figure 4.4: Particle mass vs. hydrolysis temperature for 70nm Zn NCs. (a) 3% water vapor fraction (b) 15% water vapor fraction.

4.3.3 Low Temperature Zn Hydrolysis Reaction Mechanism

Based on the mass change behavior of Zn NCs during hydrolysis as a function of temperature, we proposed the following reaction mechanism:

At relatively low temperature (below 150°C) Zn NCs can react with water and generates solid zinc hydroxide and releases hydrogen gas. The reaction proceeds as follows:

$$Zn + 2H_2O \rightarrow Zn(OH)_2 + H_2 \quad \text{(I)}$$

Since zinc hydroxide ($Zn(OH)_2$) has a low decomposition temperature (there is a range of reported $Zn(OH)_2$ decomposition temperature from 125°C to 196°C), higher termperatures lead to zinc dydroxide decomposition via:

$$Zn(OH)_2 \rightarrow ZnO + H_2O \quad \text{(II)}$$

which competes with the hydrolysis reaction (I) and form ZnO. Thus, the overall reaction at high temperatures becomes $Zn + H_2O \rightarrow ZnO + H_2$. Since ZnO has a smaller molecular weight than $Zn(OH)_2$, the total mass of NCs begin to decrease as the temperature further increases. The above reaction mechanism is consistent with the reduction in mass as the temperature was increased. Our proposed mechanism is also supported by the following evidences:

First, both experimental and theoretical works [150, 153] studying ZnO thin film formation using chemical vapor deposition method have suggested that $Zn(OH)_2$ can be easily formed in the hydrolysis reaction, but the formation of ZnO is very endothermic.

Second, zinc hydroxide is the principal constituents of the Zn corrosion layers resulting from exposure to natural environments [151].

Third, based on the results of Alimenti's theoretical modeling study [150], when two water molecules were adsorbed onto Zn, the intermediary product was $Zn(OH)_2 + H_2$ and the equilibrium state was $ZnO + H_2O$. In our aerosol experiment, water is by far the sufficient reactant.

However, it is also possible that the reaction product is ZnO with some chemisorbed water, $ZnO \cdot nOH$ as suggested by Bazan [140].

To further determine the product composition, EDS experiment was conducted on the hydrolyzed NCs. Figure 5 shows the results of Energy Dispersive X-ray (EDS) analysis of 70nm Zn NCs after reaction with water vapor at 100^{o}C. The sample was collected by electrostatically precipitating the aerosol onto a TEM grid. The TEM image in Figure 5 clearly shows that the hydrolyzed Zn NC exhibits a core-shell structure. The EDS results indicate a higher concentration of elemental oxygen on the NC shell. However, due to the limit of the EDS system, we could not detect the existence of hydrogen in the NCs.

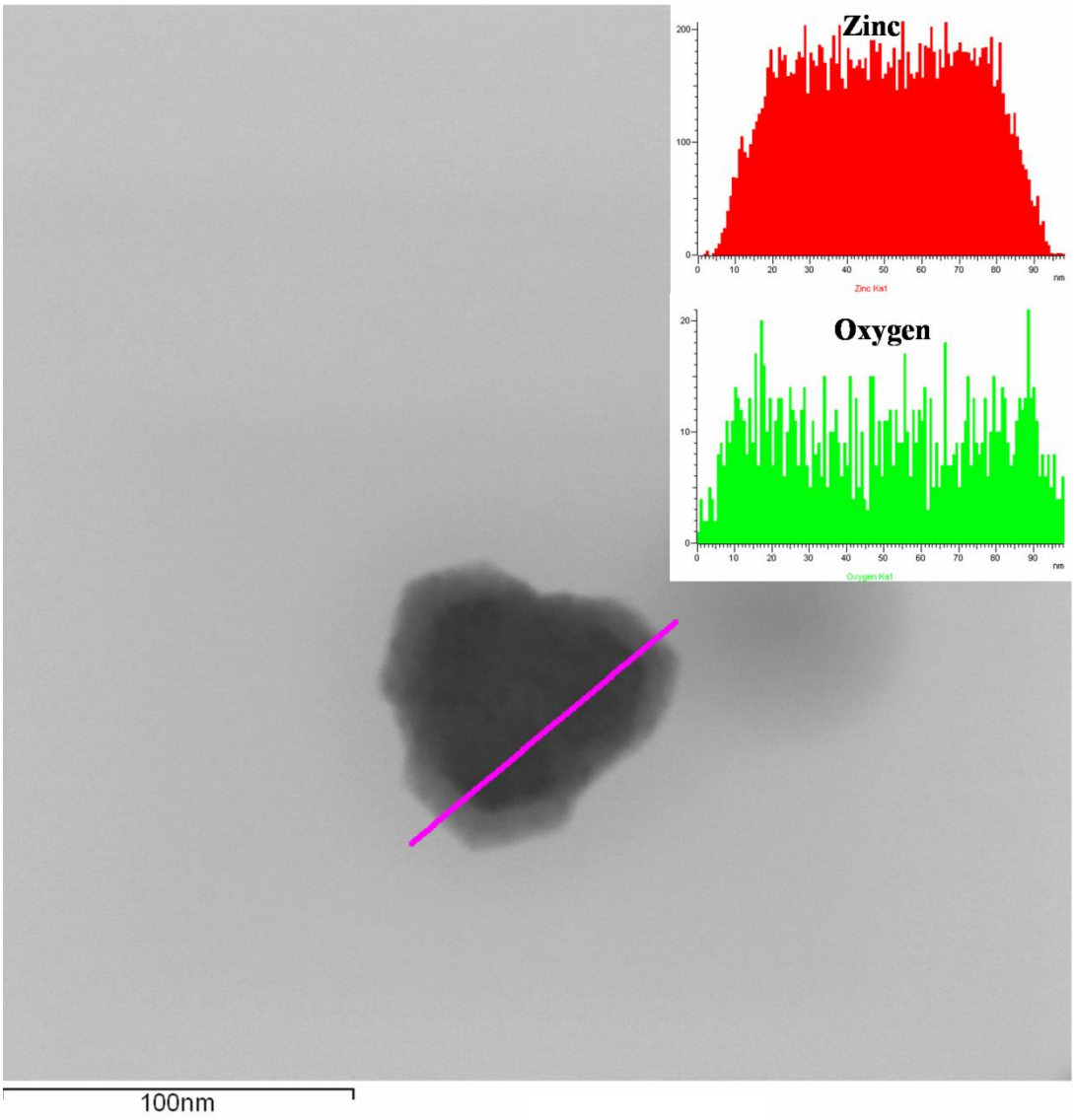

Figure 4.5: EDS analysis of a 70nm Zn nanocrystal hydrolysis at 100^{o}C.

The extremely low mass loading (of the order of femtogram) in an aerosol experiment prevents the usage of conventional material characterization method such as TGA and XRD which require milligrams of materials. To further verify the proposed reaction mechanism, a fixed-bed reactor configuration was employed with commercial Zn powders (Sigma-Aldrich, purum, ≥ 99%, more than 95% of the particles are not larger than 45nm). The reactor was made of a 3/8" ID, 25cm long

stainless tube filled with Zn powder and externally heated 100°C. A carrier nitrogen gas flow of 3 sccm containing 15% mole fraction water vapor was passed through the Zn bed. After reacting with water vapor for ~ 30 minutes, the hydrolyzed Zn powder was harvested for TGA analysis.

Figure 4.6 shows the TGA results of the hydrolyzed commercial Zn powder. From the figure, we can clearly see two plateaus in the sample mass curve. The first mass plateau was reached at about 90°C when all the absorbed water in the sample was evaporated. As the TGA temperature was increased a second plateau is seen, which we believe is consistent with weight loss due to the decomposition of $Zn(OH)_2$. The decomposition onset temperature is estimated from the TGA results to be ~120°C. Further mass loss at higher temperatures is associated with evaporation of the unreacted Zn (Ma X. et al. unpublished). Based on the mass difference between the two mass plateaus, we estimate the original percentage of conversion from Zn to $Zn(OH)_2$ in the sample to be ~36%. The TGA experiment confirms that $Zn(OH)_2$ is formed during the hydrolysis of nano-sized Zn particles at temperature around 100°C. To determine the gas products from Zn hydrolysis reaction in the fixed-bed reactor the reactor gas effluent was also sampled into a mass spectrometer (Stanford Research Systems, UGA 300). Hydrogen was observed during the hydrolysis of commercial Zn powder at 100°C.

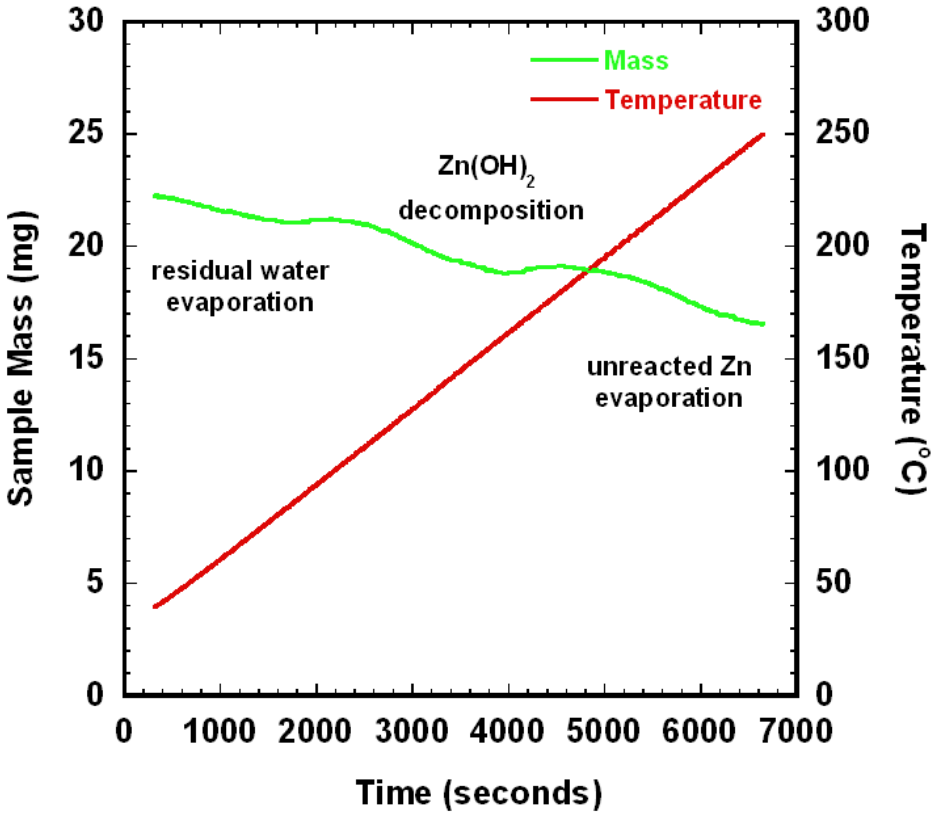

Figure 4.6: TGA measurement of the hydrolyzed commercial Zn powder reacted with water vapor at 100°C for ~30 minutes.

Based on the proposed hydrolysis mechanism, complete Zn to $Zn(OH)_2$ conversion has been achieved on the in-situ generated Zn NCs. Figure 4.7 shows a particle mass distribution of 70nm Zn NCs reacted with 19% mole fraction of water vapor at residence times of ~ 10 seconds. Based on the peak mass of Zn NCs, we can confirm that the 70nm Zn NCs were fully converted into zinc hydroxide at the temperature of 175°C. The inset in Figure 4.7 shows the percentage of conversion as a function of furnace temperature. Compared with the hydrolysis of commercial Zn powder in the fixed-bed reactor, the hydrolysis of unsupported Zn NCs enjoys a much higher conversion rate. It is well known that bulk methods suffer from heat and mass

transfer effects, milligrams of an aggregated sample are needed, while the sample mass of our aerosol based techniques is ~ 1 fg and is being performed on an isolated NC.

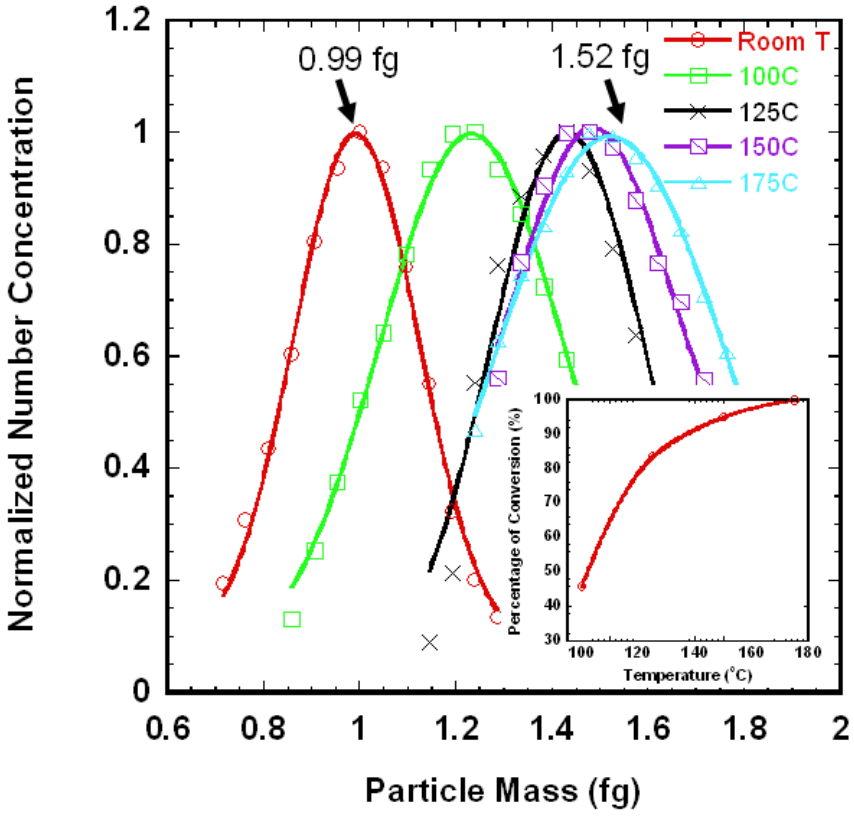

Figure 4.7: Particle mass distributions for 70nm Zn nanocrystals reacting with 19% mole fraction of water vapor at different temperatures. (Inset) percentage of conversion as a function of temperature.

Compared with the overall hydrolysis reaction $Zn + H_2O \rightarrow ZnO + H_2$, the reaction (II) can proceed at lower temperatures and release hydrogen, which makes Zn hydrolysis more energy efficient and can bypass the material loss problem due to Zn evaporation at high temperatures.

4.3.4 Kinetics of the Hydrolysis Reaction

It is assumed that the reaction rate for Zn NC hydrolysis reaction follows an Arrhenius law. In our experiment, the reaction rate k are approximated by the average mass change rate $\frac{\Delta m}{\tau}$ (Δm is the mass difference measured by DMA-APM and τ is the residence time) of the NCs. The activation energy of the Zn hydrolysis can be extracted by plotting the reaction rate as a function of reaction temperature in an Arrhenius form. Figure 4.8 shows the Arrhenius plots for 70nm Zn NCs hydrolysis at different water mole fractions. The slopes of the straight lines are roughly equal to each other which suggests that we are measuring the same mechanistic process, and yield an overall activation energy of $24 \pm 2 kJ/mol$ for the reaction (I). Previous studies on sub-micron Zn powders and nanoparticles showed strong discrepancies in the Zn hydrolysis activation energy, ranging from 132kJ/mol [147] to 43kJ/mol [144]. The big differences in activation energy can be explained by initial oxide content and morphology of the reacting particles prepared by different methods [146]. Those studies measured the activation energy based on the reaction $Zn + H_2O \rightarrow ZnO + H_2$. Unfortunately, no comparable kinetic data have been reported for the reaction $Zn + 2H_2O \rightarrow Zn(OH)_2 + H_2$ for which we can compare our studies on free Zn NC's.

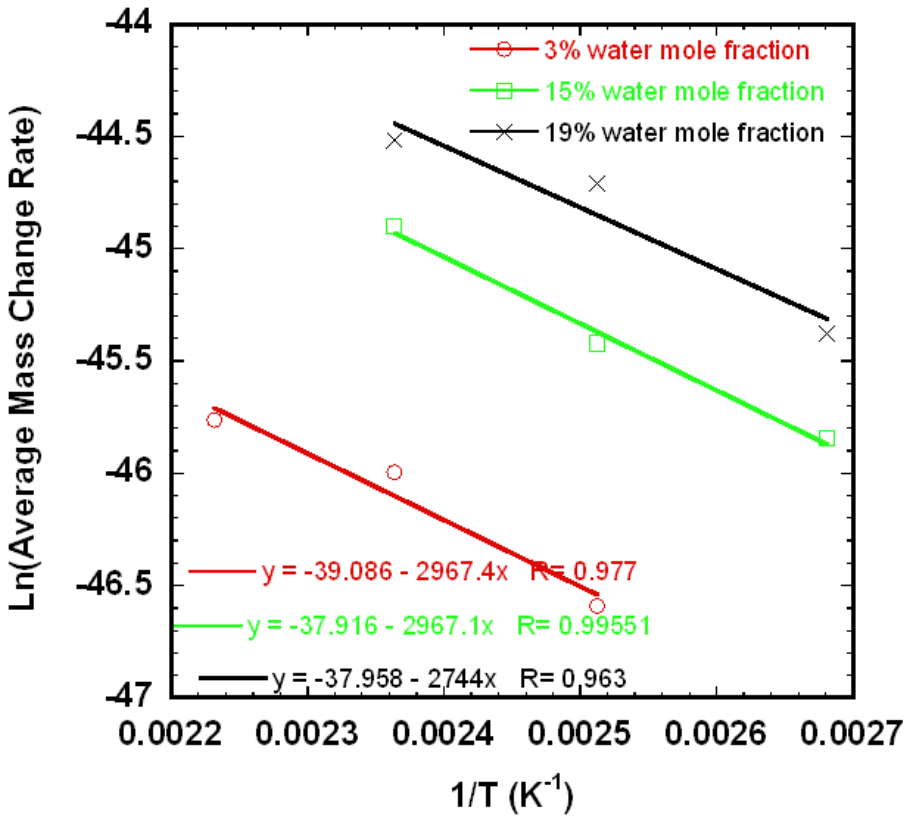

Figure 4.8: Arrhenius plot of the reaction rate for 70nm Zn NCs hydrolysis at different water vapor concentrations

Since the reaction rate depends strongly on the water vapor concentration, the experimental data are fitted to determine the reaction order n with respect to the water vapor mole fraction y. The least square fit of the reaction rates yields a dependence of 0.9 ± 0.1^{th} order on the water vapor mole fraction and a pre-exponential factor A equals to $0.012\ fg/nm^2 s$. Based on water vapor flux and the mass change rate of the NC an effective sticking coefficient of water molecules hitting Zn NCs was also calculated. This value is estimated to be between 10^{-7} to 10^{-6} in the temperature range investigated. A first order dependence on water concentration and a low value of effective sticking coefficient imply that the hydrolysis reaction is limited by the

diffusion of water molecule or water fragment through the hydroxide layer and this diffusion depends on the water solubility on the NC surfaces. For comparison, Frank et al.[144] investigated the hydrolysis rate of Zn particles by up to 50 mol% water vapor at 330-360^{o}C and found a reaction order of 0.5th on water vapor mole faction. Bazan et al.[140] studied the interaction between metallic zinc and water vapor and reported a 0.8th dependence on relative humidity in the temperature range 20-50^{o}C.

To summarize, the overall kinetics of the hydrolysis reaction for 70nm Zn NCs can be written as:

$$k = Ay^{n} \exp(-\frac{E_a}{RT}) \tag{3}$$

where $A = 0.012\ fg/nm^2 s$ is the pre-exponential factor, $n = 0.9 \pm 0.1$ is the reaction order with respect to the water vapor mole fraction and $E_a = 24 \pm 2 kJ/mol$ is the reaction activation energy. A comparison between of the experiment and the model of the reaction kinetics is shown in Figure 4.9 in which the measured reaction rate is plot against the calculated reaction rate using equation (3). A good agreement is found over the entire experimental range.

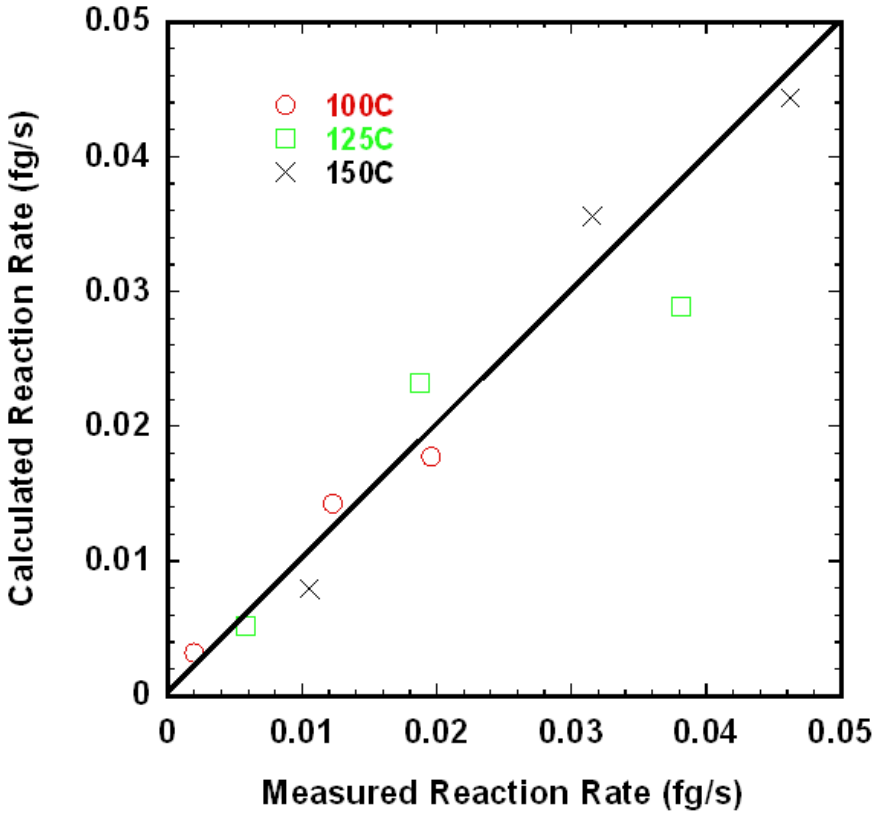

Figure 4.9 Calculated reaction rate based on equation (4) vs. measured reaction rate for 70nm Zn NCs.

4.4 Conclusions

In conclusion, we have successfully generated size-classified Zn NCs and have demonstrated that the hydrolysis kinetics of free Zn NCs can be studied by an in-flight tandem DMA-APM method. Based on the mass change of Zn NCs, we proposed a low temperature reaction mechanism for Zn NC hydrolysis. At low temperatures (below 150^{o}C) Zn NCs can react with water and generates solid zinc hydroxide and releases hydrogen gas. At higher temperatures, the zinc hydroxide

decomposition reaction $Zn(OH)_2 \rightarrow ZnO + H_2O$ starts to competes with the hydrolysis reaction and form ZnO. This mechanism is consistent with the experiment observations and can produce hydrogen at the temperature range of about 100-150^oC. Based on the proposed mechanism, complete conversion of 70nm Zn NC was achieved at the temperature of 175^oC with the residence time of 10 seconds and water vapor mole fraction of 19%. An Arrhenius law was used to extract the reaction kinetic parameters. The activation energy of the hydrolysis reaction for 70nm Zn NCs is determined to be $24 \pm 2 kJ/mol$ and the reaction order with respect to the water vapor mole fraction is found to be 0.9 ± 0.1.

Chapter 5: Catalytic Decomposition of Liquid Hydrocarbons in an Aerosol Reactor: A Potential Solar Route for Hydrogen Generation

5.1 Introduction

Any realization of hydrogen economy depends on the availability of large quantities of hydrogen produced at low cost. The hydrogen economy is environmental-friendly only when the production of hydrogen is CO_2 free. Currently, hydrogen is produced mainly through steam reforming of natural gas followed by the water gas shift reaction of CO[5]. The reaction is highly endothermic, and hence requires a substantial energy input. Furthermore, the water gas shift reaction is a major source of industrial CO_2. If the CO_2 by-product cannot be fully used or sequestrated, the environmental gain from using hydrogen as an alternative fuel to hydrocarbons is largely lost. One of the hydrogen production methods that can address these two issues simultaneously is thermal decomposition of hydrocarbons into hydrogen and carbon [47, 49, 65]. It provides an alternative, one-step process to produce hydrogen of the required purity. The process is oxygen free thus produces no oxidative products CO/CO2. This feature is important to polymer electrolyte membrane (PEM) fuel cells since PEM fuel cells require hydrogen with very low CO

concentration (<10ppm). Currently, a multiple-step process is required to produce high purity hydrogen which involves steps to produce synthesis gas, water–gas shift reactions to convert CO to CO_2 and H_2, and various purification steps to reduce the CO to ppm levels. Compared with that, the H_2 separation in the thermal decomposition process is relatively easy since the major carbon product is in solid phase. The solid carbons are easier to separate, handle, transport and store than gaseous CO2 and the product hydrogen can be supplied directly to PEM fuel cells. If taken to completion, the by-product of the decomposition could be tuned to produce valuable carbon products such as carbon black, carbon nanotubes or carbon filaments. Because of these attractive advantages of thermal decomposition, there is an increasing interest in this area. However, most studies have addressed the decomposition of methane. From a thermodynamic point of view, the decomposition of liquid hydrocarbons is favored over methane since 1.5-2 times less energy is needed to produce a unit volume of hydrogen[76]. From a practical point of view, decomposition of liquid fuel is more suitable for onboard hydrogen generation, since the current transportation, storage and dispersal infrastructure for gasoline can be easily modified for other liquid fuels. Finally, methane combustion produces the lowest GWP products since it is a hydrocarbon with highest fraction of hydrogen.

Sunlight provides by far the largest of all carbon-neutral energy sources. Basically, three pathways have been identified for producing hydrogen using solar energy [33]. They are electrochemical, photochemical, and thermochemical. The last method uses concentrated solar radiation as the energy source of high-temperature process heat for chemical transformations. Modern solar-concentrating systems can achieve maximum

concentration factors in the 1500-5000 range and provide high-temperature solar thermal heat exceeding 2000^{o}C, thus is capable of driving very endothermic chemical reactions. Various solar thermochemical routes have been proposed, some of them have been tested on a solar reactor. For example, Zn/ZnO redox pair [42, 154] is considered as one of the most favorable candidate for 2-step water-splitting thermochemical cycle for hydrogen production and exploratory tests on the first step of the cycle which is the solar dissociation of ZnO, have been carried out successfully in solar furnaces at high temperatures (>1500K) [155, 156]. Solar thermochemical decarbonization of hydrocarbons is also a promising process. Solar furnaces and reactors have been employed to study the decomposition of gaseous hydrocarbons [82, 157, 158] such as methane and butane for the catalytic production of hydrogen and filamentous carbon. Some novel reactor designs have been proposed and tested. For example, Dahl et al [82]. designed a solar tubular quartz reactor containing fine carbon black particles suspended in a CH_4 feed gas stream, a dissociation up to 90% was obtained at 2133K. Hirsch [81] and his co-worker designed a solar chemical reactor features a vortex flow of CH_4 confined to a cavity-receiver and laden with carbon particles that serve simultaneously as radiant absorbers and nucleation sites for the heterogeneous decomposition reaction. A maximum chemical conversion of CH_4 to H_2 and C was 67% at 1600 K and 1 bar. Those solar reactor designs can be easily modified to use liquid hydrocarbons as the feedstock. Considering the fact that decomposition of liquid fuels requires less energy input than the decomposition of methane, solar thermal process of liquid hydrocarbons should achieve higher conversion rates. Even more so if catalytic process enhance the decomposition rate or

conversion efficiency at a given temperature.

We begin by discussing prior relevant work on liquid fuel thermal decomposition. Otsuka et al.[159] examined the decomposition of various alkanes over Ni/fumed silica catalysts at 773K. Hydrogen and carbon nanofilaments were found as the major products with a low concentration of methane. The authors concluded that gasoline range alkanes (C6-alkane, C_8H_{18}) were superior to the light alkanes (<C4) for selective decomposition into hydrogen and carbon. Takenaka et al.[78] investigated the decomposition of various hydrocarbons (propane, n-butane, n-hexane, cyclohexane, toluene and n-octane) using a conventional gas flow system with a fixed catalyst bed over Ni based catalysts. They concluded that the saturated hydrocarbons could be a promising feedstock for hydrogen generation.

Metals (ions, atoms, clusters) are known to have a catalyst effect on the activation of carbon-carbon and carbon-hydrogen bonds in hydrocarbons. Transition and noble metal catalysts such as Ni, Fe, Cu, Co, Pt, Rh, Pd supported on high surface area ceramic substrates such as $A1_2O_3$ and SiO_2, have been investigated in the decomposition process of gaseous and liquid hydrocarbons [76]. Other novel catalyst and support materials have also been investigated for liquid fuel decomposition. For example, Ichikawa et al.[77, 160] investigated the dehydrogenation of cyclohexane, methylcyclohexane and decalin over activated carbon supported Ni, Pt, and Ni–Pt catalysts at 287–375^{o}C. A conversion between 25–35% was found with the selectivity for dehydrogenation reactions above 98.8%. Okada et al. [161] developed a unimodal porous alumina supported dehydrogenation catalyst which yielded 95% methylcyclohexane conversion and give a 38% of theoretical H_2 yield, with the

primary product toluene. Wang et al. [162] used stacked-cone carbon nanotubes as a support to prepare Pt and Pd catalysts for the dehydrogenation of cyclohexane and methylcyclohexane, and later reported results [163] of alumina supported nano-scale binary catalysts for propane and cyclohexane decomposition. The catalyst has been shown to be very effective for the decomposition of lower alkanes to produce hydrogen and carbon nanofibers or nanotubes. The decomposition of Jet A mixture, cyclohexane, decalin were performed [128] over a hybrid catalyst, Pt/γ -Al_2O_3-ZrO_2/SO^{2-}. The acidity of the catalyst promote the cracking ability but also promotes coke formation and thus to rapid deactivation of the catalyst. The major challenges remaining in the catalyst development for decomposition are coking prevention, and performance enhancement. The majority of the studies were performed using conventional fixed-bed reactors with few using other reactor configurations.

In this study, we employ an aerosol reactor to study the decomposition of liquid fuels with emphasizes on the effect of fuel molecule structure on the hydrogen yield. The uniqueness of the work comes from conducting the decomposition over aerosol catalyst and producing hydrogen and carbonaceous aerosol. In this work catalyst iron nanoparticles were generated in-situ, and are in the aerosol state, thus can maximize the contact area between the fuel and the catalyst particles. With this approach the catalyst is a one-time use, and thus poisoning is not so great a concern and as such we can drive the chemistry harder. However, this approach necessarily requires that the catalyst material be inexpensive, and the use of precious metals or complex mixtures would not be considered practical. Thus the choice of iron. A second and equally

important aspect of this approach is that the hydrogen product is CO_2 free and easily separated from the other product of decomposition, carbonaceous aerosol.

5.2 Experimental

The catalytic decomposition of liquid fuels was performed in an aerosol reactor with a controlled gas flow system. Iron nanoparticle catalysts were generated on-the-fly by thermally decomposition of iron pentacarbonyl.

Previous studies by Karlsson et al. on iron carbonyl thermal decomposition [164] found that it was difficult to regulate the iron pentacarbonyl vapor flow because of its high volatility. To mitigate this problem we mixed the iron carbonyl directly into the liquid fuel and then bubbled argon through the mixture. The vapor composition is determined by the molar ratio of the two components according to Raoult's law.

The advantage of this approach is that due to the lower decomposition temperature of the iron carbonyl we initiate the catalyst production just prior to the initiation of the hydrocarbon decomposition chemistry. This minimizes the growth rate of the particles and thus maximizes surface area.

The aerosol reactor consists of a 22mm I.D. 25mm O.D. quartz tube within a 30 cm heated length, and with a nominal residence time of ~ 1 min. The gaseous product was characterized by a mass spectrometer (Stanford Research UGA 300) which also monitored the hydrogen and argon partial pressures with time. Argon was used as an inert internal standard and to determine the volume change of gaseous reactants and products during the reaction so as to assign concentrations. The mass of the fuel was

measured each time before and after the experiment to calculate the fuel consumption rate. Samples for electron microscopic analysis were collected by electrostatically precipitating the aerosol onto a TEM grid using an electrostatic precipitator. Since a lot of materials were deposited on the wall of the quartz reactor tube, XRD analysis was employed to determine the composition of the wall deposit.

To study the effect of fuel molecular structure on the overall hydrogen conversion, different types of hydrocarbon fuels were selected according to the classification: saturated hydrocarbons, unsaturated hydrocarbons, cycloalkanes and aromatic hydrocarbons. N-octane (Sigma-Aldrich, reagent grade, 98%) was used in the experiment as a representing straight-chain saturated hydrocarbon. Iso-octane (also named 2,2,4-Trimethylpentane, Sigma-Aldrich, ACS spectrophotometric grade, ≥99%) was selected to investigate the chain branching effect of alkanes. 1-octene (Sigma-Aldrich, 98%) was chosen as the representing unsaturated hydrocarbon with one carbon-carbon double bond. Toluene (EMD, >99.5%) was used as the representing aromatic hydrocarbon and methylcyclohexane (Sigma-Aldrich, ReagentPlus, 99%) which differs with toluene only in the benzene ring was selected as the representing cycloalkane. The physical properties of the fuels are listed in Table 5.1.

Table 5.1 Physical properties of the fuels investigated

	Density at 25^{o}C (g/ml)	Purity (%)	Vapor Pressure (torr)	Melting Point (^{o}C)	Boiling Point (^{o}C)

n-octane	0.703	98	11 (20^oC)	-57	125-127
iso-octane	0.692	>99	41 (21^oC)	-107	98-99
1-octene	0.715	98	15 (20^oC)	-101	122-123
toluene	0.865	>99.5	22 (20^oC)	-93	110-111
methylcyclohexane	0.77	99	37 (20^oC)	-126	101

5.3 Results and Discussion

5.3.1 Hydrogen Yield from Thermal Decomposition of Different Liquid Fuels

To investigate the effect of fuel molecular structure on the hydrogen generation, thermal decomposition of different hydrocarbons were performed under the same experiment condition, and hydrogen yield for each fuel were calculated as a function of decomposition temperature based on the following equation:

$$Y_{H_2} = \frac{X_{H_2} V_{in} Z_{expansion}}{a \cdot V_{1mole} \cdot r_{fuel,in}}$$

where Y_{H_2} is the hydrogen yield, X_{H_2} is the hydrogen mole fraction in the gaseous product, V_{in} is the input flow rate, $Z_{expansion}$ is the gaseous expansion factor determined from the change of argon partial pressure, a is the stoichiometric factor for complete conversion of a particular fuel to hydrogen, V_{1mole} is the volume of 1 mole ideal gas at room temperature and $r_{fuel,in}$ is the fuel injection rate in moles per minute, which was determined by measuring the mass change of the liquid fuel before and after each

experiment run. Using the above equation, the hydrogen yields from pure thermal decomposition of different liquid hydrocarbons were calculated and shown in Figure 5.1.

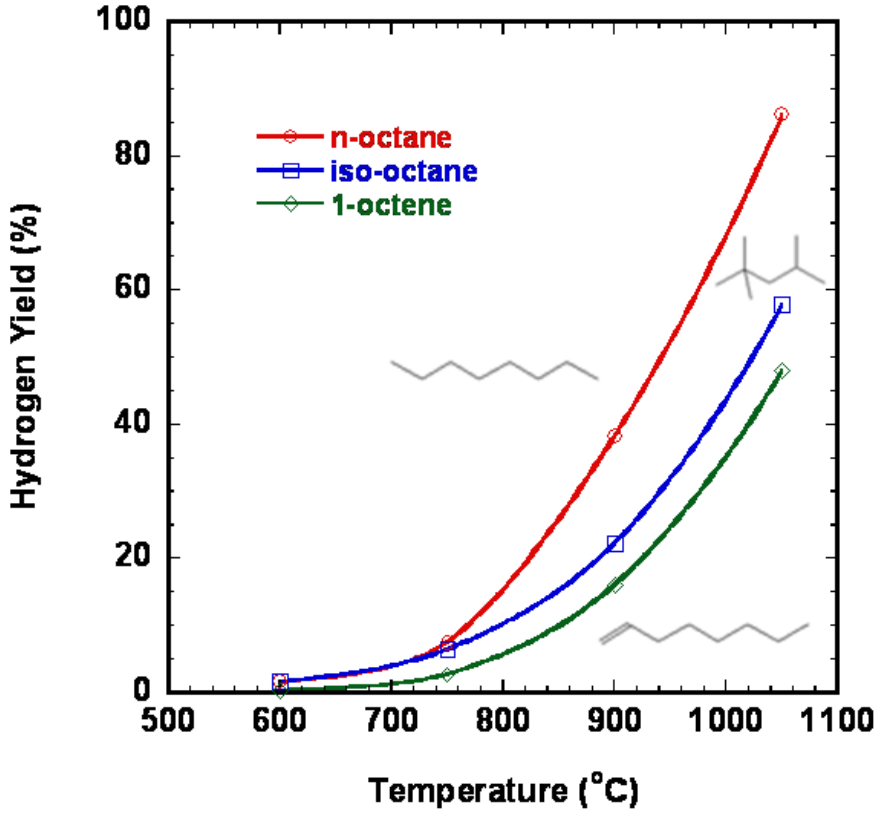

(a)

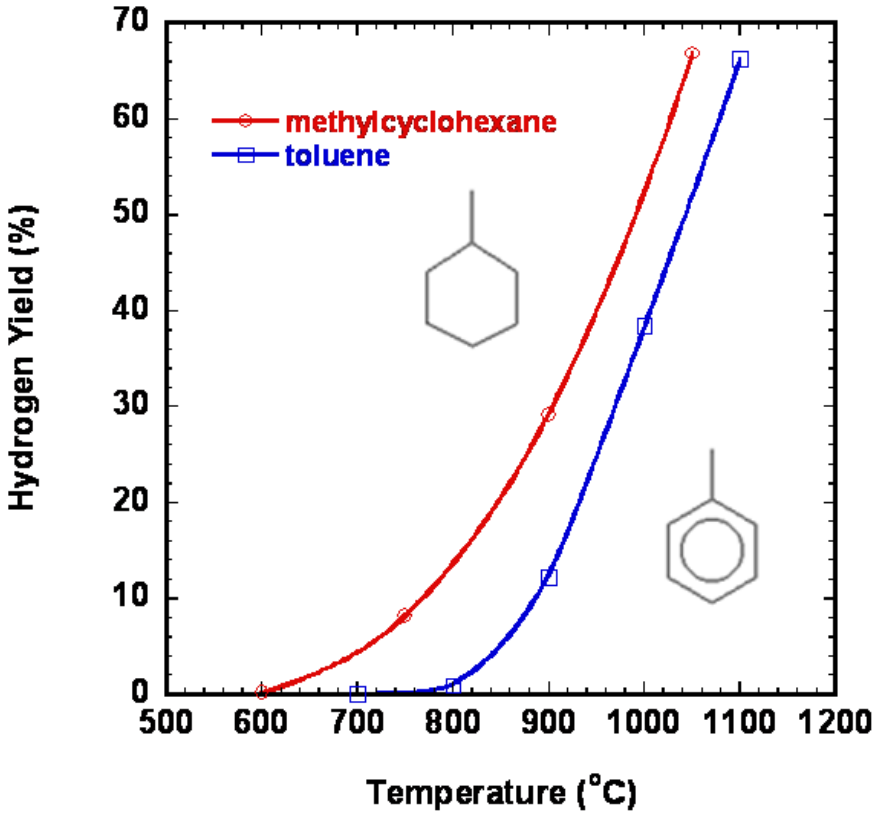

(b)

Figure 5.1: Hydrogen yields from thermal decomposition of fuels (a) hydrogen yields from n-octane, iso-octane and 1-octene (b) hydrogen yields from methylcyclohexane and toluene

As we can see from the plots, except for toluene, all other fuels start to release hydrogen at around 600°C. For toluene, the onset temperature of hydrogen generation is about 800°C, which reflects the greater stability of aromatic structures. The general trend of ease of thermal decomposition is alkanes > alkenes and cycloalkanes > aromatics. Compared with the three fuels in Figure 5.1(a), (These fuels have the same carbon number and differ only in the carbon skeleton and bond order) n-octane has the highest hydrogen yield and both n-octane and iso-octane outperform their alkene

counterpart (1-octene) in terms of hydrogen yield. However, different from the thermal cracking in petrochemical industry, where branched hydrocarbons are always found to be more reactive than their straight-chain counterparts [165], the straight-chain n-octane outperforms its branched-chain counterpart (iso-octane) in hydrogen production. Since carbon-carbon bond scission is the principal reaction during cracking, while hydrogen generation is more related to the C-H bond strength, a comparison of the C-H bond configurations in the three fuels may reveal some insights about trend in overall hydrogen yield. Table 5.2 shows the number of each C-H bond type, bond dissociation energy, and the percentage of total C-H bonds in n-octane, iso-octane and 1-octene molecules. Clearly, iso-octane has the highest percentage of C-H primary bonds, and n-octane has the highest percentage of secondary C-H bonds. Even though iso-octane has one tertiary C-H bond which is the easiest to dissociate, the fact that the majority of C-H bonds in iso-octane are primary C-H bonds means it's harder to decompose than n-octane. As for 1-octene, the existence of three H-C=C bonds makes it extremely hard to decompose since the hydrogen atom attached to the C=C double bond has much higher bond dissociation energy (460kJ/mol).

Table 5.2. C-H bond types in n-octane, iso-octane and 1-octene

	Number of primary C-H bond (bond dissociation	Number of secondary C-H bond (bond dissociation	Number of tertiary C-H bond (bond dissociation	Number of H-C=C bond (bond dissociation energy 460kJ/mol)

	energy 410kJ/mol)	energy 397kJ/mol)	energy 389kJ/mol)	
n-octane	6 (33.3% of the total C-H bonds)	12 (66.7% of the total C-H bonds)	0	0
iso-octane	15 (83.3% of the total C-H bonds)	2 (11.3% of the total C-H bonds)	1 (5.3% of the total C-H bonds)	0
1-octene	3 (18.75% of the total C-H bonds)	10 (62.5% of the total C-H bonds)	0	3 (18.75% of the total C-H bonds)

The comparison between toluene and methylcyclohexane is straight forward. Since the dehydrogenation product of toluene is methylcyclohexane, and this reaction is highly endothermic (The heat of reaction is around 205kJ/mol [161]). Toluene is clearly harder to decompose. As we can see from Figure 1(b), not only the onset temperature of hydrogen generation for toluene is higher than that of methylcyclohexane, but also the hydrogen yield from toluene is lower than that of methylcyclohexan at all decomposition temperatures.

The order of overall hydrogen yield from thermal decomposition of different fuels follows: n-octane > methylcyclohexane > iso-octane > 1-octene > toluene. As a tentative explanation, the observed hydrogen yield order is compared with the fuel cetane number which characterizes the fuel ignition delay property. Table 5.3 lists the

cetane numbers for fuels investigated in this study. As we can see from the table, except for 1-octene, the larger the cetane number, the higher the hydrogen yields from thermal decomposition. The cetane number characterizes the ease of ignition for a given fuel.

Table 5.3. Fuel cetane number

Fuels	Fuel Cetane Number*
n-octane	63.8, 64.4, 65
Methylcyclohexane	20, 23
iso-octane	12, 14, 17.5
Toluene	5, 9, 18.3
1-octene	40.5, 41

* The different values of fuel cetane number are obtained by using different methods.

5.3.2 Gaseous Products from Thermal Decomposition of Liquid Fuels

Mass spectrums of thermal decomposition product were taken at each reaction temperature using the quadruple mass analyzer. The common decomposition products for all the fuels were hydrogen, toluene, benzene, and methane. For n-octane, the product also contained C2 and C3 olefins; for iso-octane, the product contained C2-C6 olefins; for 1-octene, the product had C2-C3 olefins and alkynes; for methylcyclohexane, the product had C2-C3 olefins and paraffins and for toluene, the product contained C2-C6 paraffins. The similarity in gaseous products from different

fuels suggests that at high temperatures, it is the stability of each gas species that determines the product distribution. Figure 5.2(a) and 5.2(b) shows species concentration from n-octane decomposition as a function of decomposition temperature. From these plots, we can obtain some qualitative insights into the mechanism of fuel decomposition.

As we can see from the plot, hydrogen partial pressure starts to increase at ~600^{o}C accompanying by the increases in concentration of toluene, methane, ethylene and other gas species. The cracking of the fuel molecule is believed to be initiated by carbon-carbon bond homolysis reaction with the formation of two radicals. The intermediate radicals may undergo carbon-carbon bond homolysis (β-scission) to form olefins (ethylene and propene) and a new radical [166, 167]. A stepwise dehydrocyclization with gradual loss of hydrogen to form a conjugated triene followed by ring closure and further dehydrogenation may account for aromatics formation [166]. Therefore, toluene and benzene are produced from their cycloalkane precursors. Studies have shown that the conversion efficiency for preparing toluene from its precursor is nearly 100%, while for benzene this efficiency is lower [166]. At higher temperatures, toluene hydrodealkylation reaction converts toluene to benzene. As Figure 2(b) shows, toluene concentration peaks at 750^{o}C, while benzene concentration peaks at 900^{o}C. At even higher temperatures, benzene decomposition reaction takes over the benzene formation reaction. Methane due to its high stability peaks at 900^{o}C followed by ethylene at 750^{o}C, and propene peaks at 600^{o}C. The decrease in temperature for the peak concentration from methane to ethylene reflects

the decrease in thermal stability also reflects the hierarchy of decomposition from larger to smaller molecules.

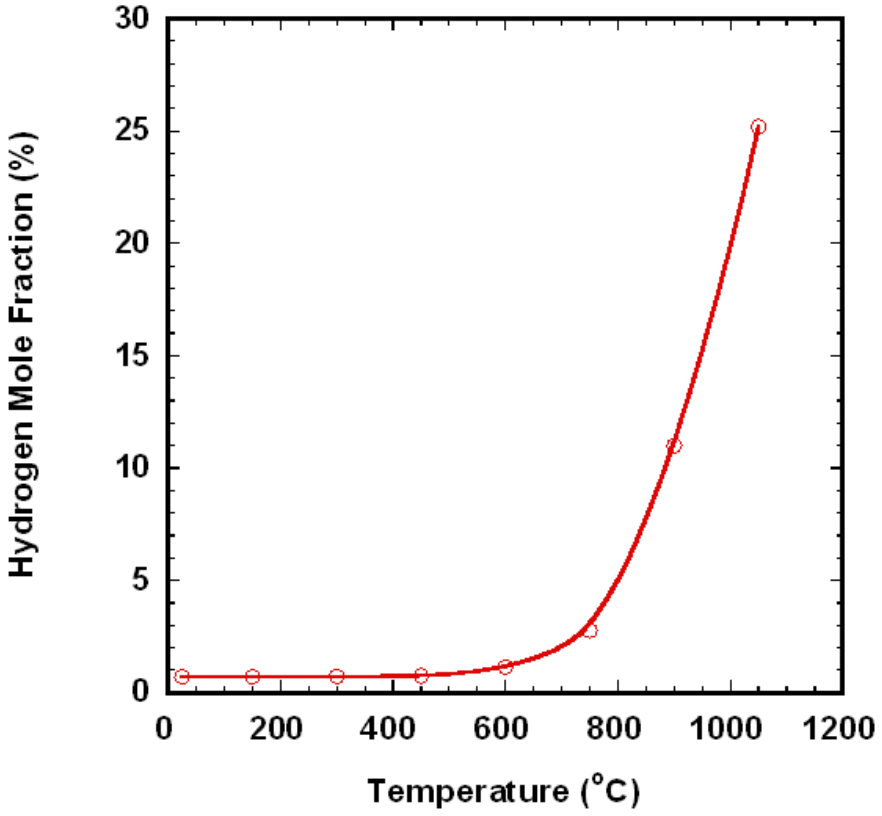

(a)

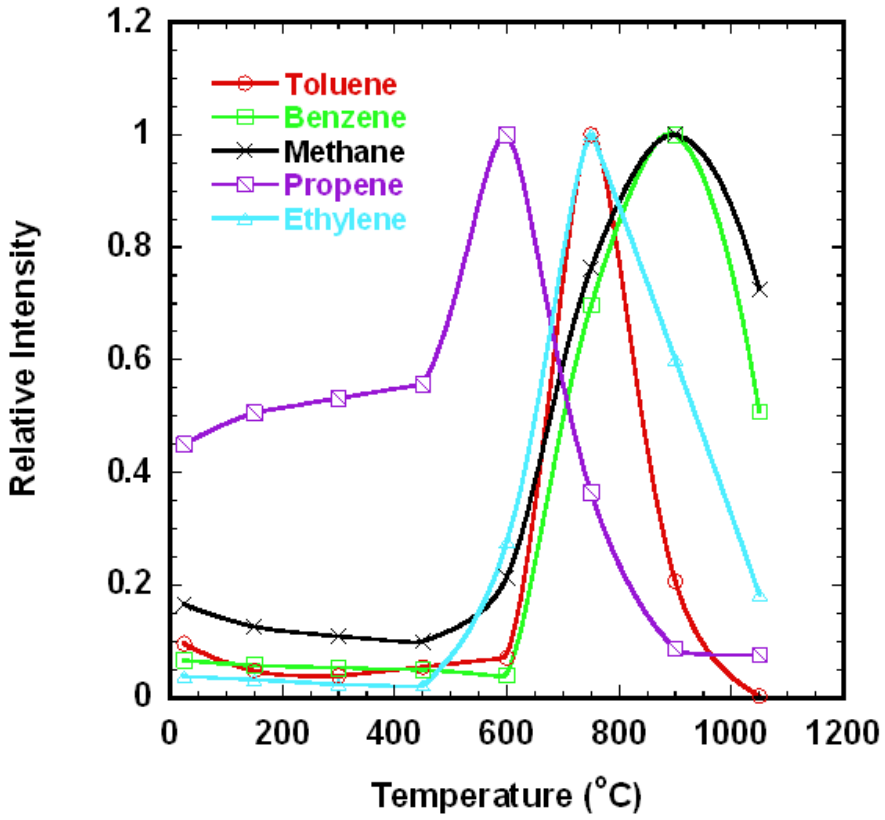

(b)

Figure 5.2: Product concentration from n-octane decomposition as a function of decomposition temperature (a) hydrogen mole fraction (b) relative intensities for other gas species

5.3.3 Catalytic Decomposition of Liquid Fuels

Metal atoms are believed to have an impact on the activation of carbon-hydrogen and carbon-carbon bonds in hydrocarbons. Reactions initialed by addition of metal atoms across a C-H or C-C bond, results in loss of molecular hydrogen and small alkanes to yield metal ion–olefin complexes. Transition metals are shown to have

higher potential in catalyzing this reaction. In our experiment, we produced catalytic iron nanoparticles on-the-fly by thermally cracking the iron pentacarbonyl precursor as discussed in the experimental section. TEM image of the as-produced iron particles are presented in Figure 5.3(a) and shows that the primary particles are 10-20nm in diameter, with electron diffraction confirming elemental iron. The particle size distribution of the catalytic iron particles was measured using an SMPS (scanning mobility particle sizer) system and is presented in Figure 5.3(b). The results show that the aggregate sizes are quite large with a median diameter around 300nm. A large aggregate is actually beneficial in this case, since it should better represent large iron flakes that could be produced by mechanical milling methods if this approach were to be used in an industrial setting. Figure 5.4 compares the changes in reaction activation energy for toluene decomposition with and without iron catalysts.

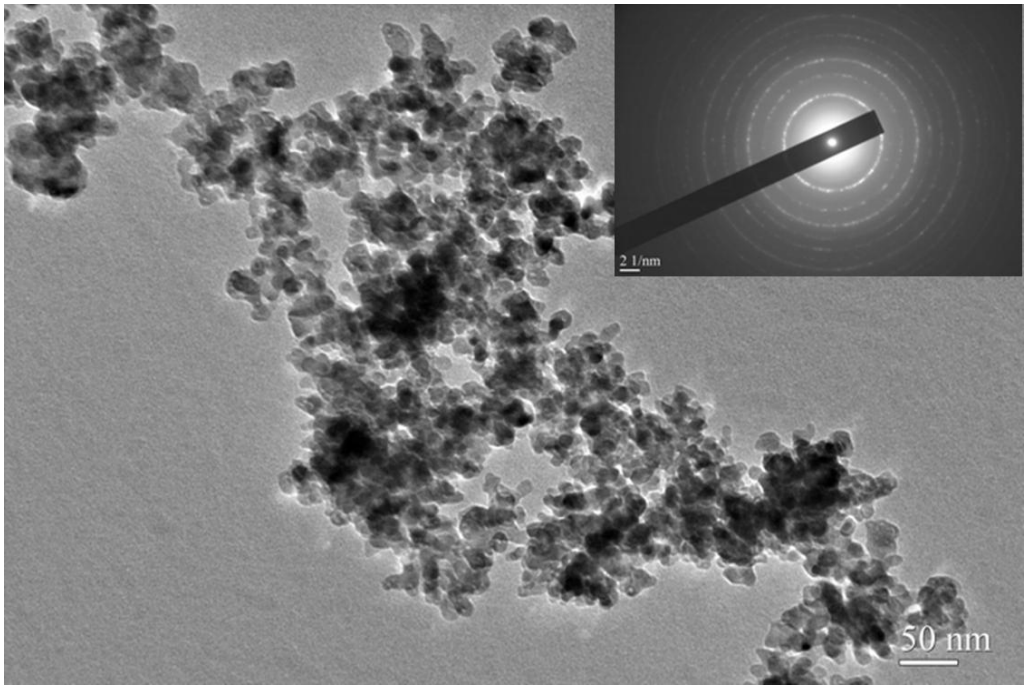

(a)

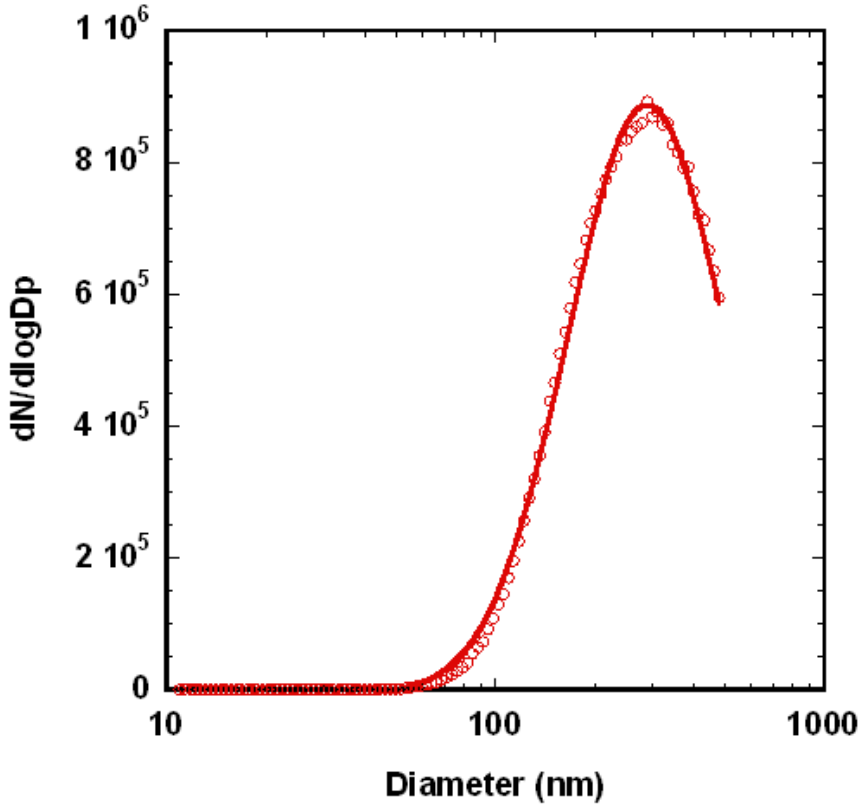

(b)

Figure 5.3: (a) TEM image of iron nanoparticle aggregates produced by decomposition of $Fe(CO)_5$ at 300°C. (b) Particle size distribution of iron nanoparticle aggregates measured by SMPS

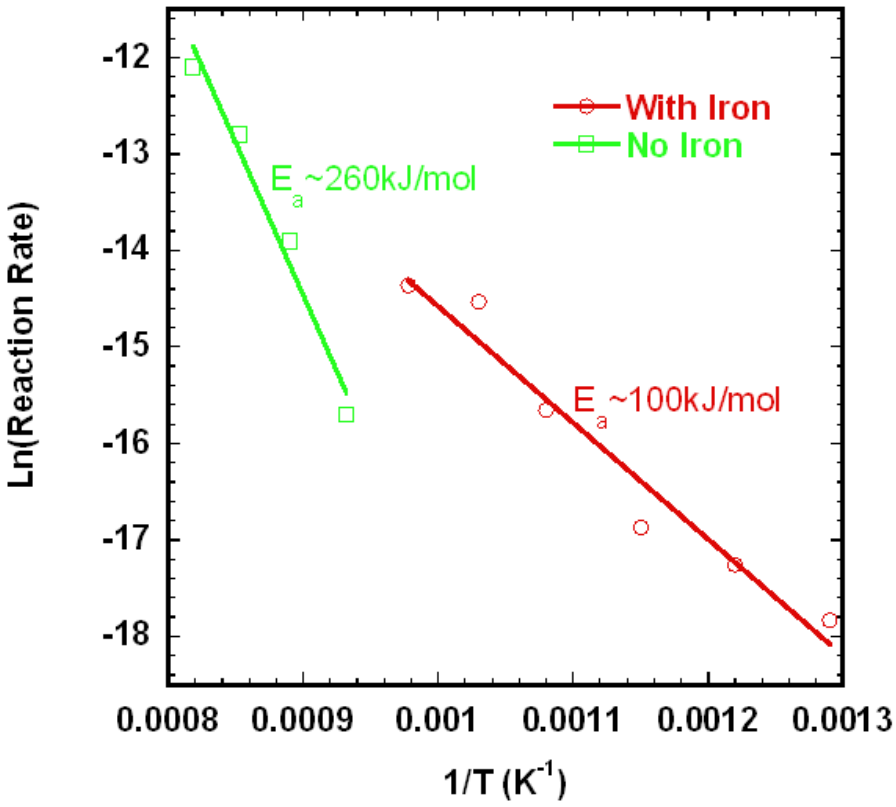

Figure 5.4: Activation energy for toluene decomposition with and without iron addition

The addition of iron catalyst can significantly lower the onset temperature of hydrogen generation (from ~ 800°C to ~ 600°C) and decreases the reaction activation energy. However, there is only very limited enhancement in hydrogen yield (less than 10% increase compared with thermal decomposition). Similar results have been obtained for other fuels. This behavior is well-known and resulted from the coking of catalyst particles since large quantity of solid carbon is produced. To prevent coking and promote the decomposition reaction, a small quantity of water vapor (as a weak oxidizer) was added (several thousand ppm) together with fuel and iron

pentacarbonyl during the toluene decomposition. The effect of water addition is presented in Figure 5.5.

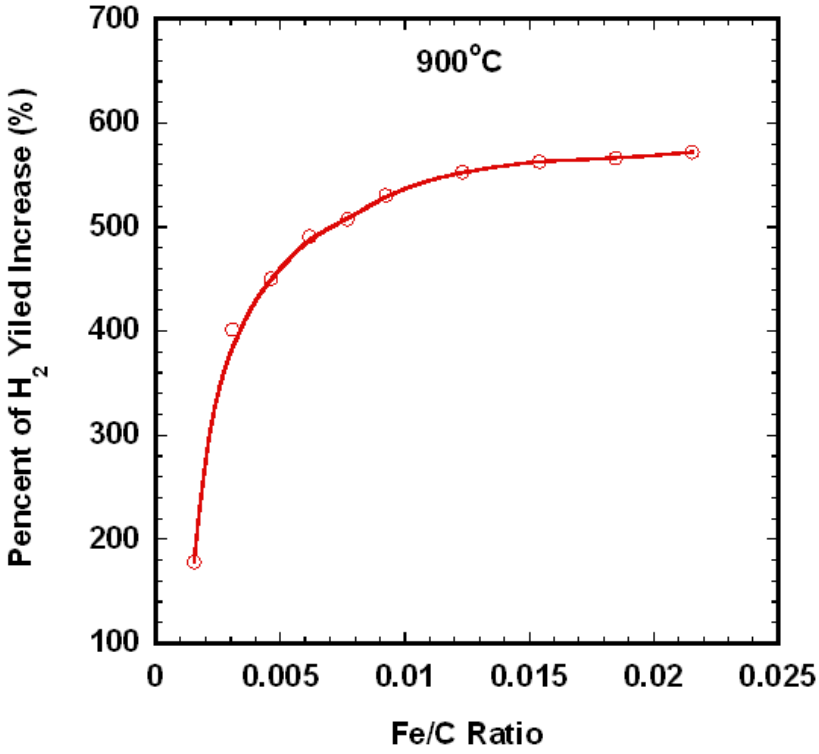

(a)

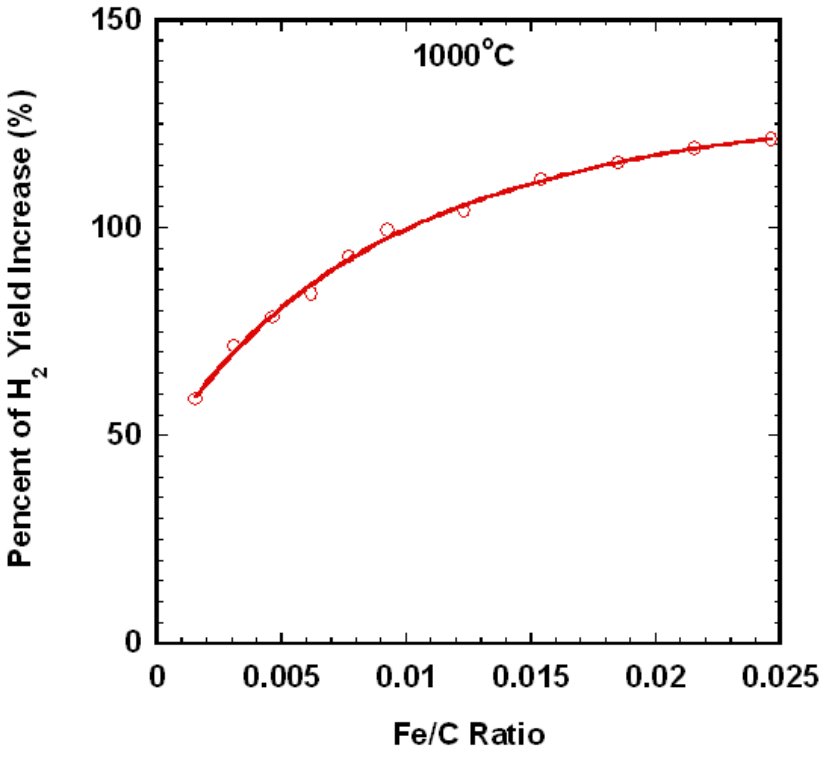
1000°C
Pencent of H2 Yield Increase (%)
150
100
50
0
0
0.005
0.01
0.015
0.02
0.025
Fe/C Ratio

(b)

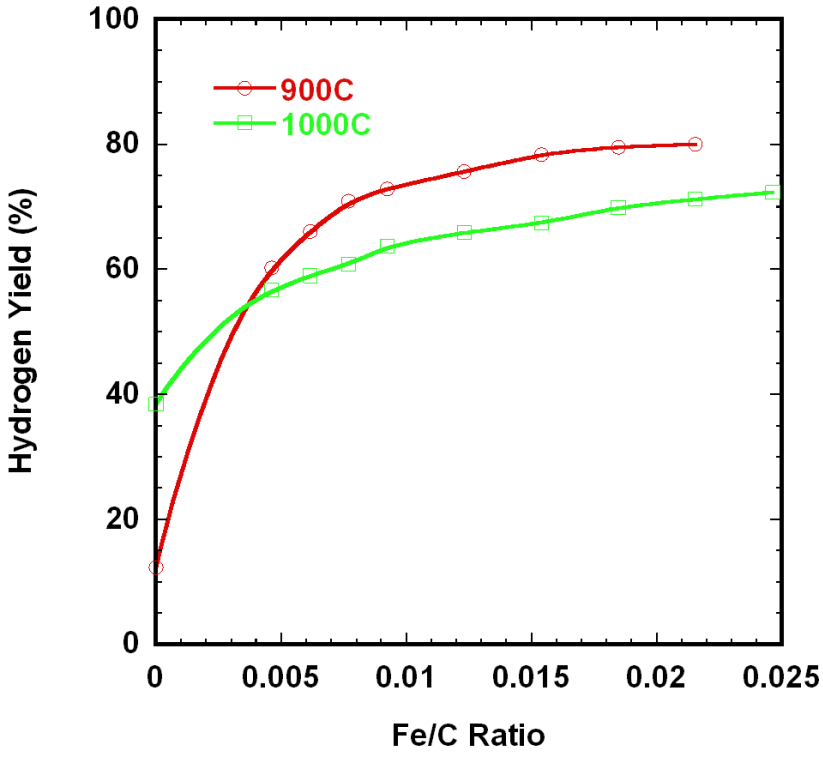
900C
1000C
Hydrogen Yield (%)
100
80
60
40
20
0
0
0.005
0.01
0.015
0.02
0.025
Fe/C Ratio

(c)

Figure 5.5: Adding water together with fuel and iron precursor greatly enhances the catalytic effect of iron nanoparticles in decomposition of toluene (a) percent of hydrogen yield increase at 900^{o}C (b) percent of hydrogen yield increase at 1000^{o}C (c) absolute hydrogen yield for catalytic toluene decomposition (the data points on the y-axis corresponding to toluene thermal decomposition without catalysts)

The addition of water significantly enhances the catalytic power of iron. As we increase the iron loading, the hydrogen yield also increases. An enhancement of 6 times in hydrogen yield was observed at 900^{o}C with Fe/C ratio of ~0.015. Further increase in iron loading does not increase the hydrogen yield. An interesting result is that the hydrogen yield increase at 1000^{o}C is not as high as that at 900^{o}C. A possible reason may be that at higher temperatures the thermal pyrolysis chemistry as well as possible coking of the catalyst competes with catalytic decomposition to minimize the gains of using a catalyst. To compare the catalytic effects, catalytic decomposition of different hydrocarbon fuels were investigated at 900^{o}C under the same experimental condition. The results are presented in Figure 5.6. As we can see from the plot, toluene shows the highest yield enhancement while iso-octane has the weakest enhancement. The general trend in hydrogen yield enhancement can be summarized as: the higher the non-catalytic thermal decomposition yield, the weaker the catalytic enhancement.

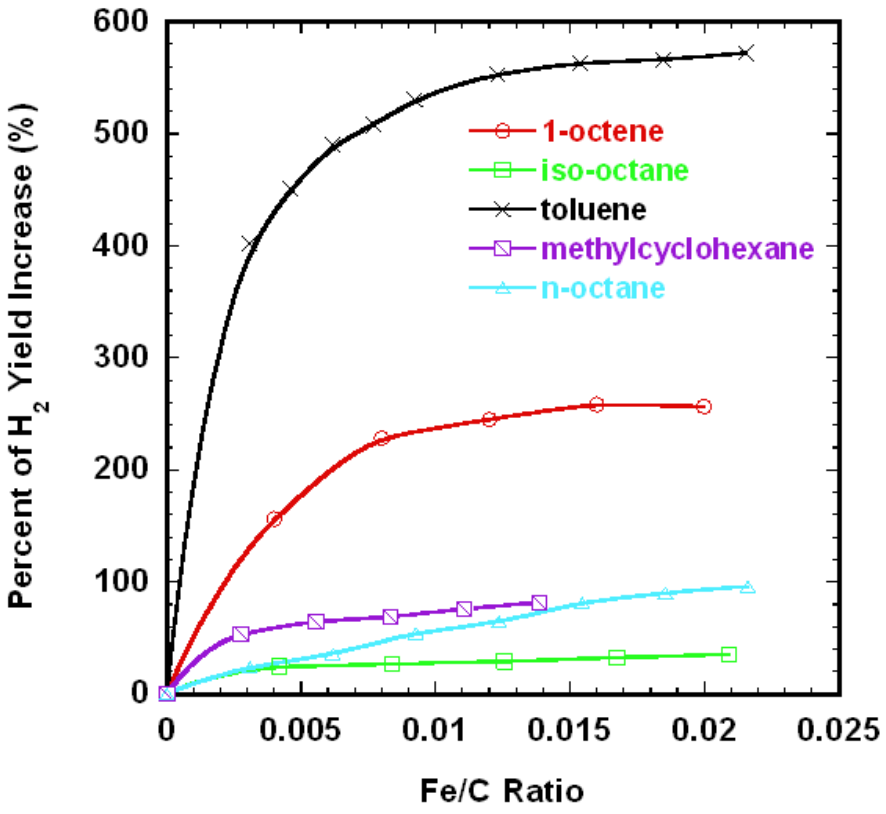

Figure 5.6: Comparison of percent increase of hydrogen yield with iron catalyst concentration for different fuels decomposition at 900^{o}C

5.3.4 Solid Carbon from Fuel Decomposition

One of the advantages of this process is that the byproduct of reaction ideally would be solid carbon and thus separation from hydrogen becomes, from a practical point of view, much simpler. To characterize the carbon particles produced from fuel decomposition, samples for electron-microscopic analysis were collected exiting the reactor by electrostatically precipitating the aerosol onto a TEM grid. Figure 5.7 presents the TEM images of carbon black particles collected from toluene

decomposition under various experimental conditions. As shown in Figure 5.7(a), the particulate product are quite large, about 1μm in size with primary particle diameters ~100-130nm. This is much larger than combustion generated carbon black or soot particles, where primarily particle sizes are nominally under 30nm. This difference reflects that fact that soot nominally experiences a much higher temperature and thus greater dehydrogenation. In turn, the more graphitic like the particle, the less they sinter, and thus the smaller the resulting primary particles. Figure 5.7(b) and 5.7(c) show the particle morphology resulting from toluene decomposition at 1000^{o}C with the addition of iron catalyst only. The darker area within a particle aggregate is iron, while the lighter-colored area is determined to be carbon. A high-resolution image (Figure 5.7(c)) shows the crystalline structure of the carbon materials. As we co-inject water vapor together with iron catalysts, hollow carbon particles were observed (shown in Figure 5.7(d)) as a result of partial oxidation of carbon particles by water vapor. The formation of hollow carbon particles also verifies that water vapor as a weak oxidizer, has an effect of carbon removal and recovering the iron catalysts. For the catalytic decomposition studies, in addition to carbon black particles in the aerosol form, a layer of mirror quality highly-reflective thin film was also observed after one experimental run (~ 2 hours) in the central region of the reaction tube as shown in Figure 5.8(a). XRD analysis (Figure 5.8(b)) confirmed that graphite was the major component.

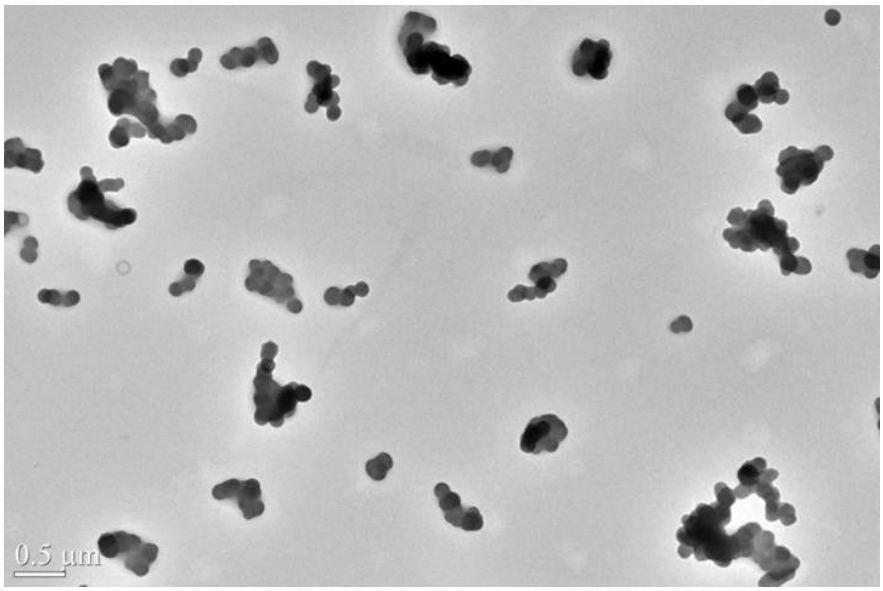

(a)

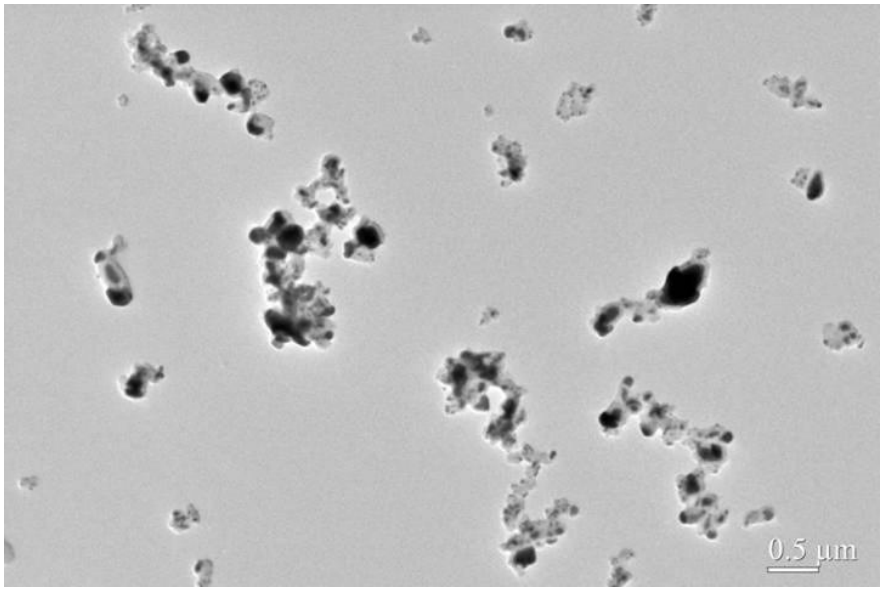

(b)

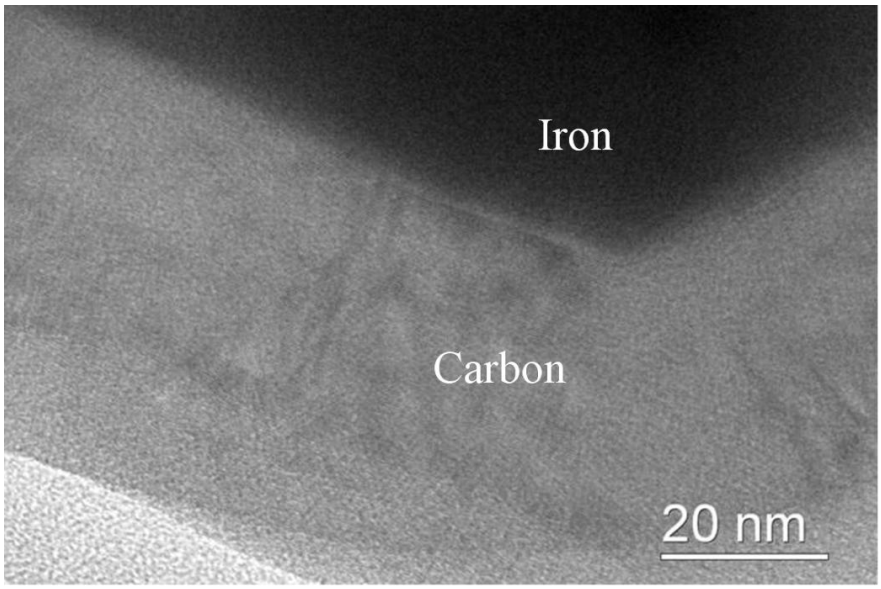

(c)

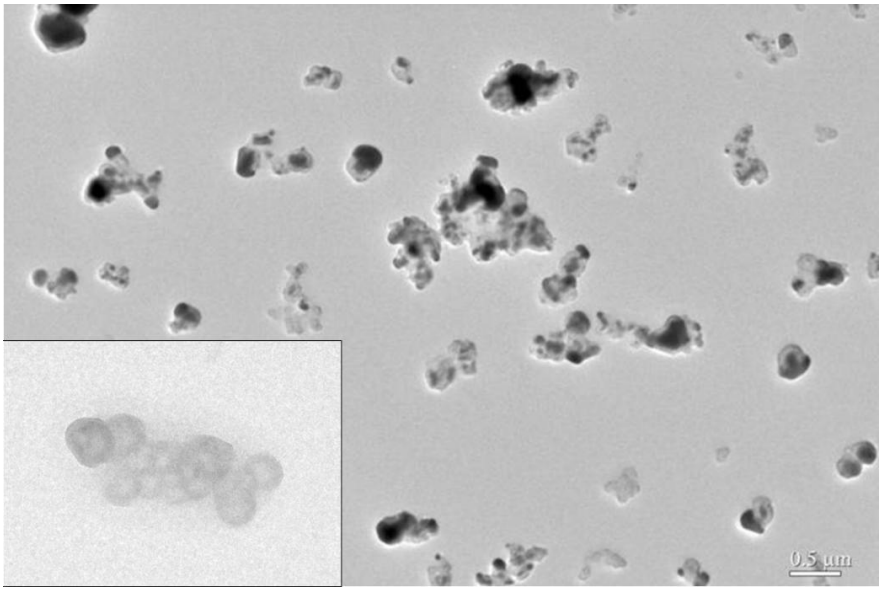

(d)

Figure 5.7: Carbon black particles from toluene decomposition under various conditions (a) decomposition at 1000^{o}C without catalysts, (b) and (c) decomposition at 1000^{o}C with addition of iron catalysts only, (d) decomposition at 1000^{o}C with addition of iron catalysts and water vapor.

(a)

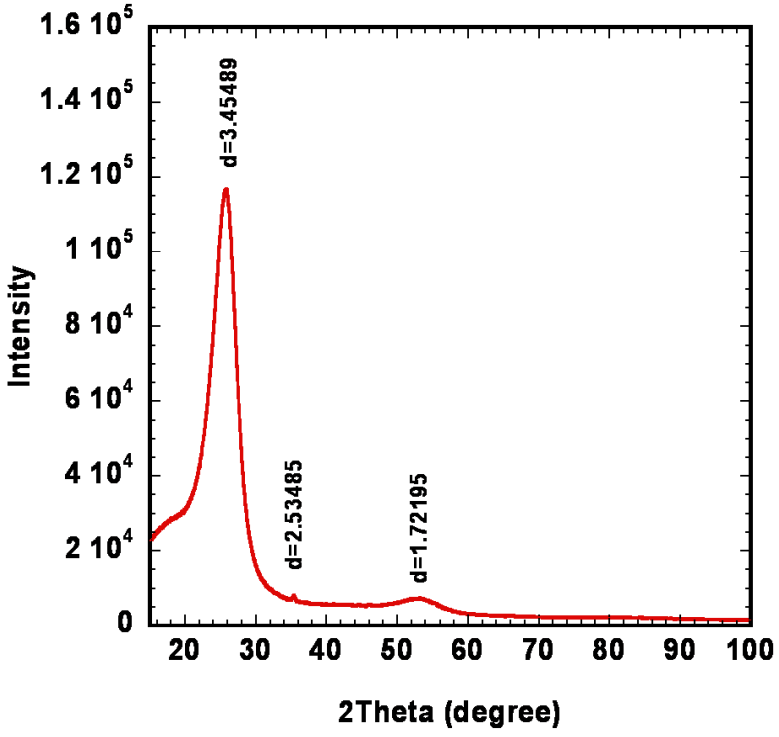
1.6 10^5
1.4 10^5
1.2 10^5
1 10^5
8 10^4
6 10^4
4 10^4
2 10^4
0
Intensity
d=3.45489
d=2.53485
d=1.72195
20
30
40
50
60
70
80
90
100
2Theta (degree)

(b)

Figure 5.8: Wall deposit (a) picture of thin films collected from the wall of the reaction tube (b) XRD result of the thin film collected from the central region of the reaction tube

5.4 Conclusion

The thermal and catalytic decomposition of liquid fuels were investigated in an aerosol reactor configuration to produce hydrogen and an easily separable solid carbonaceous aerosol product. The scheme is investigated as a possible route to solar driven hydrogen generation. To demonstrate this process scheme, iron was used as a catalytic material which was generated *in-situ* by thermal cracking of iron pentacarbonyl. The addition of iron catalyst was found to lower the onset temperature of fuel decomposition, and decrease the reaction activation energy. Co-injection of water vapor, which acts as a catalyst surface cleaning agent, significantly enhanced H_2 yield. The effect of fuel structure on the hydrogen yield from thermal decomposition follows the trend, alkanes > alkenes and cycloalkanes > aromatics and the overall order of hydrogen yield follows n-octane > methylcyclohexane > iso-octane > 1-octene > toluene. With the addition of iron catalyst, toluene has the highest yield enhancement by over a factor of six. The carbon black particles and graphite films were co-produced from the decomposition process.

Chapter 6: Ignition of Liquid Fuels Catalyzed by Unsupported Metal Nanoparticles in a Flow Reactor

6.1 Introduction

Combustion of fossil fuels provides the majority of the energy used today [168]. Conventionally, combustion process is initiated by an external ignition source. Modern internal combustion engines generally equipped with a sophisticated ignition system which ignites the fuel-oxidizer mixture and governs the performance of the engine. When designing such ignition systems, ignition properties of the fuel must be taken into account. However, the ignition properties vary very widely from fuel to fuel. Thus, the ignition systems can greatly add the complexity to the engine design and potentially lower the energy utilization efficiency. A promising route to improve fuel ignition properties is to use catalysts.

Catalysts can aid in the attainment of chemical equilibrium by providing an alternative reaction pathway with lower activation energy. Catalytic reactions play an important role in the energy, petroleum, and chemical industries. About 90% of the total chemical products are manufactured in catalytic processes. Catalysts are usually prepared in nanometer-sized particles so that total surface area exposed to the reactants is maximized. To preserve the high degree of dispersion and to provide a suitable form of packing for catalyst nanoparticles, supports on larger and inert materials such as alumina, silica, titania, carbon are usually needed. Most

investigations on catalytic reactions are done with such catalysis configurations. However, unsupported (free) nanoparticle catalysts can offer many advantages over traditional supported ones. First, investigations on free nanoparticles can eliminate the influence of the support materials and other extraneous factors. Second, the freshly generated free catalyst particles can readily mix with reacting gas stream and initiate the gas phase reactions downstream. Third, rapid advances in clusters and nanoparticle science provides better approaches of controlling particle size distribution, morphology, and surface properties in the aerosol phase. Furthermore, the development of on-line characterization tools offers new way to probe intrinsic nanoparticle reaction kinetics. Some pioneer works have been done on this area. For example, Glikin [169, 170] studied the oxidation of acetic acid over a free iron oxide catalyst. Weber [171, 172] investigated the catalytic activity of gasborne Ni nanoparticles for methanation reaction and concluded that the particle morphology could influence the catalytic performance.

Recently, Shimizu [173] et al. reported work of catalytic methane ignition over the surfaces of freely-suspended and in situ generated palladium nanoparticles. Compared with homogeneous ignition, the ignition catalyzed by free palladium particles had much lower ignition temperature (a reduction in ignition temperature of ~150K was observed) and shorter ignition delay. However, no significant particle size or structure changes were found below and above the ignition temperature. In a later work, Devener [174] and his colleagues employed various tools to characterize the composition, structure, and surface chemical state of the in-situ generated Pd/PdO

catalyst particles during the ignition process. Their results implied that particles must get oxidized before catalytic ignition can be expected.

Ignition is important with regard to exothermic decomposition. Wolfe [175] studied the catalytic effect of different metal surfaces for hydrazine decomposition and found that metals with incomplete d-orbitals had catalytic effect in hydrazine decomposition ignition. It is believed that bonds can form between the N atoms in hydrazine and the incomplete d-orbitals of the metal. This bonding can initiate hydrazine dissociation and subsequent decomposition and heat release. During the process, the catalytic surface will also rise in temperature. Transition metals are catalytically active for many reactions.

Aromatic compounds are important constituents of transportation fuels. Commercial gasoline, diesel, and jet fuels contain on average 25%, 33%, and 16% volume percentage of aromatics, respectively [176]. Of all aromatic compounds, toluene is the most significant component. Toluene has been proposed as component of many surrogate fuels for gasoline, diesel, and jet fuels [177-180]. Therefore, a reasonable volume of theoretically and experimental works has been devoted on this system. However, toluene exhibits poor ignition properties. In this work, in-situ generated unsupported (free) iron and nickel nanoparticles were used to catalyze the ignition of toluene. Those metal nanoparticles suspended in the gas mixture are expected to provide necessary surfaces to initiate gas-surface reactions which can result in a lower ignition temperature for toluene.

6.2 Experimental

The catalytic ignition of liquid fuels was performed in an aerosol reactor with a controlled gas flow system. The catalytic effects of three aerosol phase catalysts (Fe NPs, Ni NPs, and graphene sheet) were investigated in this study. A schematic of the experimental setup is presented in Figure 6.1. The gas mixtures were prepared by bubbling liquid fuel and then mixing the fuel vapor with the oxidizer (oxygen or air). The catalyst particles were generated in-situ and mixed with the fuel/oxidizer gas mixture before entering the reactor tube. The aerosol reactor consists of a 22 mm I.D. 25 mm O.D. quartz tube within a 30 cm heated length, and with a nominal residence time of ~1 min. In our experiment, the reactor temperatures were increased at a step of 150^{o}C. Steady states were achieved at each temperature. Between temperature steps, a heating rate of about 30^{o}C/min is used.

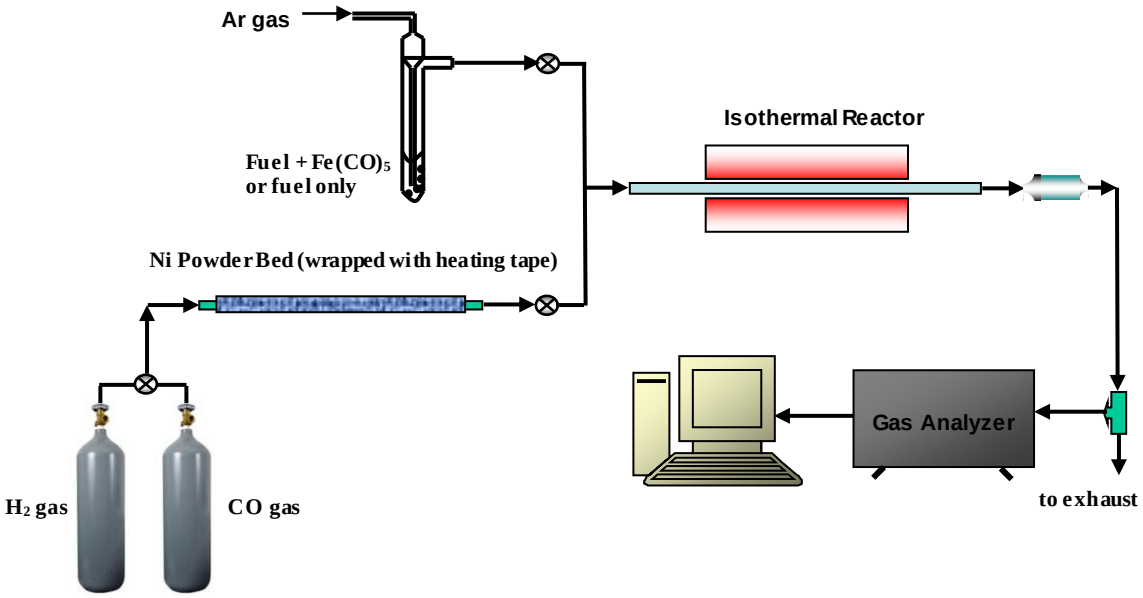

Figure 6.1 Schematic of the experiment setup for liquid fuel ignition

6.2.1 In-situ Generation of Iron Catalyst Particles

Iron catalyst particles were generated on-the-fly by thermally decomposition of the fuel-soluble iron pentacarbonyl. The iron carbonyl was directly mixed with the liquid fuel and then the mixture was bubbled and carried by Ar flow to the reactor. The vapor composition is determined by the molar ratio of the two components according to Raoult's law.

6.2.2 In-situ Generation of Nickel Catalyst Particles

The Ni nanoparticles were prepared by using gas-phase thermal pyrolysis of nickel tetracarbonyl. Because of the high toxicity of nickel carbonyl, it was generated in situ by flowing of a small amount of carbon monoxide through a nickel powder bed. Before each experiment, the nickel bed was heated to ~350 ℃ with a hydrogen flow for about 4 h to clean the surface of the nickel powder. After the hydrogen pretreatment, activated nickel powder is reacted with CO at 60^{o}C to generate $Ni(CO)_4$. The generated $Ni(CO)_4$ was mixed with a flow of Ar and passed to the cracking reactor held at ~450 ℃ to generate nickel particles. Due to the low activation energy of $Ni(CO)_4$ formation reaction, increases in Ni bed temperature has small effect the Ni particle concentration.

6.2.3 Product Characterization

The size distributions of catalyst particles were measured at the reactor exit using a scanning mobility particle sizer (TSI SMPS), which is composed of an electrostatic classifier (Model 3080) and a condensation particle counter (Model 3775). A flow rate of 0.3LPM of the diluted exhaust was sampled into the SMPS system.

The gaseous product was characterized by a mass spectrometer (Stanford Research UGA 300) which also monitored the hydrogen and argon partial pressures with time. The fuel ignition behavior was determined by monitoring the fuel, oxygen and gas products partial pressures. Argon was used as an inert internal standard and to determine the volume change of gaseous reactants and products during the reaction so as to assign concentrations. Samples for electron-microscopic analysis were collected

by electrostatically precipitating the aerosol onto a TEM grid using an electrostatic precipitator.

6.3 Results and Discussion

6.3.1 Iron Nanoparticles

Figure 6.2 shows a TEM image of Fe NPs collected at temperature 150^{o}C under oxygen free environment with 400microliters of $Fe(CO)_5$ dissolved in 15ml toluene. Under this condition, the atomic Fe to toluene molecule ratio is 0.02. As we can see from the image, the Fe NPs form aggregates which are composed of small primary particles of sizes between 20 and 30nm. Figure 6.3 presents the particle size distribution of iron aggregates generated at 150^{o}C with different iron carbonyl loadings. The size distributions were measured at the reactor exit using a scanning mobility particle sizer. As shown in the figure, all of the particle size distributions are roughly follow log-normal distribution. The Fe aggregate mobility diameters range from 120-170nm depending on the loading of the iron precursor. The particle concentration also increased with iron pentacarbonyl loading.

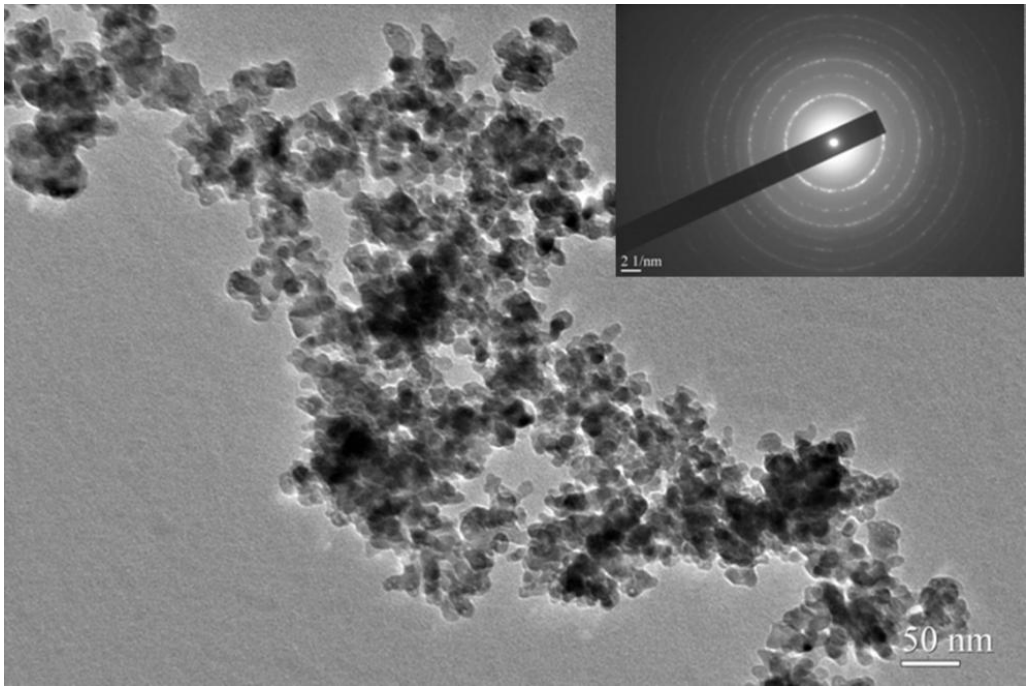

Figure 6.2 TEM image of Fe aggregates

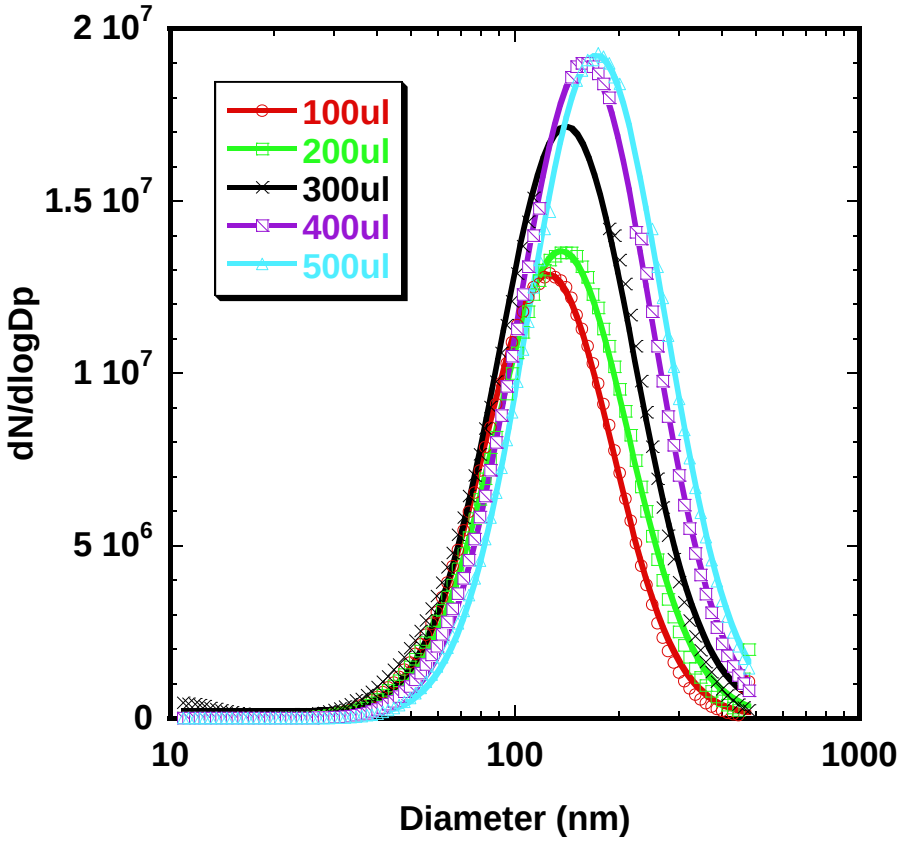

Figure 6.3 Particle size distribution of iron nanoparticle aggregates generated by iron carbonyl decomposition at 150^{o}C with different iron precursor concentrations

6.3.2 Nickel Nanoparticles

Figure 6.4 presents the particle size distribution of Ni NPs generated by nickel tetracarbonyl decomposition at 450^{o}C measured by SMPS system. As we can see from the graph, the particle size distribution peaks at about 61nm, which is much smaller than the size of Fe aggregates. This is consistent with the particle morphology observed from TEM analysis (Figure 6.5). As shown in the figure, Ni NPs are less

aggregated than Fe NPs. However, the primary Ni particle is about 50nm, which is larger than the Fe primary particles.

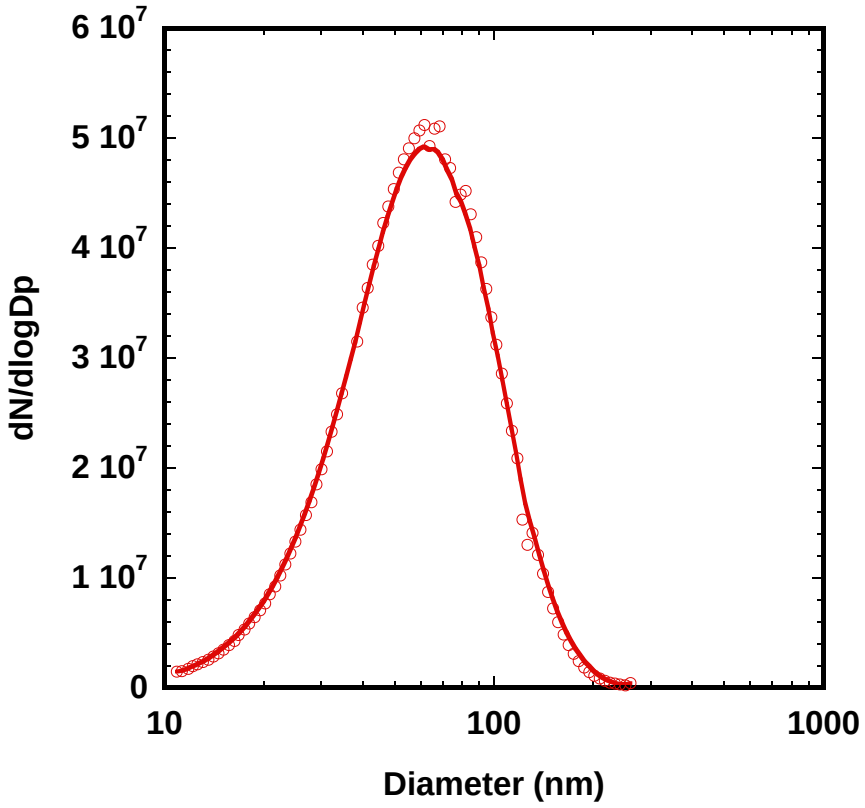

Figure 6.4 Particle size distribution of Ni NPs generated by nickel tetracarbonyl decomposition at 450^{o}C

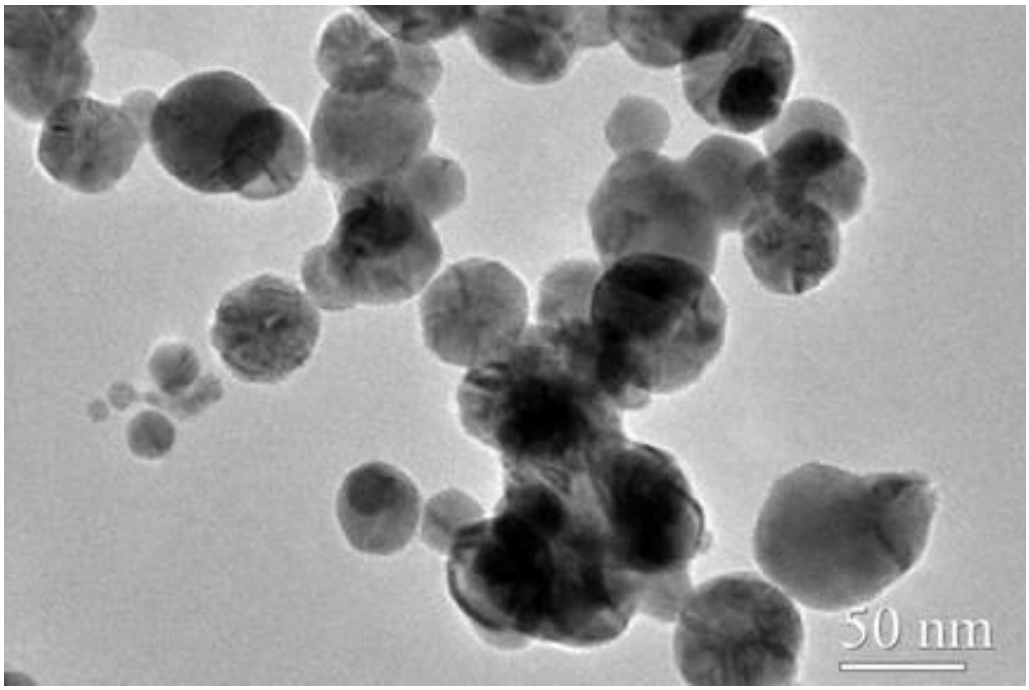

Figure 6.5 TEM images of Ni NPs

6.3.3 Liquid Fuel Ignition Catalyzed by Fe NPs

The toluene ignition experiments were conducted at various equivalence ratios. The results for equivalence ratios of 2.3, 1.0, and 0.4 are presented in Figure 6.6. The partial pressure of each gas species were monitored using a mass spectrometer (SRS UGA 300). A sudden increase in product CO_2 and CO together with the decrease of O_2 indicated an ignition event. As we can see from the plots, for equivalence of 2.3, the addition of iron catalyst decreased the toluene ignition temperature from ~ 750^{o}C to ~ 600^{o}C. However, at equivalence of 0.4, no significant changes in toluene ignition behavior were observed from the experiment. A reasonable explanation would be at low equivalence ratios, the iron nanoparticles were preferentially oxidized by O_2, thus

the catalytic effect is diminished. The same ignition behavior was also observed for octane fuel.

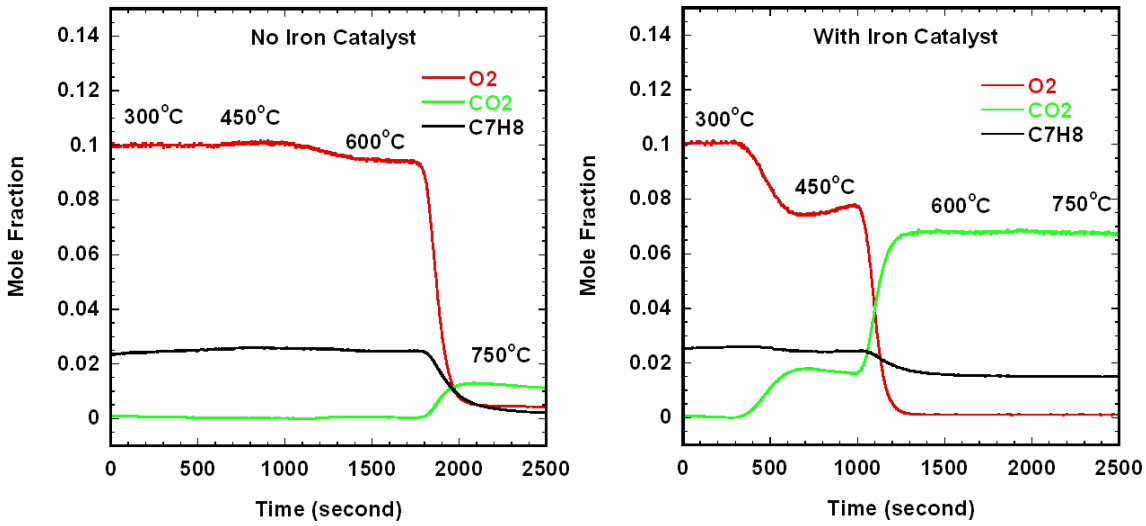

(a)

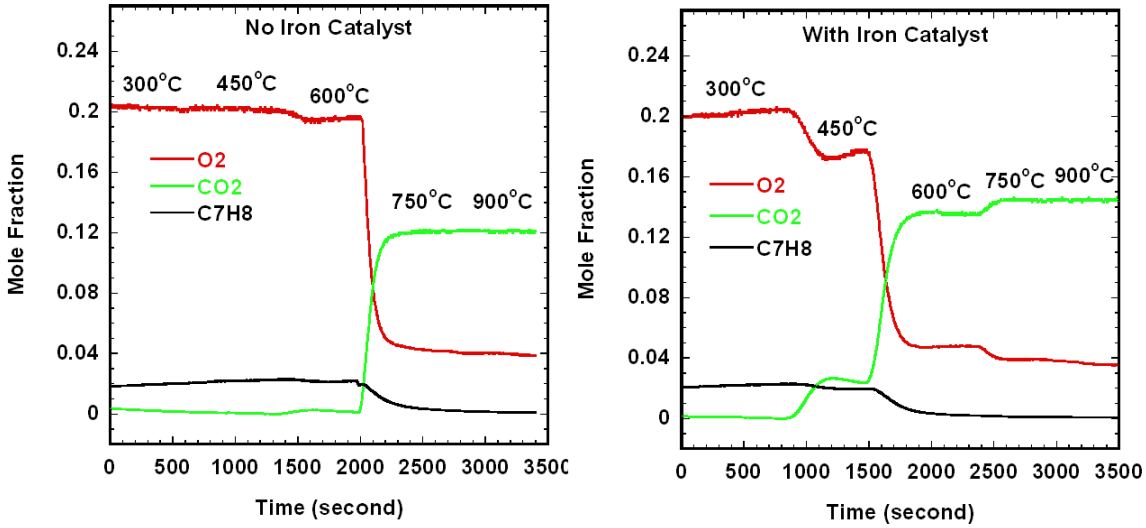

(b)

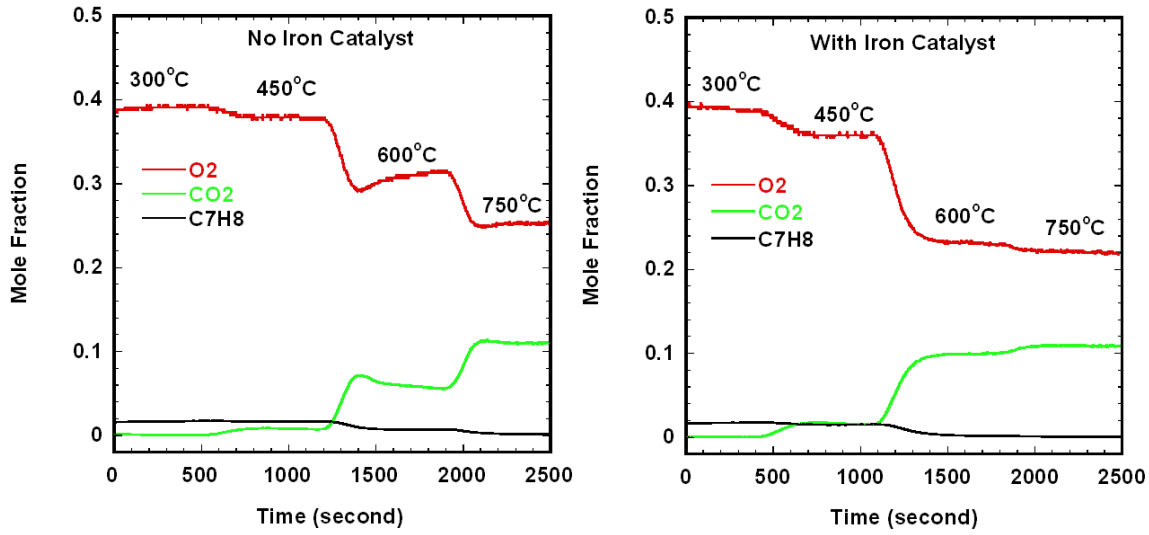

(c)

Figure 6.6 Partial pressures of fuel (toluene), oxidizer (O_2) and products CO and CO_2 for (a) fuel/oxidizer equivalence ratio of 2.3 (b) fuel/oxidizer equivalence ratio of 1.0 (c) fuel/oxidizer equivalence ratio of 0.4

In order to monitor the morphology evolution of the catalyst particles during the ignition event, samples for TEM analysis were collected at different reactor temperatures and under the oxidative condition with equivalence ratio of 1.0. The TEM images are presented in Figure 6.7. As shown in the figure, the particles at 300°C (Figure 6.7) exhibit a flower-shaped morphology with small oxide branches growing from each primary particle, which indicates partial oxidation of the Fe particles. Similar morphology was observed at 450°C. As the reactor temperature increased to 600°C (the ignition temperature from Figure 6.6(b)), particle sintering can be observed. The partially melted particle surface suggests that the local particle temperature may have been high due to local heating from exothermic reaction since

the bulk melting temperature of iron is above 1500°C. At the reactor temperature increased to 750°C, more sintered particle shape was observed.

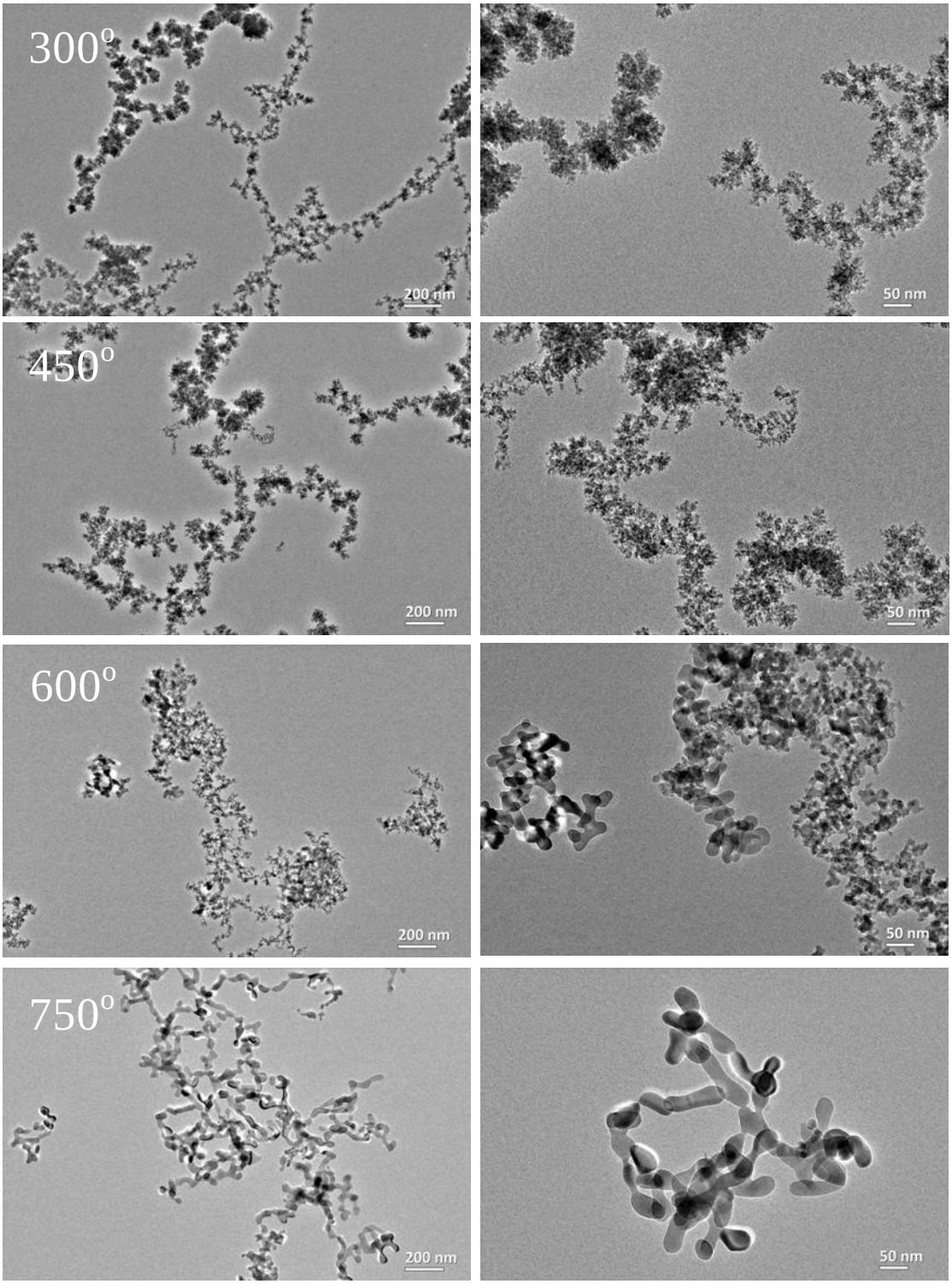

Figure 6.7 TEM images of Fe NPs at different reactor temperatures

A series of particle size distribution of catalyst Fe particles were also measured at the exit of the reactor under different reactor temperatures. The equivalence ratio was kept at 1.0 during the measurement. The results are presented in Figure 6.8. As can be observed from the figure, a large increase in aggregate size occurs at 300^{o}C with the particle mobility size almost doubling from that at 150^{o}C. The large size increase is due to more complete iron carbonyl decomposition and Fe particle partial oxidation at 300^{o}C. This is consistent with the oxygen concentration decrease at 300^{o}C. Further increase in the reactor temperature leads to slightly smaller particle peak size accompanied by lower particle concentrations. The smaller particle size at higher temperature is consistent with the sintering of particles. While a lower particle concentration is due to the increased diffusion particle loss at high temperatures.

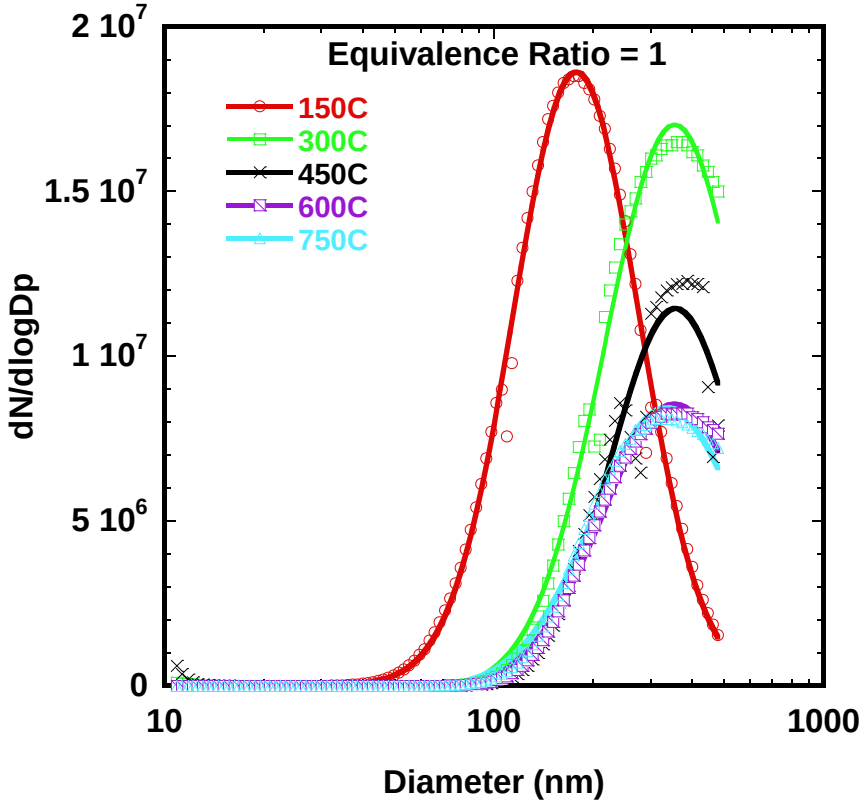

Figure 6.8 PSD of Fe NPs at different temperatures

6.3.4 Liquid Fuel Ignition Catalyzed by Ni NPs

The experiments of toluene ignition catalyzed by Ni NPs were carried out under various equivalence ratios. Since Ni NPs were generated by flowing CO through Ni powder bed in the catalytic ignition experiment, a small CO flow was also added in the non-catalytic experiment such that the total flow rate was the same for both cases. Figure 8 shows the comparable results for toluene ignition with equivalence ratio of 4.6. Two observations can be made from the results. First, adding Ni NPs lowers the ignition temperature of toluene by about 150^{o}C. Second, the

product CO in the non-catalytic case converted to more CO_2 in the catalytic experiment. This is similar in the Fe catalytic experiment. The ignition experiments were also carried out at equivalence ratios at 2.3, 1.0, 0.8 (?). As we decrease the equivalence ratios, the auto-ignition temperature also decreases. At equivalence ratio of 1.0, flash was observed at temperatures between 600-650^{o}C, indicating violent combustion occurring at this condition. At low equivalence ratios, adding Ni NP catalysts did not change the ignition behavior of the fuel. This trend is the same as that observed in toluene ignition experiments catalyzed by Fe NPs.

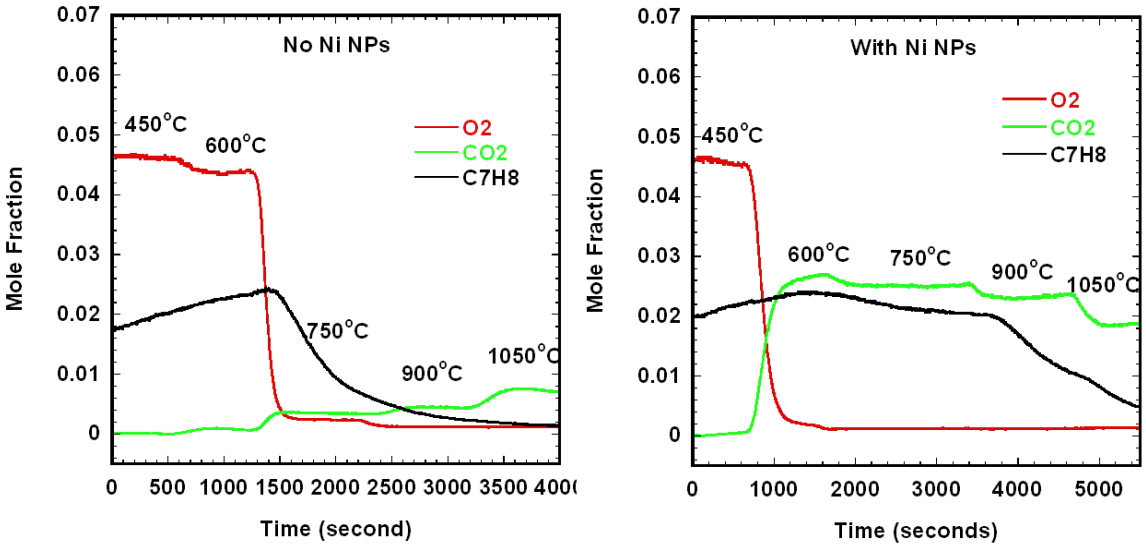

Figure 6.9 Toluene ignition catalyzed by Ni NPs

6.3.5 Mechanism of Catalytic Ignition

In order to reveal the effect of nanoparticles in toluene ignition, full mass spectrums of the reaction products were collected at each reaction temperature. The major detectable reaction products were hydrogen, carbon dioxide, carbon monoxide,

methane, ethylene, acetylene, and benzene. The concentration variations with temperature for selected reactant and products are presented in Figure 6.10. For comparison, the catalytic concentration and non-catalytic concentration are plotted in the same graph. Several trends can be observed from the plots. With the addition of iron catalysts, the oxygen concentration starts to decrease at a much lower temperature than the non-catalytic case. Correspondingly, the product carbon dioxide concentration starts to increase at a lower temperature and saturated at about 600^{o}C. The saturation concentration of carbon dioxide in the catalytic case is also much higher. The overall methane concentration is higher in the non-catalytic case. Hydrogen was detected at 600^{o}C in the catalytic case, while in the non-catalytic case, hydrogen was detected at 750^{o}C.

The detailed toluene oxidation mechanism is very complex. It is generally believed that the initiation of oxidation of toluene is the pyrolytic cleavage of a hydrogen atom from the methyl side chain at high temperatures, and the O_2 abstraction of an H from the side chain at low temperatures [175]. The products of the initiation step then undergo a series of chemical transformations and form smaller intermediate molecules. Carbon monoxide and water can be produced during the transformations. Finally, the smaller intermediate products undergo their own oxidation processes and generate carbon dioxide and water. With the general mechanism of toluene oxidation, we can summarize the effects of catalysts in toluene ignition. As we can see from Figure 6.10, with the addition of Fe catalysts, oxygen starts to decrease as low as 300^{o}C, which is consistent with the oxidation of iron nanoparticles. No carbon dioxide increase was detected. Further decrease in oxygen

concentration occurs at 450^{o}C which corresponds to the attack of toluene by oxygen molecules. At this temperature, a small amount of carbon dioxide is detected as the reaction product. As the temperature increases to 600^{o}C, hydrogen is detected as the results of high-temperature toluene pyrolysis. The generated H atoms initiate H_2-O_2 radical pool which leads to the radical attack of toluene molecules. As more and more toluene molecules start to break down and react with oxygen, the ignition occurs. A huge amount of carbon dioxide is produced by conversion of carbon monoxide and by oxidation of smaller intermediate molecules such as methane, ethylene, and acetylene. A much higher carbon dioxide concentration is observed in the catalytic case, which suggests a thorough oxidation reaction. Figure 6.10 shows a lower methane concentration at high temperatures in the catalytic ignition. The detected ethylene and acetylene concentrations (not shown) were also lower in the catalytic case. In summary, the addition of iron nanoparticles has three effects in catalyzing toluene ignition. First, iron nanoparticles can promote oxygen attack of toluene molecules at low temperatures. Second, iron nanoparticles promote the fuel pyrolysis at higher temperatures. The similar trend was also observed in our previous studies in catalytic fuel decomposition [181]. And third, the addition of iron particles accelerates the oxidation of smaller molecules.

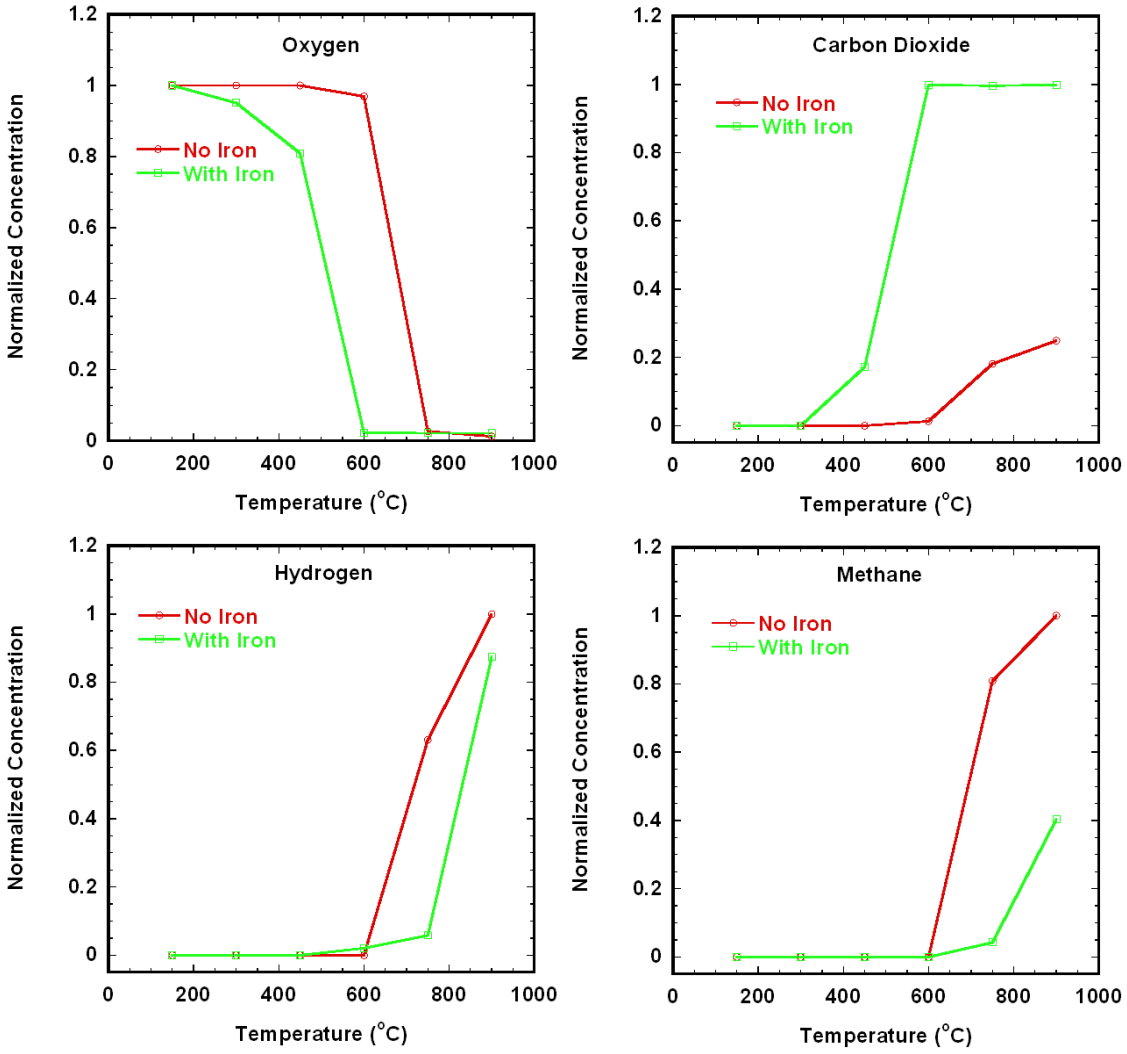

Figure 6.10 Concentrations of selected gas species

6.4 Conclusion

In summary, catalytic ignition of liquid fuels (toluene, octane) over the surfaces of in situ generated free metal (Fe, Ni) nanoparticles was performed experimentally in an aerosol reactor. The Fe nanoparticles were generated by decomposition of the fuel-soluble precursor iron pentacarbonyl ($Fe(CO)_5$). The Ni nanoparticles were prepared

by using gas-phase thermal pyrolysis of nickel tetracarbonyl ($Ni(CO)_4$). The nanoparticles were suspended in Ar environment and injected into the aerosol reactor along with a fuel-oxygen mixture. Under the experimental conditions studied in this work, the catalytic effect is the most significant at high equivalence ratios. Compared with non-catalytic homogeneous ignition, the addition of Fe nanoparticles can lower the ignition temperature of toluene and octane by about 150^{o}C at equivalence ratio of 2.3. The size distributions of Fe nanoparticles was log-normal with a median diameter ranging from 120-170nm depending on the loading of the iron precursor. The size of Ni nanoparticles ranges from 60nm to 100nm.

Chapter 7: Synthesis of Hollow Black Carbon Nanoparticles by Controlled Oxidation

7.1 Introduction

There have been a number of studies concerning the structural changes of black carbon nanoparticles during oxidation. Ladd etc. al.[182] observed a hollow shell structure with acid oxidation of soot produced by thermal decomposition of gas or oil feedstock. Heckman[183] employed high temperature heat treatment to study the structural change of carbon black particles. After heat treatment at high temperatures, the particles exhibited a capsular structure analogous to the hollow structure. Vander Wal et al.[184] employed HRTEM technique to study the nanostructure of soot from diesel engine under different operating conditions. The HRTEM images revealed that a substantial fraction of primary particles show evidence of densification, with the ''hollow'' interior and highly crystalline outer shell. This is consistent with the densification being caused by a slow oxidation process under the conditions typical for diesel exhaust (temperature range of ~200–500^{o}C). Their results also show that the percentage of hollow particles varied between different soot samples and tentatively appeared to be related to the oxidation history of the sample.

Apart from air, various other oxidizers have been used for soot oxidation studies. These oxidizers vary in oxidative strength and can result in different soot structure changes. For example, water vapor has been used as an after-treatment agent in

carbon black industry. When this treatment is carried out at relatively low temperatures (300°C-500°C), extractable matters are primarily removed from the carbon black surface. At higher treatment temperatures (900°C-1100°C), porous carbon blacks are formed since steam preferentially attacks the less ordered regions of the carbon located inside the particles. If a considerable number of pores are formed, complete erosion of the inside of the particle is possible, leading to hollow particles.

Even though hollow soot nanostructures have often been found in diesel engine exhaust, detailed information on the oxidation condition for the formation of hollow black carbon particle is still lacking. To our knowledge, hollow black carbon nanostructure has not been previously produced in the gas phase in a controlled manner. In order to address these points, we developed a flow reactor system in which we can precisely control the oxidation conditions (such as temperature, residence time, choice of oxidizer) for synthesizing hollow black carbon nanostructures. The effect of different oxidizers on the structure of black carbon particles was investigated.

7.2 Experiment

The initial black carbon particles were generated by bubbling toluene vapor into a controlled pyrolysis environment. The pyrolysis reactor consists of a 22mm I.D. 25mm O.D. quartz tube within a 30 cm heated length, and with a nominal residence time of ~ 1 min. Various oxidizers (such as oxygen, water, carbon dioxide and acetone) and different oxidation conditions (such as temperature and residence time)

have been examined for the synthesis of hollow black carbon particles. The experiments of different oxidation conditions can be further grouped into two categories. In the first category, the oxidizer was added to the fuel before entering the reactor such that the black carbon particles were formed and partially oxidized in the presence of an oxidizer. In the second category, the black carbon particles were formed in the first reactor and then the oxidizer was added to the black carbon particles in the second reactor. A better control over the oxidation conditions can be achieved in this setup. Samples for electron microscopy analysis were collected under each condition by electrostatically precipitating the aerosol onto a TEM grid using an electrostatic precipitator.

7.3 Results and Discussion

Hollow Black Carbon Nanoparticles

The TEM images of hollow black carbon particles synthesized under various oxidation conditions are presented in Figure 7.1. Figure 7.1(a)-(c) show the hollow structures of black carbon particles synthesized by mixing the fuel and different oxidizers before entering the reactor at 900^{o}C. The oxidizers were water vapor, acetone and CO_2, respectively. Figure 7.1(d)-(f) are the TEM images of hollow black carbon synthesized using two-stage oxidation method in which black carbon particles generated by toluene pyrolysis at 900^{o}C in the first reactor underwent controlled

oxidation in the second furnace. As we can see from the TEM images, the black carbon particles generated by toluene pyrolysis are quite large in size with primary particles about 100nm. After oxidation, hollow shells are prevalent. For Figure 7.1(b), 7.1(d) and 7.1(e), the hollow black carbon particles are enclosed by large "droplets". The "droplets" are believed to form by condensation of hydrocarbon vapor onto the existing carbon particles when the aerosol exiting the furnace. EDS (Energy dispersive X-ray spectroscopy) analysis on these "droplets" confirmed that carbon was the major component of the structure. The "droplet" structure can be removed by increases in the furnace temperature. Two experiments were conducted to compare the morphologies of the hollow black carbon particles produced from the two-stage oxidation by water vapor. In the first experiment the oxidation furnace was kept at 600^{o}C, while in the second experiment, the oxidation temperature was set at 900^{o}C. The TEM images for these two conditions are presented in Figure 7.1(e) and 7.1(f), respectively. As can be seen from the figures, the major difference between the particle morphology is that the "droplet" structures prevail in the low temperature case but are absent in the high temperature case. To summarize the experiment results, mild oxidation conditions such as a weak oxidizer or low temperatures for stronger oxidizers are necessary for the formation of hollow black carbon structures. For example, in the two-stage oxidation by oxygen (Figure 7.1(d)), a relatively low oxidation temperature (500^{o}C) was chosen in the second furnace in order to create a mild oxidation environment. Our experiments showed that high temperatures (greater than 800^{o}C for a 60 seconds residence time) in an oxygen environment would lead to complete oxidation of the black carbon particles.

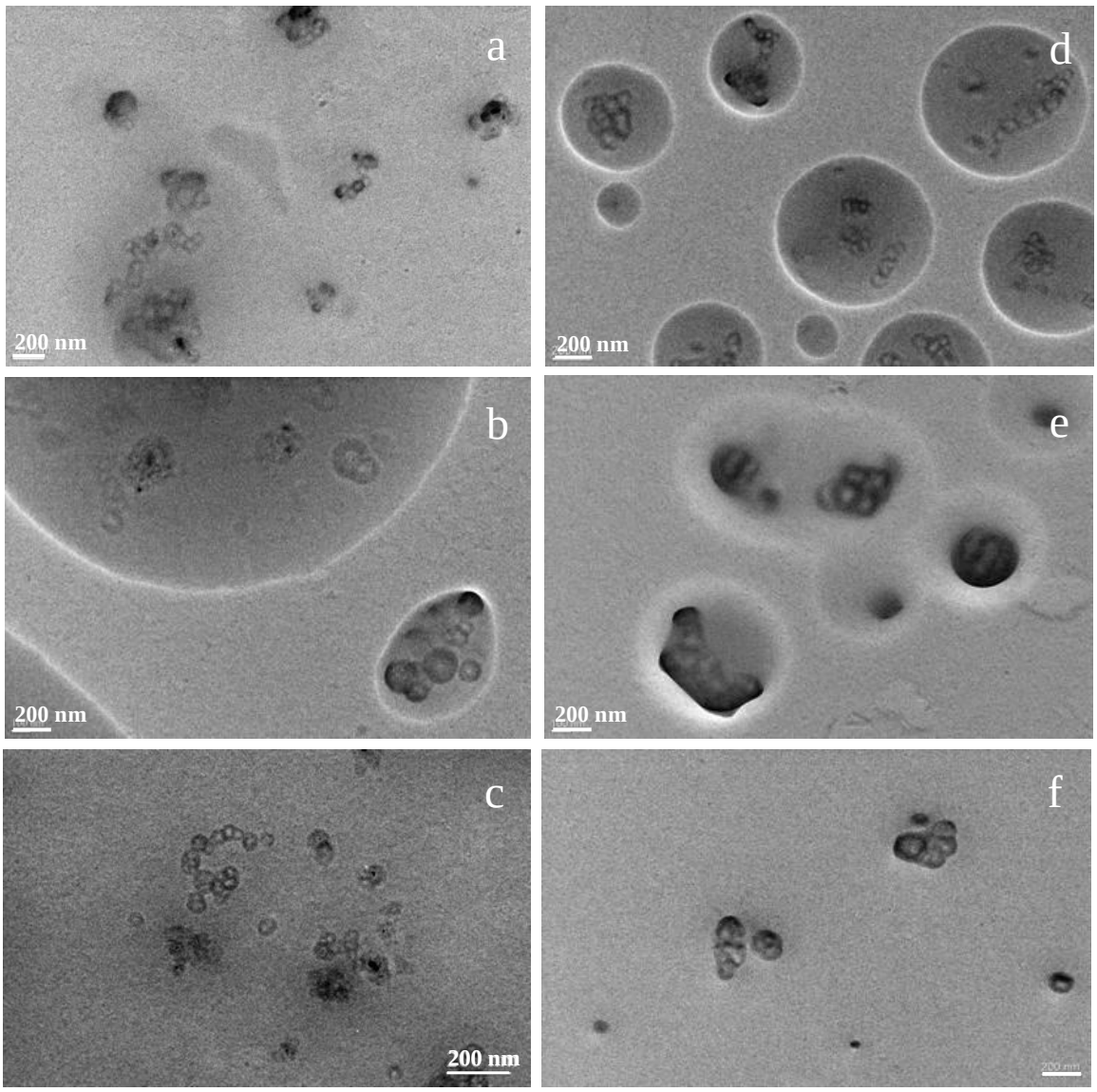

Figure 7.1. TEM images of hollow black carbon nanoparticles synthesized under different oxidation conditions. (a) Water vapor co-injected with fuel before entering the furnace at 900^{o}C. (b) Acetone vapor co-injected with fuel at 900^{o}C (c) CO_2 co-injected with fuel at 900^{o}C. (d) Two stage oxidation, black carbon generated at 900^{o}C followed by oxidation in the second furnace at 500^{o}C by oxygen. (e) Two stage oxidation, black carbon generated at 900^{o}C followed by oxidation in the second

furnace at 600^{o}C by water vapor. (f) Two stage oxidation, black carbon generated at 900^{o}C followed by oxidation in the second furnace at 900^{o}C by water vapor.

Determination of Elemental Carbon/Organic Carbon Concentrations

It is believed that a single black carbon primary particle has a more ordered graphitic layered structure at the surface of the particles, where the layer planes are aligned parallel to the surface, and diminishing graphitic order near the particle center [185]. With less structural order and potentially high H/C ratio, the inner core of the particle would preferentially oxidize before the outer, more graphitic particle perimeter. In our experiments, the hollow structures were consistently observed for black carbon particles generated by toluene pyrolysis at 900^{o}C. However, for black carbon particles generated by toluene pyrolysis at 1050^{o}C, no hollow structures were observed. This suggests that in addition to the oxidation conditions, the elemental carbon to organic carbon (EC/OC) ratio in the original black carbon particles plays a role in the formation of hollow structure. Changing the toluene pyrolysis temperatures, the elemental carbon concentration in the black carbon particles also changed.

In order to measure the elemental carbon (EC) and organic carbon (OC) on the samples, a Sunset Laboratories' Thermal Optical Carbon Analyzer employing the Thermal-Optical Transmission (TOT) method was used. The samples from the two pyrolysis temperatures were collected on a precleaned quartz-fiber filter positioned at the exit of the reactor. The TOT method pyrolyzes OC and employs laser light absorption to distinguish EC from the pyrolyzed OC. The details of the TOT analysis

and the schematic of the TOT instrument can be found in the references [186, 187]. The results of the TOT measurement are presented in Figure 7.2. The TOT measurement consists of three stages as can be seen from the thermogram in the figure. During the first stage that employs four heating steps in an inert (helium) atmosphere, thermally unstable OC is pyrolyzed, which causes the attenuation of laser light through the filter. Thermally stable OC is volatilized and removed from the filter at this stage and measured by flame ionization detection (FID). Later, in an oxidizing atmosphere of 1-2% in He, pyrolyzed OC as well as EC that is original on the sample is removed from the filter and captured by FID. With the removal of light-absorbing carbon, the laser signal retures to the point prior to the OC pyrolysis. All carbon measured beyond this point, the split point in the figure, is quantitatively assigned to EC, while all carbon measured prior to the point is quantitatively assigned to OC. The last stage of the measurement, which is in an oxidizing atmosphere in CH_4, used methane as a standard to determine the total carbon in the sample. Comparing the TOT results of the two samples, considerable more EC was found in the sample collected at 1050^{o}C, thus less OC in the sample. For the black carbon particles generated by toluene pyrolysis at 900^{o}C, the elemental carbon to the total carbon (EC/TC) ratio was determined to be 1.3%. For the black carbon particles generated by toluene pyrolysis at 1050^{o}C, the elemental carbon to the total carbon (EC/TC) ratio is about 21.3%.

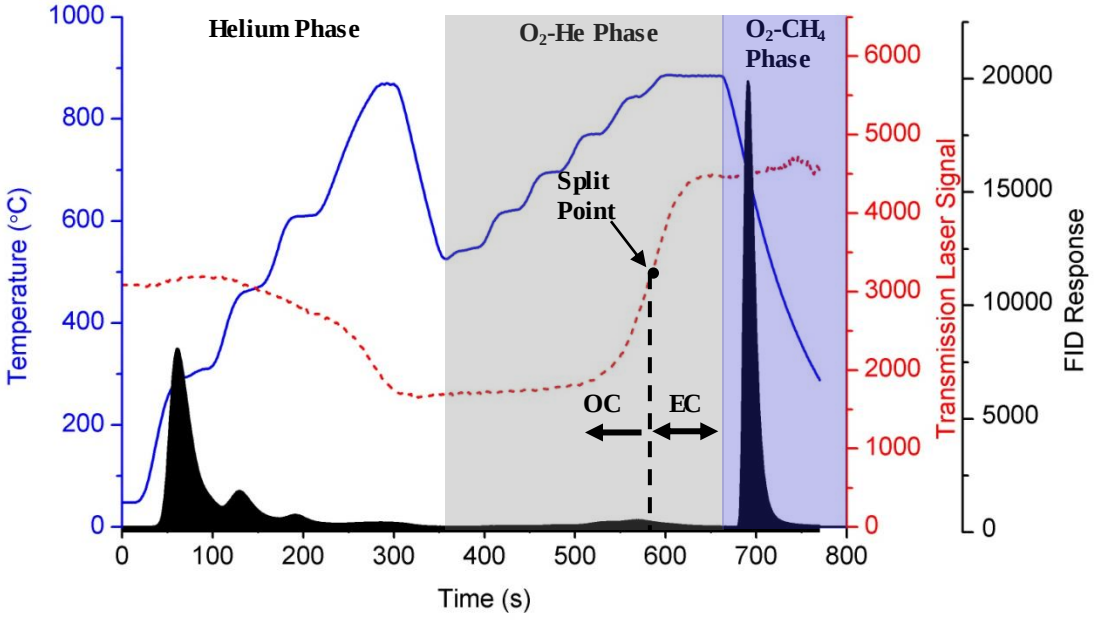
Helium Phase
O2-He Phase
O2-CH4 Phase
Split Point
OC
EC
Temperature (°C)
Transmission Laser Signal
FID Response
Time (s)

(a)

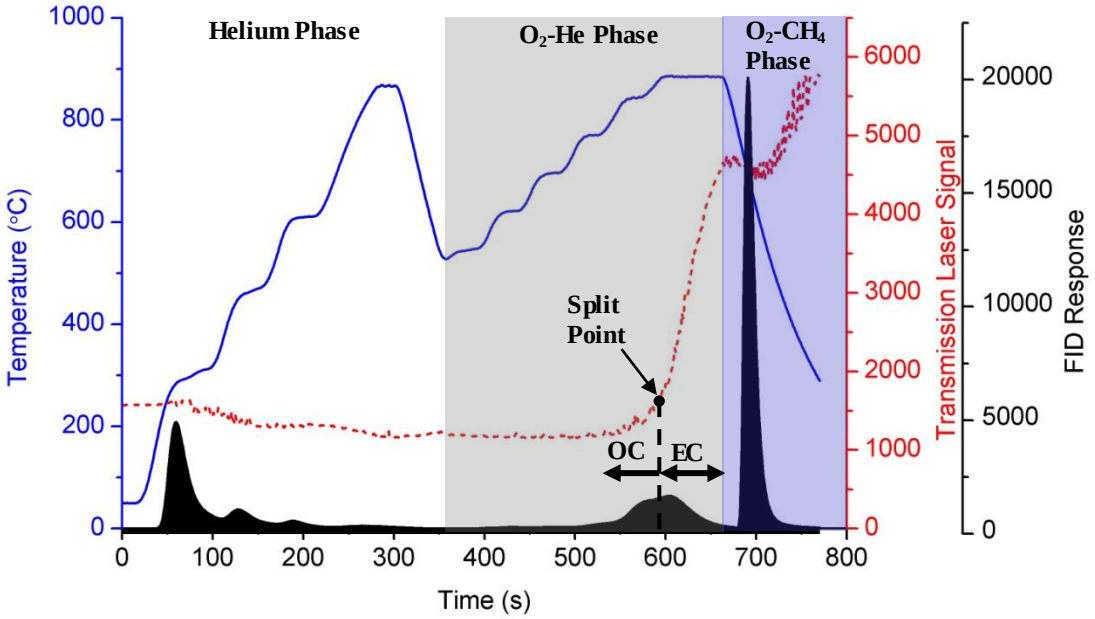
Helium Phase
O2-He Phase
O2-CH4 Phase
Split Point
OC
EC
Temperature (°C)
Transmission Laser Signal
FID Response
Time (s)

(b)

Figure 7.2 TOT instrument thermogram showing front over temperature profile, laser signal and FID response to thermally evolved particulate carbon. (a)toluene pyrolysis at 900^{o}C (b) toluene pyrolysis at 1050^{o}C

7.4 Conclusion

The synthesis of hollow black carbon nanoparticles in gas phase by controlled oxidation method was investigated. The formation of the hollow black carbon nanostructure is determined by the elemental carbon to organic carbon (EC/OC) ratio in the original particles and the oxidation conditions that the particles underwent. The effect of the oxidation conditions on the black carbon nanostructure was examined using electron microscopy. A thermal-optical method was used for measuring the elemental carbon concentration in the particles. For the black carbon particles generated by toluene pyrolysis at 900^{o}C, the elemental carbon to the total carbon (EC/TC) ratio was determined to be 1.3%, hollow structures were consistently observed using various oxidizers (O_2, CO_2, acetone and water) under mild oxidation conditions. For the black carbon particles generated by toluene pyrolysis at 1050^{o}C, the elemental carbon to the total carbon (EC/TC) ratio is about 21.3%, hollow structure was not observed.

Chapter 8: Conclusion and Future Work

The work discussed in this dissertation concentrates on using aerosol/nanoparticle techniques studying the reaction mechanism and kinetics of the chemical processes that can be potentially used for solar hydrogen generation. Basically, two types of solar thermochemical processes were investigated: metal/metal oxide solar thermochemical water splitting cycle and catalytic decomposition of liquid hydrocarbons. Nanostructured materials such as Zn nanocrystal, Fe, and Ni nanoparticle were generated, characterized, and used as either the reactants or the catalysts in those solar thermochemical processes. Their intrinsic reactivity was probed using tandem ion-mobility method. Metal/graphite core/shell nanostructure and hollow black carbon nanoparticles were synthesized as the solid products of the liquid fuel decomposition process. Their morphology and properties were determined and measured using electron microscopic analysis and thermal-optical transmission (TOT) method. The future extension of this work would involve further investigation of the mechanism, reaction pathway and kinetics of the novel solar thermochemical processes; further development and improvement of the on-line aerosol/nanoparticle measurement techniques; and synthesizing better, well-characterized nanomaterials for solar hydrogen generation. A more detailed discussion of the future improvements for each part of the work is listed below.

1. **Developing improved kinetics model for processing Zn nanocrystal oxidation data**

In Chapter 2, the Zn NC air oxidation study is presented. In the study, the size-classified substrate-free Zn NCs were explored for their oxidation kinetics using an in-flight tandem ion-mobility method. A shrinking core model is used to extract the size-dependent oxidation activation energies. Two reaction regimes were observed for Zn NC oxidation. The assumption behind the shrinking core model is that the reacting particles are spherical in shape. However, the generated Zn nanocrystals were perfect hexagonal prism based on the TEM analysis. Thus, the spherical assumption would cause errors in extracting the kinetics parameters. Future models development for processing the oxidation kinetics data could consider the nanocrystal shape factor. Even better, taking into account of the fact that oxide shell preferentially formed on the higher energy surfaces (Zn $\{1\bar{1}00\}$ planes).

2. Conducting computer simulation to explore the mechanism of Zn nanocrystal evaporation anisotropy

In Chapter 3, the Zn NC evaporation work is presented. In the study, the size-dependent evaporation of free Zn NCs was studied by the in-flight tandem method. The variation of the onset temperature of evaporation with the size of Zn NCs is found to be similar to the melting temperature depression of small nanoparticles. We observed the evaporation anisotropy effect during the evaporation process of NCs using electron microscopy. A phenomenological model based on crystal-face dependent surface melting was developed to explain the evaporation anisotropy. Surface energy is believed to play the key role in determining the particle

morphology. However, this model failed to predict the observed convex curvature of the evaporated surfaces. A more sophisticated model with radial surface energy distribution could be used to predict both the order and the curvature of the evaporated planes. One route for this model development would be to conduct a computer simulation. We could monitor the particle shape evolution by varying the radial surface energy distribution of the evaporated surfaces until we find the shape observed in experiment.

3. Conducting hydrolysis experiment on Zn materials generated from solar ZnO dissociation

In Chapter 4, the Zn NC hydrolysis work is presented. In the study, the hydrolysis kinetics of free Zn NCs was studied by in-flight tandem ion-mobility method. The Zn NCs were generated in-situ by condensation/evaporation method. Based on the mass change of Zn NCs, a low temperature reaction mechanism for Zn NC hydrolysis was proposed. Since the Zn NC hydrolysis reaction is investigated as the second step of a Zn/ZnO solar thermochemical water splitting cycle, the ideal reactant Zn materials would be the Zn powder produced directly from solar ZnO dissociation. One would imagine at least the morphology of the solar Zn will be different from the in-situ generated Zn NCs. Steinfeld and his colleagues conducted a series experiments [44, 46, 136, 139, 155, 156, 188, 189] to investigate the dissociation of ZnO in a solar furnace and studied the zinc vapor condensation process in the presence of oxygen under different conditions. The following electron microscopic images show the products from solar

ZnO dissociation. As we can see from the images, depending on the reactor designs and operation conditions the dissociation products can vary widely in morphology.

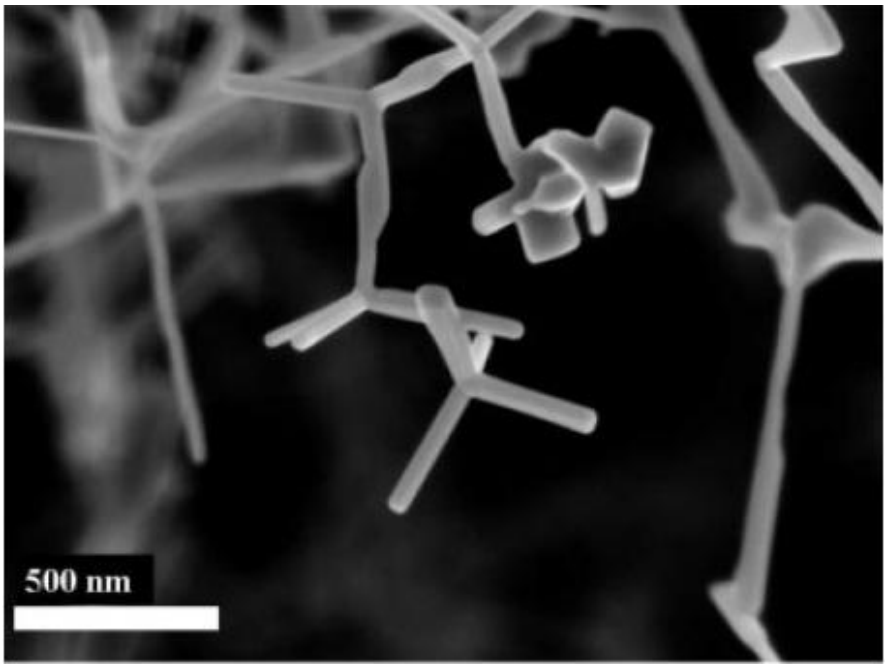

(a)

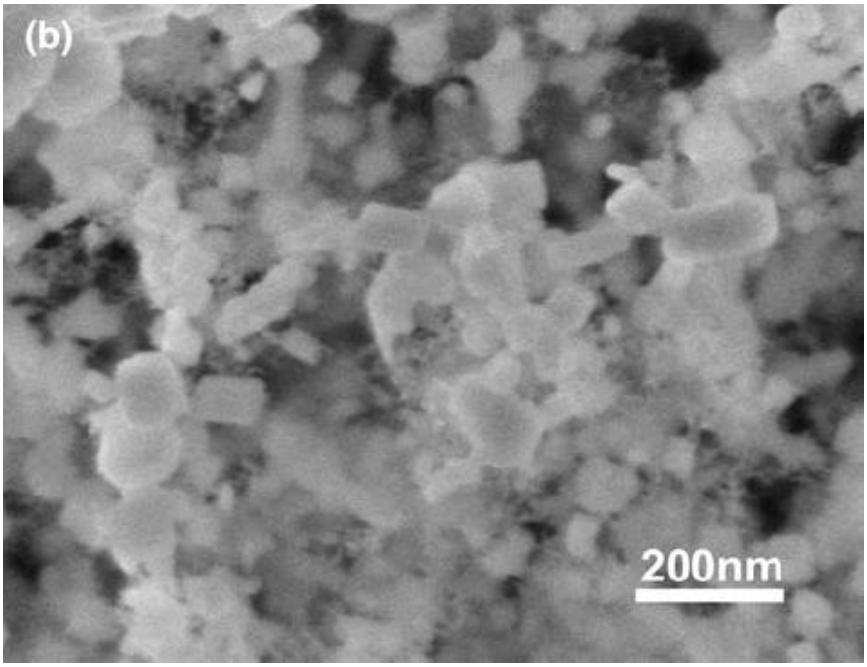

(b)

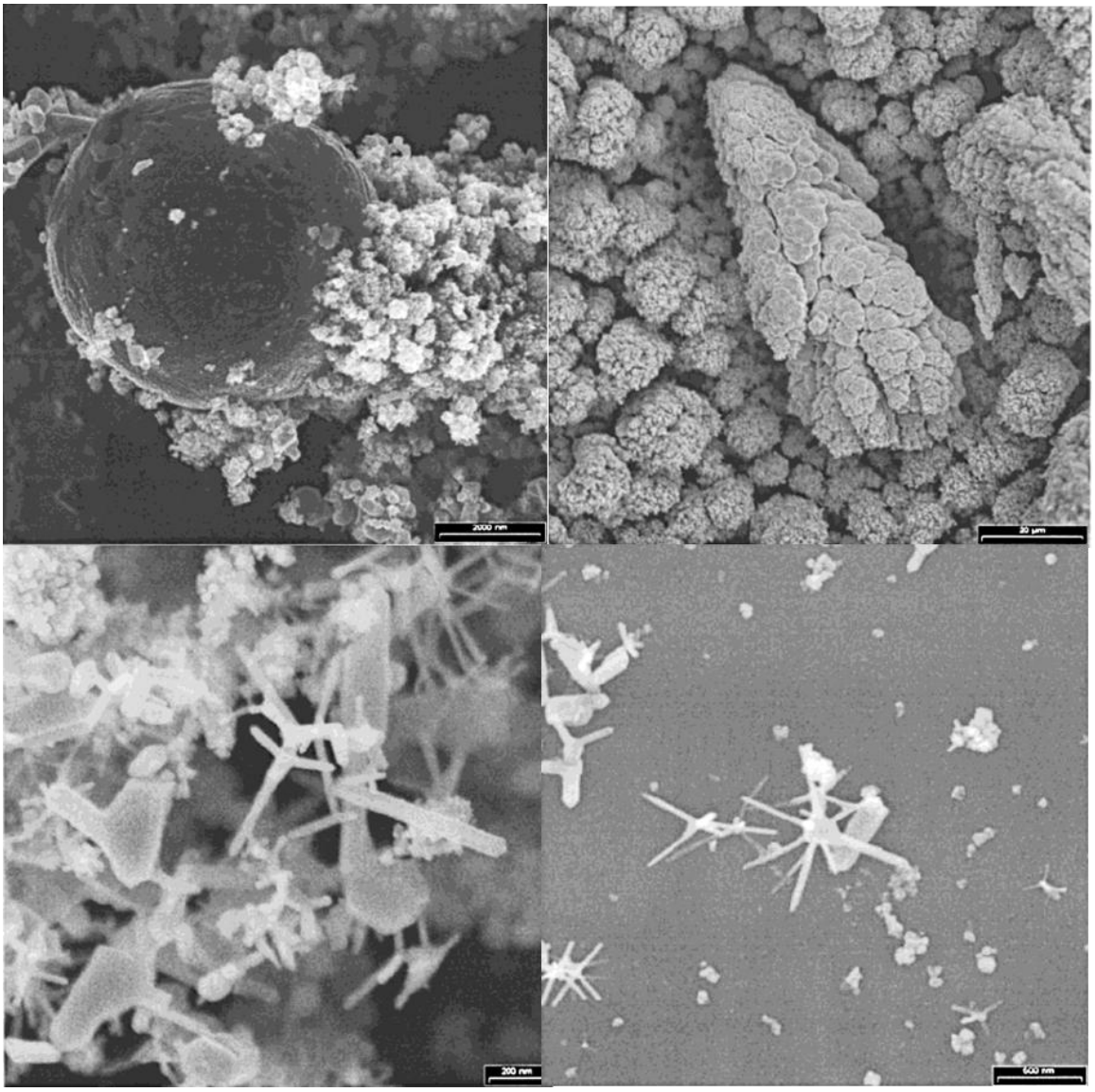

(c)

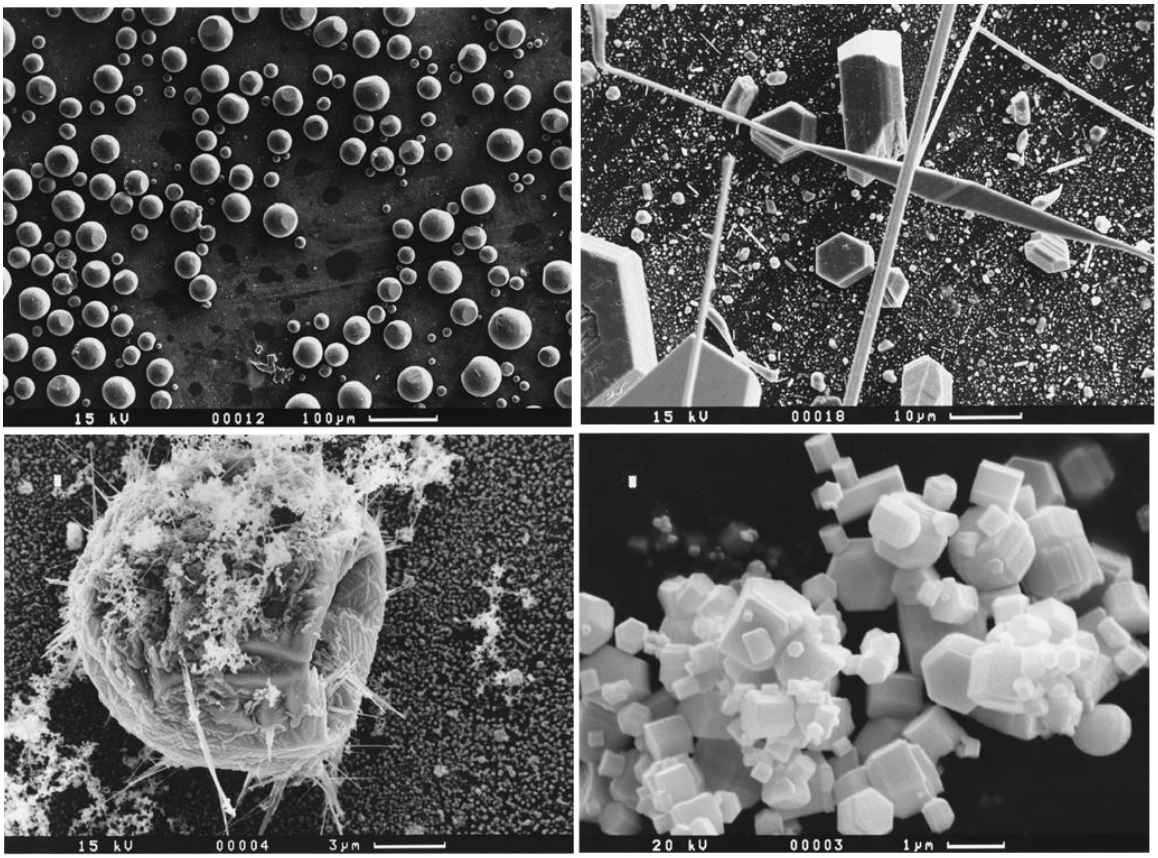

(d)

Figure 8.1 Solid products from solar ZnO dissociation (a) SEM image of recombined gaseous product from ZnO dissociation, from reference [188] (b) SEM image of solid product from ZnO dissociation, from reference [189] (c) SEM images of condensed products from the water-cooled target surface in ZnO dissociation, from reference [155] (d) SEM images of ZnO dissociation product from reference [44], upper left: the deposit structures of droplet at T>693K; upper right: the deposit structures of droplet at T<693K; lower left: the surface of a partially oxidized Zn droplet; lower right: Zn obtained from solar thermal dissociation

Due to the reverse reaction (re-oxidation of zinc), the influence of the zinc vapor and oxygen dilution in inert gas during the ZnO dissociation experiment was found to be very complex. This is to say, in addition to the morphology difference, the composition of the ZnO dissociation product is expected to be deviated from pure Zn due to the existence of un-dissociated ZnO and re-oxidation of Zn vapor. Thus, the challenges in studying the hydrolysis kinetics using solar ZnO dissociation products are how to deals with the different shaped Zn particles and how to eliminate the influence of ZnO.

4. Improving the catalytic fuel decomposition process by co-production of high-value carbon nanostructure

In Chapter 5, the catalytic fuel decomposition work is presented. In the study, the thermal and catalytic decomposition of liquid fuels were investigated in an aerosol reactor configuration to produce hydrogen and an easily separable solid carbonaceous aerosol product. Iron aerosol particles were used as the catalytic materials. The carbon black particles and graphite films were co-produced from the decomposition process. The process has the advantages of producing no carbon oxides and easily separable solid carbon and gaseous hydrogen products. Based on the economic analysis [47, 49], the sale price of solid carbon is the key factor which determines the economic feasibility of the fuel decomposition technology. Therefore, future work on fuel decomposition should focus on improving the current method to produce high-value carbon products such as carbon nanotubes, carbon nanofibers. Two criterions

can be summarized for carbon nanotube formation based on the previous work in our group [190]: the addition of relatively large amount of hydrogen as the cleaning agent for catalyst metal particles and relatively low temperatures. For the liquid fuel decomposition process, lower temperature means sacrifice of hydrogen yield. Therefore, the challenge would be how to produce carbon nanotubes without significant reduction in hydrogen yield.

5. Extending the catalytic ignition study to real jet fuels

In Chapter 6, the work of catalytic ignition of liquid fuels is presented. In the study, the ignition of toluene and octane over the surfaces of in situ generated free metal (Fe, Ni) nanoparticles was performed experimentally in an aerosol reactor. The Fe and Ni nanoparticles were generated in-situ and used as the catalysts for fuel ignition. Future work on this topic would involve extending the current study to a real jet fuel. A real jet fuel is a mixture of different hydrocarbons. The combined effect of different components on real fuel ignition properties is hard to predict from information of individual hydrocarbon component. Thus, the best way is study the ignition of a real fuel catalyzed by metal nanoparticles.

6. Improving the synthesis method to control the size and wall thickness of hollow black carbon nanoparticle

In Chapter 7, the work on hollow black carbon particle synthesis is presented. In the study, the synthesis of hollow black carbon nanoparticles in gas phase by controlled oxidation method was investigated. We concluded that the formation of the hollow black carbon nanostructure is determined by the elemental carbon to organic carbon (EC/OC) ratio in the original particles and the oxidation conditions that the particles underwent. The effect of the oxidation conditions on the black carbon nanostructure was also examined. Hollow particles have potential applications in drug delivery, cell and enzyme transplantation, contaminated waste removal, gene therapy, and heterogeneous catalysis. All those applications need well-defined hollow nanostructures. Thus, future work on this topic could involve improvement of the current synthesis method to produce hollow carbon nanoparticles with designed size and wall thickness. One approach could be on-line particle size or mass selection followed by controlled oxidation reaction.

Bibliography

1. The History of Hydrogen by the National Hydrogen Association.

2. Bockris, J. O. M., The origin of ideas on a Hydrogen Economy and its solution to the decay of the environment. *International Journal of Hydrogen Energy* **2002,** 27, (7-8), 731-740.

3. Keeling, C. D., The Concentration and Isotopic Abundances of Carbon Dioxide in the Atmosphere. *Tellus* **1960,** 12, 200-203.

4. Keeling, C. D., Rewards and Penalties of Monitoring the Earth. *Annual Review of Energy and the Environment* **1998,** 23, 25-82.

5. Navarro, R. M.; Pena, M. A.; Fierro, J. L. G., Hydrogen production reactions from carbon feedstocks: Fossils fuels and biomass. *Chemical Reviews* **2007,** 107, (10), 3952-3991.

6. Gupta, R. B., *Hydrogen Fuel: Production, Transport, and Storage*. CRC Press: 2009.

7. Rajeshwar, K.; McConnell, R.; Licht, S., *Solar Hydrogen Generation*. Springer: 2008.

8. Halmann, M.; Steinfeld, A., Fuel saving, carbon dioxide emission avoidance, and syngas production by tri-reforming of flue gases from coal- and gas-fired power stations, and by the carbothermic reduction of iron oxide. *Energy* **2006,** 31, (15), 3171-3185.

9. Baron, P. A.; Willeke, K., *Aerosol Measurement*. John Wiley and Sons, Inc.: 2001.

10. Colbeck, I., *Physics And Chemical Properties of Aerosols*. Blackie Academic & Professional: 1998.

11. Pui, D. Y. H., Direct-reading instrumentation for workplace aerosol measurements. *Analyst* **1996,** 121, (9), 1215-1224.

12. Wang, Z. L., *Characterization of Nanophase Materials*. WILEY-VCH: 2000.

13. Goldstein, A. N.; Echer, C. M.; Alivisatos, A. P., Melting in Semiconductor Nanocrystals. *Science* **1992,** 256, (5062), 1425-1427.

14. Lai, S. L.; Guo, J. Y.; Petrova, V.; Ramanath, G.; Allen, L. H., Size-dependent melting properties of small tin particles: Nanocalorimetric measurements. *Physical Review Letters* **1996,** 77, (1), 99-102.

15. Schmidt, M.; Kusche, R.; von Issendorff, B.; Haberland, H., Irregular variations in the melting point of size-selected atomic clusters. *Nature* **1998,** 393, (6682), 238-240.

16. Ajayan, P. M.; Marks, L. D., Experimental-Evidence for Quasimelting in Small Particles. *Physical Review Letters* **1989,** 63, (3), 279-282.

17. Pluis, B.; Vandergon, A. W. D.; Frenken, J. W. M.; Vanderveen, J. F., Crystal-Face Dependence of Surface Melting. *Physical Review Letters* **1987,** 59, (23), 2678-2681.

18. Wang, Z. L.; Petroski, J. M.; Green, T. C.; El-Sayed, M. A., Shape transformation and surface melting of cubic and tetrahedral platinum nanocrystals. *Journal of Physical Chemistry B* **1998,** 102, (32), 6145-6151.

19. Nanda, K. K.; Kruis, F. E.; Fissan, H., Evaporation of free PbS nanoparticles: Evidence of the Kelvin effect. *Physical Review Letters* **2002,** 89, (25).

20. Wiechowski, A.; Savinova, E.; Vayenas, C., *Catalysis and Electrocatalysis at Nanoparticle Surfaces*. Marcel Dekker, Inc.: New York
Basel, 2003.

21. Burda, C.; Chen, X. B.; Narayanan, R.; El-Sayed, M. A., Chemistry and properties of nanocrystals of different shapes. *Chemical Reviews* **2005,** 105, (4), 1025-1102.

22. Narayanan, R.; El-Sayed, M. A., Catalysis with transition metal nanoparticles in colloidal solution: Nanoparticle shape dependence and stability. *Journal of Physical Chemistry B* **2005,** 109, (26), 12663-12676.

23. El-Sayed, M. A., Some interesting properties of metals confined in time and nanometer space of different shapes. *Accounts of Chemical Research* **2001,** 34, (4), 257-264.

24. Knutson, E. O.; Whitby, K. T., Aerosol Classification by Electric Mobility: Apparatus, Theory, and Applications. *Journal of Aerosol Science* **1975**, (8), 443-451.

25. Song, D. K.; Lee, H. M.; Chang, H.; Kim, S. S.; Shimada, M.; Okuyama, K., Performance evaluation of long differential mobility analyzer (LDMA) in measurements of nanoparticles. *Journal of Aerosol Science* **2006,** 37, (5), 598-615.

26. Ehara, K.; Hagwood, C.; Coakley, K. J., Novel method to classify aerosol particles according to their mass-to-charge ratio - Aerosol particle mass analyser. *Journal of Aerosol Science* **1996,** 27, (2), 217-234.

27. McMurry, P. H.; Wang, X.; Park, K.; Ehara, K., The relationship between mass and mobility for atmospheric particles: A new technique for measuring particle density. *Aerosol Science and Technology* **2002,** 36, (2), 227-238.

28. Agarwal, J. K.; Sem, G. J., CONTINUOUS-FLOW, SINGLE-PARTICLE-COUNTING CONDENSATION NUCLEUS COUNTER. *Journal of Aerosol Science* **1980,** 11, (4), 343-&.

29. Stolzenburg, M. R.; McMurry, P. H., AN ULTRAFINE AEROSOL CONDENSATION NUCLEUS COUNTER. *Aerosol Science and Technology* **1991,** 14, (1), 48-65.

30. Sinclair, D.; Yue, P. C., THE CONTINUOUS-FLOW CONDENSATION NUCLEUS COUNTER .2. *Aerosol Science and Technology* **1982,** 1, (2), 217-223.

31. Nowotny, J.; Sorrell, C. C.; Sheppard, L. R.; Bak, T., Solar-hydrogen: Environmentally safe fuel for the future. *International Journal of Hydrogen Energy* **2005,** 30, (5), 521-544.

32. Myers, D. R., The Solar Resource. In *Solar Hydrogen Generation*, Rajeshwar, K.; McConnell, R.; Licht, S., Eds. Springer: New York, 2008.

33. Steinfeld, A., Solar thermochemical production of hydrogen - a review. *Solar Energy* **2005,** 78, (5), 603-615.

34. Kodama, T.; Gokon, N., Thermochernical cycles for high-temperature solar hydrogen production. *Chemical Reviews* **2007,** 107, 4048-4077.

35. Fujishima, A.; Honda, K., Electrochemical Photolysis of Water at a Semiconductor Electrode. *Nature* **1972,** 238, (5358), 37-+.

36. Nakamura, T., Hydrogen Production from Water Utilizing Solar Heat at High-Temperatures. *Solar Energy* **1977,** 19, (5), 467-475.

37. Lundberg, M., Model-Calculations on Some Feasible 2-Step Water Splitting Processes. *International Journal of Hydrogen Energy* **1993,** 18, (5), 369-376.

38. Bilgen, E.; Ducarroir, M.; Foex, M.; Sibieude, F.; Trombe, F., Use of Solar-Energy for Direct and 2-Step Water Decomposition Cycles. *International Journal of Hydrogen Energy* **1977,** 2, (3), 251-257.

39. Abanades, S.; Charvin, P.; Flamant, G.; Neveu, P., Screening of water-splitting thermochemical cycles potentially attractive for hydrogen production by concentrated solar energy. *Energy* **2006,** 31, (14), 2805-2822.

40. Sibieude, F.; Ducarroir, M.; Tofighi, A.; Ambriz, J., High-Temperature Experiments with a Solar Furnace - the Decomposition of Fe3o4, Mn3o4, Cdo. *International Journal of Hydrogen Energy* **1982,** 7, (1), 79-88.

41. Steinfeld, A.; Kuhn, P.; Reller, A.; Palumbo, R.; Murray, J.; Tamaura, Y., Solar-processed metals as clean energy carriers and water-splitters. *International Journal of Hydrogen Energy* **1998,** 23, (9), 767-774.

42. Steinfeld, A., Solar hydrogen production via a two-step water-splitting thermochemical cycle based on Zn/ZnO redox reactions. *International Journal of Hydrogen Energy* **2002,** 27, (6), 611-619.

43. Wegner, K.; Ly, H. C.; Weiss, R. J.; Pratsinis, S. E.; Steinfeld, A., In situ formation and hydrolysis of Zn nanoparticles for H-2 production by the 2-step ZnO/Zn water-splitting thermochemical cycle. *International Journal of Hydrogen Energy* **2006,** 31, (1), 55-61.

44. Weidenkaff, A.; Steinfeld, A.; Wokaun, A.; Auer, P. O.; Eichler, B.; Reller, A., Direct solar thermal dissociation of zinc oxide: Condensation and crystallisation of zinc in the presence of oxygen. *Solar Energy* **1999,** 65, (1), 59-69.

45. Muller, R.; Steinfeld, A., H2O-splitting thermochemical cycle based on ZnO/Zn-redox: Quenching the effluents from the ZnO dissociation. *Chemical Engineering Science* **2008,** 63, (1), 217-227.

46. Muller, R.; Lipinski, W.; Steinfeld, A., Transient heat transfer in a directly-irradiated solar chemical reactor for the thermal dissociation of ZnO. *Applied Thermal Engineering* **2008,** 28, (5-6), 524-531.

47. Muradov, N., Hydrogen via methane decomposition: an application for decarbonization of fossil fuels. *International Journal of Hydrogen Energy* **2001,** 26, (11), 1165-1175.

48. Muradov, N. Z., Thermocatalytic production of hydrogen via pyrolysis of hydrocarbon fuels: From methane to residual oil. *Abstracts of Papers of the American Chemical Society* **2001,** 221, U494-U494.

49. Muradov, N. Z.; Veziroglu, T. N., From hydrocarbon to hydrogen-carbon to hydrogen economy. *International Journal of Hydrogen Energy* **2005,** 30, (3), 225-237.

50. Rostrup-Nielsen, J., Catalytic steam reforming. In *Catalysis: Science and Technology*, Anderson, J.; Boudart, M., Eds. Springer: Berlin, 1984.

51. Xu, J. G.; Froment, G. F., METHANE STEAM REFORMING, METHANATION AND WATER-GAS SHIFT .1. INTRINSIC KINETICS. *Aiche Journal* **1989,** 35, (1), 88-96.

52. Xu, J. G.; Froment, G. F., METHANE STEAM REFORMING .2. DIFFUSIONAL LIMITATIONS AND REACTOR SIMULATION. *Aiche Journal* **1989,** 35, (1), 97-103.

53. Rostrupnielsen, J. R.; Hansen, J. H. B., CO2-REFORMING OF METHANE OVER TRANSITION-METALS. *Journal of Catalysis* **1993,** 144, (1), 38-49.

54. Armor, J. N., The multiple roles for catalysis in the production of H-2. *Applied Catalysis a-General* **1999,** 176, (2), 159-176.

55. Muradov, N., Production of Hydrogen from Hydrocarbons. In *Hydrogen Fuel: Production, Transport, and Storage*, Gupta, R., Ed. CRC Press: 2009.

56. Ashcroft, A. T.; Cheetham, A. K.; Green, M. L. H.; Vernon, P. D. F., PARTIAL OXIDATION OF METHANE TO SYNTHESIS GAS-USING CARBON-DIOXIDE. *Nature* **1991,** 352, (6332), 225-226.

57. Hu, Y. H.; Ruckenstein, E., Catalytic conversion of methane to synthesis gas by partial oxidation and CO2 reforming. *Advances in Catalysis, Vol 48* **2004,** 48, 297-345.

58. Bradford, M. C. J.; Vannice, M. A., CO2 reforming of CH4. *Catalysis Reviews-Science and Engineering* **1999,** 41, (1), 1-42.

59. Bradford, M. C. J.; Vannice, M. A., CO2 reforming of CH4 over supported Ru catalysts. *Journal of Catalysis* **1999,** 183, (1), 69-75.

60. Sigl, M.; Bradford, M. C. J.; Knozinger, H.; Vannice, M. A., CO2 reforming of methane over vanadia-promoted Rh/SiO2 catalysts. *Topics in Catalysis* **1999,** 8, (3-4), 211-222.

61. Haussinger, P.; Lohmuller, R.; Watson, A., *Ullmann's Encyclopedia of Industrial Chemistry*. Wiley-VCH Verlag GmbH & Co.,: Weinheim, 2002.

62. Dissanayake, D.; Rosynek, M. P.; Kharas, K. C. C.; Lunsford, J. H., PARTIAL OXIDATION OF METHANE TO CARBON-MONOXIDE AND

HYDROGEN OVER A NI/AL2O3 CATALYST. *Journal of Catalysis* **1991,** 132, (1), 117-127.

63. Hickman, D. A.; Schmidt, L. D., PRODUCTION OF SYNGAS BY DIRECT CATALYTIC-OXIDATION OF METHANE. *Science* **1993,** 259, (5093), 343-346.

64. Aasberg-Petersen, K., Synthesis gas production for FT synthesis. In *Fischer-Tropsch Technology*, Steynbery, A.; Dry, M., Eds. Elsevier: Amsterdam, 2004.

65. Muradov, N. Z., CO2-free production of hydrogen by catalytic pyrolysis of hydrocarbon fuel. *Energy & Fuels* **1998,** 12, (1), 41-48.

66. *Kirk-Othmer Encyclopedia of Chemical Technology*. Wiley: New York, 1992.

67. Dean, A. M., DETAILED KINETIC MODELING OF AUTOCATALYSIS IN METHANE PYROLYSIS. *Journal of Physical Chemistry* **1990,** 94, (4), 1432-1439.

68. Holmen, A.; Olsvik, O.; Rokstad, O. A., PYROLYSIS OF NATURAL-GAS - CHEMISTRY AND PROCESS CONCEPTS. *Fuel Processing Technology* **1995,** 42, (2-3), 249-267.

69. Muradov, N.; Smith, F.; T-Raissi, A., Catalytic activity of carbons for methane decomposition reaction. *Catalysis Today* **2005,** 102, 225-233.

70. Matsukata, M.; Matsushita, T.; Ueyama, K., A CIRCULATING FLUIDIZED-BED CH4 REFORMER - PERFORMANCE OF SUPPORTED NI CATALYSTS. *Energy & Fuels* **1995,** 9, (5), 822-828.

71. Liao, M. S.; Au, C. T.; Ng, C. F., Methane dissociation on Ni, Pd, Pt and Cu metal(111) surfaces - A theoretical comparative study. *Chemical Physics Letters* **1997,** 272, (5-6), 445-452.

72. Au, C. T.; Liao, M. S.; Ng, C. F., A theoretical investigation of methane dissociation on Rh(111). *Chemical Physics Letters* **1997,** 267, (1-2), 44-50.

73. Koerts, T.; Deelen, M.; Vansanten, R. A., HYDROCARBON FORMATION FROM METHANE BY A LOW-TEMPERATURE 2-STEP REACTION SEQUENCE. *Journal of Catalysis* **1992,** 138, (1), 101-114.

74. Snoeck, J. W.; Froment, G. F.; Fowles, M., Kinetic study of the carbon filament formation by methane cracking on a nickel catalyst. *Journal of Catalysis* **1997,** 169, (1), 250-262.

75. Snoeck, J. W.; Froment, G. F.; Fowles, M., Filamentous carbon formation and gasification: Thermodynamics, driving force, nucleation, and steady-state growth. *Journal of Catalysis* **1997,** 169, (1), 240-249.

76. Ahmed, S.; Aitani, A.; Rahman, F.; Al-Dawood, A.; Al-Muhaish, F., Decomposition of hydrocarbons to hydrogen and carbon. *Applied Catalysis a-General* **2009,** 359, (1-2), 1-24.

77. Kariya, N.; Fukuoka, A.; Utagawa, T.; Sakuramoto, M.; Goto, Y.; Ichikawa, M., Efficient hydrogen production using cyclohexane and decalin by pulse-spray mode reactor with Pt catalysts. *Applied Catalysis a-General* **2003,** 247, (2), 247-259.

78. Takenaka, S.; Kawashima, K.; Matsune, H.; Kishida, M., Production of CO-free hydrogen through the decomposition of LPG and kerosene over Ni-based catalysts. *Applied Catalysis a-General* **2007,** 321, (2), 165-174.

79. Xing, Y.; Fang, W. J.; Xie, W. J.; Guo, Y. S.; Lin, R. S., Thermal Cracking of JP-10 under Pressure. *Industrial & Engineering Chemistry Research* **2008,** 47, (24), 10034-10040.

80. Takenaka, S.; Kobayashi, Y.; Otsuka, K., Formation of hydrogen through the decomposition of kerosene over nickel-based catalysts. *Energy & Fuels* **2004,** 18, (6), 1775-1783.

81. Hirsch, D.; Steinfeld, A., Solar hydrogen production by thermal decomposition of natural gas using a vortex-flow reactor. *International Journal of Hydrogen Energy* **2004,** 29, (1), 47-55.

82. Dahl, J. K.; Buechler, K. J.; Weimer, A. W.; Lewandowski, A.; Bingham, C., Solar-thermal dissociation of methane in a fluid-wall aerosol flow reactor. *International Journal of Hydrogen Energy* **2004,** 29, (7), 725-736.

83. Kogan, M.; Kogan, A., Production of hydrogen and carbon by solar thermal methane splitting. I. The unseeded reactor. *International Journal of Hydrogen Energy* **2003,** 28, (11), 1187-1198.

84. Kogan, A.; Kogan, M.; Barak, S., Production of hydrogen and carbon by solar thermal methane splitting. II. Room temperature simulation tests of seeded solar reactor. *International Journal of Hydrogen Energy* **2004,** 29, (12), 1227-1236.

85. Sutton, G. P., *Rocket Propulsion Elements*. 7th ed.; Wiley-Interscience: 2000.

86. Laboratory, L. L. N., *Science and Technology Review* **1995**.

87. Abu Hamed, T.; Davidson, J. H.; Stolzenburg, M., Hydrolysis of evaporated Zn in a hot wall flow reactor. *Journal of Solar Energy Engineering-Transactions of the Asme* **2008,** 130, (4).

88. Ernst, F. O.; Tricoli, A.; Pratsinis, S. E.; Steinfeld, A., Co-synthesis of H-2 and ZnO by in-situ Zn alerosol formation and hydrolysis. *Aiche Journal* **2006,** 52, (9), 3297-3303.

89. Wong, E. M.; Searson, P. C., ZnO quantum particle thin films fabricated by electrophoretic deposition. *Applied Physics Letters* **1999,** 74, (20), 2939-2941.

90. Tang, Z. K.; Wong, G. K. L.; Yu, P.; Kawasaki, M.; Ohtomo, A.; Koinuma, H.; Segawa, Y., Room-temperature ultraviolet laser emission from self-assembled ZnO microcrystallite thin films. *Applied Physics Letters* **1998,** 72, (25), 3270-3272.

91. Pan, Z. W.; Dai, Z. R.; Wang, Z. L., Nanobelts of semiconducting oxides. *Science* **2001,** 291, (5510), 1947-1949.

92. Wang, Z.; Harris, R., Morphology of Zinc Deposited from Mixed Gas Streams at Reduced Pressures. *Materials Characterization* **1993,** 30, (3), 155-173.

93. Kim, S.; Jeong, M. C.; Oh, B. Y.; Lee, W.; Myoung, J. M., Fabrication of Zn/ZnO nanocables through thermal oxidation of Zn nanowires grown by RF magnetron sputtering. *Journal of Crystal Growth* **2006,** 290, (2), 485-489.

94. Wang, Y. G.; Lau, S. P.; Lee, H. W.; Yu, S. F.; Tay, B. K.; Zhang, X. H.; Hng, H. H., Photoluminescence study of ZnO films prepared by thermal oxidation of Zn metallic films in air. *Journal of Applied Physics* **2003,** 94, (1), 354-358.

95. Lu, H. B.; Li, H.; Liao, L.; Tian, Y.; Shuai, M.; Li, J. C.; Fhu, M.; Fu, Q.; Zhu, B. P., Low-temperature synthesis and photocatalytic properties of ZnO nanotubes by thermal oxidation of Zn nanowires. *Nanotechnology* **2008,** 19, (4).

96. Nakamura, R.; Lee, J. G.; Tokozakura, D.; Mori, H.; Nakajima, H., Formation of hollow ZnO through low-temperature oxidation of Zn nanoparticles. *Materials Letters* **2007,** 61, (4-5), 1060-1063.

97. Wagner, C. Z., *Phys. Chem. Abt. B* **1933,** 21.

98. Atkinson, A., Transport Processes During the Growth of Oxide-Films at Elevated-Temperature. *Reviews of Modern Physics* **1985,** 57, (2), 437-470.

99. A. T. Fromhold, J., *Theory of Metal Oxidation*. North-Holland Publishing Company: 1976; Vol. 1.

100. A. T. Fromhold, J., *Theory of Metal Oxidation*. North-Holland Publishing Company: 1980; Vol. 2.

101. Cabrera, N.; Mott, N. F., Theory of the Oxidation of Metals. *Reports on Progress in Physics* **1948,** 12, 163-184.

102. Liu, H. T.; Armitage, A. F.; Woodruff, D. P., Anisotropy of Initial Oxidation-Kinetics of Nickel Single-Crystal Surfaces. *Surface Science* **1982,** 114, (2-3), 431-444.

103. Munoz-Marquez, M. A.; Tanner, R. E.; Woodruff, D. P., Surface and subsurface oxide formation on Ni(100) and Ni(111). *Surface Science* **2004,** 565, (1), 1-13.

104. Zhou, L.; Rai, A.; Piekiel, N.; Ma, X. F.; Zachariah, M. R., Ion-Mobility Spectrometry of Nickel Nanoparticle Oxidation Kinetics: Application to Energetic Materials. *Journal of Physical Chemistry C* **2008,** 112, (42), 16209-16218.

105. Liu, B. Y. H.; Pui, D. Y. H., Equilibrium Bipolar Charge-Distribution of Aerosols. *Journal of Colloid and Interface Science* **1974,** 49, (2), 305-312.

106. Liu, B. Y. H. P., D. Y. H., *J. Colloid Interface Sci.* **1974,** 47, 155-171.

107. Knutson, E. O.; Whitby, K. T., Anomalous Unipolar Diffusion Charging of Polystyrene Latex Aerosols. *Journal of Colloid and Interface Science* **1975,** 53, (3), 493-495.

108. Kim, S. H.; Woo, K. S.; Liu, B. Y. H.; Zachariah, M. R., Method of measuring charge distribution of nanosized aerosols. *Journal of Colloid and Interface Science* **2005,** 282, (1), 46-57.

109. Jung, H. J.; Kittelson, D. B.; Zachariah, M. R., Kinetics and visualization of soot oxidation using transmission electron microscopy. *Combustion and Flame* **2004,** 136, (4), 445-456.

110. Rai, A.; Park, K.; Zhou, L.; Zachariah, M. R., Understanding the mechanism of aluminium nanoparticle oxidation. *Combustion Theory and Modelling* **2006,** 10, (5), 843-859.

111. Lall, A. A.; Ma, X. F.; Guha, S.; Mulholland, G. W.; Zachariah, M. R., Online Nanoparticle Mass Measurement by Combined Aerosol Particle Mass Analyzer and Differential Mobility Analyzer: Comparison of Theory and Measurements. *Aerosol Science and Technology* **2009,** 42, (11), 1075-1083.

112. Levenspiel, O., *Chemical Reaction Engineering*. 3rd ed. ed.; John Wiley & Sons: 1999.

113. Carter, R. E., Kinetic Model for Solid-State Reactions. *Journal of Chemical Physics* **1961,** 34, (6), 2010-&.

114. Park, K.; Lee, D.; Rai, A.; Mukherjee, D.; Zachariah, M. R., Size-resolved kinetic measurements of aluminum nanoparticle oxidation with single particle mass spectrometry. *Journal of Physical Chemistry B* **2005,** 109, (15), 7290-7299.

115. Mahadevan, R.; Lee, D.; Sakurai, H.; Zachariah, M. R., Measurement of condensed-phase reaction kinetics in the aerosol phase using single particle mass spectrometry. *Journal of Physical Chemistry A* **2002,** 106, (46), 11083-11092.

116. Campbell, T.; Kalia, R. K.; Nakano, A.; Vashishta, P.; Ogata, S.; Rodgers, S., Dynamics of oxidation of aluminum nanoclusters using variable charge molecular-dynamics simulations on parallel computers. *Physical Review Letters* **1999,** 82, (24), 4866-4869.

117. Law, J. B. K.; Boothroyd, C. B.; Thong, J. T. L., Site-specific growth of ZnO nanowires from patterned Zn via compatible semiconductor processing. *Journal of Crystal Growth* **2008,** 310, (10), 2485-2492.

118. Gao, P. X.; Wang, Z. L., Mesoporous polyhedral cages and shells formed by textured self-assembly of ZnO nanocrystals. *Journal of the American Chemical Society* **2003,** 125, (37), 11299-11305.

119. Nanda, K. K.; Maisels, A.; Kruis, F. E.; Fissan, H.; Stappert, S., Higher surface energy of free nanoparticles. *Physical Review Letters* **2003,** 91, (10).

120. Cleveland, C. L.; Luedtke, W. D.; Landman, U., Melting of gold clusters. *Physical Review B* **1999,** 60, (7), 5065-5077.

121. Ahmadi, T. S.; Wang, Z. L.; Green, T. C.; Henglein, A.; ElSayed, M. A., Shape-controlled synthesis of colloidal platinum nanoparticles. *Science* **1996,** 272, (5270), 1924-1926.

122. Ma, X. F.; Zachariah, M. R., Oxidation Anisotropy and Size-Dependent Reaction Kinetics of Zinc Nanocrystals. *Journal of Physical Chemistry C* **2009,** 113, (33), 14644-14650.

123. Lall, A. A.; Ma, X.; Guha, S.; Mulholland, G. W.; Zachariah, M. R., Online Nanoparticle Mass Measurement by Combined Aerosol Particle Mass Analyzer and

Differential Mobility Analyzer: Comparison of Theory and Measurements. *Aerosol Science and Technology* **2009,** 43, (11), 1075-1083.

124. Dash, J. G.; Rempel, A. W.; Wettlaufer, J. S., The physics of premelted ice and its geophysical consequences. *Reviews of Modern Physics* **2006,** 78, (3), 695-741.

125. J.F.van der Veen, B. P., A.W.Denier van der Gon, Surface Melting. In *Chemistry and Physics of Solid Surfaces*, R.Vanselow, R. H., Ed. Springer: 1988; Vol. VII, pp 455-490.

126. Sun, C. Q., Size dependence of nanostructures: Impact of bond order deficiency. *Progress in Solid State Chemistry* **2007,** 35, (1), 1-159.

127. Nanda, K. K., Bulk cohesive energy and surface tension from the size-dependent evaporation study of nanoparticles. *Applied Physics Letters* **2005,** 87, (2).

128. Wang, T. H.; Zhu, Y. F.; Jiang, Q., Size effect on evaporation temperature of nanocrystals. *Materials Chemistry and Physics* **2008,** 111, (2-3), 293-295.

129. *CRC Handook of Chemistry and Physics*. 89 ed.; CRC Press: 2008-2009.

130. Philipsen, P. H. T.; Baerends, E. J., Cohesive energy of 3d transition metals: Density functional theory atomic and bulk calculations. *Physical Review B* **1996,** 54, (8), 5326-5333.

131. Wedig, U.; Jansen, M.; Paulus, B.; Rosciszewski, K.; Sony, P., Structural and electronic properties of Mg, Zn, and Cd from Hartree-Fock and density functional calculations including hybrid functionals. *Physical Review B* **2007,** 75, (20).

132. Gaston, N.; Paulus, B., Ab initio correlation calculations for the ground-state properties of group-12 metals Zn and Cd. *Physical Review B* **2007,** 76, (21).

133. Gaston, N.; Paulus, B.; Wedig, U.; Jansen, M., Multiple minima on the energy landscape of elemental zinc: A wave function based ab initio study. *Physical Review Letters* **2008,** 100, (22).

134. Abraham, B. M.; Schreine.F, General Principles Underlying Chemical Cycles Which Thermally Decompose Water into Elements. *Industrial & Engineering Chemistry Fundamentals* **1974,** 13, (4), 305-310.

135. Weidenkaff, A.; Reller, A. W.; Wokaun, A.; Steinfeld, A., Thermogravimetric analysis of the ZnO/Zn water splitting cycle. *Thermochimica Acta* **2000,** 359, (1), 69-75.

136. Palumbo, R.; Lede, J.; Boutin, O.; Ricart, E. E.; Steinfeld, A.; Moller, S.; Weidenkaff, A.; Fletcher, E. A.; Bielicki, J., The production of Zn from ZnO in a high-temperature solar decomposition quench process - I. The scientific framework for the process. *Chemical Engineering Science* **1998,** 53, (14), 2503-2517.

137. Moller, S.; Palumbo, R., The development of a solar chemical reactor for the direct thermal dissociation of zinc oxide. *Journal of Solar Energy Engineering-Transactions of the Asme* **2001,** 123, (2), 83-90.

138. Moller, S.; Palumbo, R., Solar thermal decomposition kinetics of ZnO in the temperature range 1950-2400 K. *Chemical Engineering Science* **2001,** 56, (15), 4505-4515.

139. Schunk, L. O.; Haeberling, P.; Wepf, S.; Wuillemin, D.; Meier, A.; Steinfeld, A., A receiver-reactor for the solar thermal dissociation of zinc oxide. *Journal of Solar Energy Engineering-Transactions of the Asme* **2008,** 130, (2).

140. Bazan, J. C.; Gschaider, M. E.; Alimenti, G. A., Gravimetric study of interaction of water vapour with metallic zinc. *Journal of Thermal Analysis and Calorimetry* **1999,** 55, (2), 569-579.

141. Berman, A.; Epstein, M., The kinetics of hydrogen production in the oxidation of liquid zinc with water vapor. *International Journal of Hydrogen Energy* **2000,** 25, (10), 957-967.

142. Melchior, T.; Piatkowski, N.; Steinfeld, A., H-2 production by steam-quenching of Zn vapor in a hot-wall aerosol flow reactor. *Chemical Engineering Science* **2009,** 64, (5), 1095-1101.

143. Weiss, R. J.; Ly, H. C.; Wegner, K.; Pratsinis, S. E.; Steinfeld, A., H-2 production by Zn hydrolysis in a hot-wall aerosol reactor. *Aiche Journal* **2005,** 51, (7), 1966-1970.

144. Ernst, F. O.; Steinfeld, A.; Pratsinis, S. E., Hydrolysis rate of submicron Zn particles for solar H-2 synthesis. *International Journal of Hydrogen Energy* **2009,** 34, (3), 1166-1175.

145. Vishnevetsky, I.; Epstein, M., Production of hydrogen from solar zinc in steam atmosphere. *International Journal of Hydrogen Energy* **2007,** 32, 2791-2802.

146. Chambon, M.; Abanades, S.; Flamant, G., Kinetic investigation of hydrogen generation from hydrolysis of SnO and Zn solar nanopowders. *International Journal of Hydrogen Energy* **2009,** 34, (13), 5326-5336.

147. Funke, H. H.; Diaz, H.; Liang, X. H.; Carney, C. S.; Weimer, A. W.; Li, P., Hydrogen generation by hydrolysis of zinc powder aerosol. *International Journal of Hydrogen Energy* **2008,** 33, (4), 1127-1134.

148. Ortega, A., The kinetics of solid-state reactions toward consensus - Part I: Uncertainties, failures, and successes of conventional methods. *International Journal of Chemical Kinetics* **2001,** 33, (6), 343-353.

149. Anderson, H., On the Controversies in Ta Kinetics. *Thermochimica Acta* **1992,** 203, 515-518.

150. Alimenti, G. A.; Gschaider, M. E.; Bazan, J. C.; Ferreira, M. L., Theoretical and experimental study of the interaction of O-2 and H2O with metallic zinc - discussion of the initial step of oxide formation. *Journal of Colloid and Interface Science* **2004,** 276, (1), 24-38.

151. Graedel, T. E., Corrosion Mechanisms for Zinc Exposed to the Atmosphere. *Journal of the Electrochemical Society* **1989,** 136, (4), C193-C203.

152. Mattsson, E., Corrosion - an Electrochemical Problem. *Chemtech* **1985,** 15, (4), 234-243.

153. Smith, S. M.; Schlegel, H. B., Molecular orbital studies of zinc oxide chemical vapor deposition: Gas-phase hydrolysis of diethyl zinc, elimination reactions, and formation of dimers and tetramers. *Chemistry of Materials* **2003,** 15, (1), 162-166.

154. Ma, X.; Zachariah, M. R., Size-resolved kinetics of Zn nanocrystal hydrolysis for hydrogen generation. *International Journal of Hydrogen Energy* 35, (6), 2268-2277.

155. Weidenkaff, A.; Reller, A.; Sibieude, F.; Wokaun, A.; Steinfeld, A., Experimental investigations on the crystallization of zinc by direct irradiation of zinc oxide in a solar furnace. *Chemistry of Materials* **2000,** 12, (8), 2175-2181.

156. Haueter, P.; Moeller, S.; Palumbo, R.; Steinfeld, A., The production of zinc by thermal dissociation of zinc oxide - Solar chemical reactor design. *Solar Energy* **1999,** 67, (1-3), 161-167.

157. Meier, A.; Kirillov, V. A.; Kuvshinov, G. G.; Mogilnykh, Y. I.; Reller, A.; Steinfeld, A.; Weidenkaff, A., Solar thermal decomposition of hydrocarbons and carbon monoxide for the production of catalytic filamentous carbon. *Chemical Engineering Science* **1999,** 54, (15-16), 3341-3348.

158. Steinfeld, A.; Kirillov, V.; Kuvshinov, G.; Mogilnykh, Y.; Reller, A., Production of filamentous carbon and hydrogen by solarthermal catalytic cracking of methane. *Chemical Engineering Science* **1997,** 52, (20), 3599-3603.

159. Otsuka, K.; Shigeta, Y.; Takenaka, S., Production of hydrogen from gasoline range alkanes with reduced CO2 emission. *International Journal of Hydrogen Energy* **2002,** 27, (1), 11-18.

160. Biniwale, R. B.; Kariya, N.; Ichikawa, M., Dehydrogenation of cyclohexane over Ni based catalysts supported on activated carbon using spray-pulsed reactor and enhancement in activity by addition of a small amount of Pt. *Catalysis Letters* **2005,** 105, (1-2), 83-87.

161. Okada, Y.; Sasaki, E.; Watanabe, E.; Hyodo, S.; Nishijima, H., Development of dehydrogenation catalyst for hydrogen generation in organic chemical hydride method. *International Journal of Hydrogen Energy* **2006,** 31, (10), 1348-1356.

162. Wang, Y. G.; Shah, N.; Huffman, G. P., Pure hydrogen production by partial dehydrogenation of cyclohexane and methylcyclohexane over nanotube-supported Pt and Pd catalysts. *Energy & Fuels* **2004,** 18, (5), 1429-1433.

163. Wang, Y. G.; Shah, N.; Huffman, G. P., Simultaneous production of hydrogen and carbon nanostructures by decomposition of propane and cyclohexane over alumina supported binary catalysts. *Catalysis Today* **2005,** 99, (3-4), 359-364.

164. Karlsson, M. N. A.; Deppert, K.; Wacaser, B. A.; Karlsson, L. S.; Malm, J. O., Size-controlled nanoparticles by thermal cracking of iron pentacarbonyl. *Applied Physics a-Materials Science & Processing* **2005,** 80, (7), 1579-1583.

165. Kissin, Y. V., Chemical mechanisms of catalytic cracking over solid acidic catalysts: Alkanes and alkenes. *Catalysis Reviews-Science and Engineering* **2001,** 43, (1-2), 85-146.

166. Olah, G. A., *Hydrocarbon Chemistry*. second ed.; John Wiley & Sons, Inc.: 2003.

167. Wojciechowski, B. W., The reaction mechanism of catalytic cracking: Quantifying activity, selectivity, and catalyst decay. *Catalysis Reviews-Science and Engineering* **1998,** 40, (3), 209-328.

168. Turns, S. R., *An Introduction to Combustion*. McGraw Hill, Inc.: 2000.

169. Glikin, M.; Kutakova, D.; Prin, E., Unsteady processes and aerosol catalysis. *Chemical Engineering Science* **1999,** 54, (20), 4337-4342.

170. Glikin, M. A., Aerosol catalysis. *Theor. Found. Chem. Eng.* **1996,** 30, (4), 390-394.

171. Weber, A. P.; Seipenbusch, M.; Binnig, J.; Kasper, G., Influence of the particle morphology on the activity of nanometer platinum aerosol catalysts. *Particle & Particle Systems Characterization* **2002,** 19, (5), 300-305.

172. Weber, A. P.; Seipenbusch, M.; Kasper, G., Application of aerosol techniques to study the catalytic formation of methane on gasborne nickel nanoparticles. *Journal of Physical Chemistry A* **2001,** 105, (39), 8958-8963.

173. Shimizu, T.; Abid, A. D.; Poskrebyshev, G.; Wang, H.; Nabity, J.; Engel, J.; Yu, J.; Wickham, D.; Van Devener, B.; Anderson, S. L.; Williams, S., Methane ignition catalyzed by in situ generated palladium nanoparticles. *Combustion and Flame* 157, (3), 421-435.

174. Van Devener, B.; Anderson, S. L.; Shimizu, T.; Wang, H.; Nabity, J.; Engel, J.; Yu, J.; Wickham, D.; Williams, S., In Situ Generation of Pd/PdO Nanoparticle Methane Combustion Catalyst: Correlation of Particle Surface Chemistry with Ignition. *Journal of Physical Chemistry C* **2009,** 113, (48), 20632-20639.

175. Glassman, I.; Yetter, R. A., *Combustion*. Academic Press: 2008.

176. Shen, H. P. S.; Oehlschlaeger, M. A., The autoignition of C8H10 aromatics at moderate temperatures and elevated pressures. *Combustion and Flame* **2009,** 156, (5), 1053-1062.

177. Edwards, T.; Maurice, L. Q., Surrogate mixtures to represent complex aviation and rocket fuels. *Journal of Propulsion and Power* **2001,** 17, (2), 461-466.

178. Violi, A.; Yan, S.; Eddings, E. G.; Sarofim, F.; Granata, S.; Faravelli, T.; Ranzi, E., Experimental formulation and kinetic model for JP-8 surrogate mixtures. *Combustion Science and Technology* **2002,** 174, (11-2), 399-417.

179. Eddings, E. G.; Yan, S. H.; Ciro, W.; Sarofim, A. F., Formulation of a surrogate for the simulation of jet fuel pool fires. *Combustion Science and Technology* **2005,** 177, (4), 715-739.

180. Humer, S.; Frassoldati, A.; Granata, S.; Faravelli, T.; Ranzi, E.; Seiser, R.; Seshadri, K., Experimental and kinetic modeling study of combustion of JP-8, its surrogates and reference components in laminar nonpremixed flows. *Proceedings of the Combustion Institute* **2007,** 31, 393-400.

181. Ma, X. F.; Lall, A. A.; Aronhime, N.; Zachariah, M. R., Catalytic decomposition of liquid hydrocarbons in an aerosol reactor: A potential solar route to hydrogen production. *International Journal of Hydrogen Energy* **2010,** 35, (14), 7476-7484.

182. Ladd, W. A.; Ladd, M. W., *Rubber Chemistry and Technology* **1961,** 34, 697.

183. Heckman, F. A., *Rubber Chemistry and Technology* **1964,** 37, 1245.

184. Vander Wal, R. L.; Yezerets, A.; Currier, N. W.; Kim, D. H.; Wang, C. M., HRTEM Study of diesel soot collected from diesel particulate filters. *Carbon* **2007,** 45, (1), 70-77.

185. Donnet, J.-B.; Bansal, R. C.; Wang, M.-J., *Carbon Black Science and Technology*. MARCEL DEKKER, INC.: New York, 1993.

186. Conny, J. M.; Klinedinst, D. B.; Wight, S. A.; Paulsen, J. L., Optimizing thermal-optical methods for measuring atmospheric elemental (black) carbon: A response surface study. *Aerosol Science and Technology* **2003,** 37, (9), 703-723.

187. Conny, J. M.; Norris, G. A.; Gould, T. R., Factorial-based response-surface modeling with confidence intervals for optimizing thermal-optical transmission analysis of atmospheric black carbon. *Analytica Chimica Acta* **2009,** 635, (2), 144-156.

188. Schunk, L. O.; Steinfeld, A., Kinetics of the Thermal Dissociation of ZnO Exposed to Concentrated Solar Irradiation Using a Solar-Driven Thermogravimeter in the 1800-2100 K Range. *Aiche Journal* **2009,** 55, (6), 1497-1504.

189. Gstoehl, D.; Brambilla, A.; Schunk, L. O.; Steinfeld, A., A quenching apparatus for the gaseous products of the solar thermal dissociation of ZnO. *Journal of Materials Science* **2008,** 43, (14), 4729-4736.

190. Kim, S. H.; Zachariah, M. R., Gas-phase growth of diameter-controlled carbon nanotubes. *Materials Letters* **2007,** 61, (10), 2079-2083.